Computation of bubbly cavitating flow in shock wave lithotripsy

Thesis by

Michel Tanguay

In Partial Fulfillment of the Requirements

for the Degree of

Doctor of Philosophy

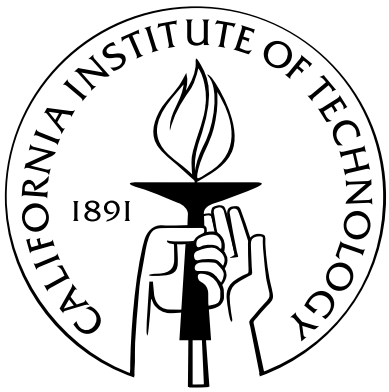

California Institute of Technology

Pasadena, California

2004

(Submitted May 25, 2004)

Acknowledgements

Above all, I would like to thank my advisor, Tim Colonius, for his advice and guidance. This work was conducted in the context of an NIH program project grant (PPG) under the leadership of Andy Evans. I would therefore like to thank all its participants for their comments and in particular, Larry Crum, Mike Bailey and Robin Cleveland for their invaluable contributions to this work.

On a more personal level, working (and living) in the Thomas building has been an overall positive experience. It has been a rough ride but thanks to the following people (and many more), I have survived being the "most bitter man in Thomas".

Lynn	Patrick	Prashant	Gustavo
Dan	Guillaume	the Guyader's	the Clinton's
Eric	Linda	Isaac	Rob
Jeff	Tracy	Al	the Caltech rugby team

The support and constant encouragements from my parents kept me strong and focused during the darker times. Finally, this work would not have been possible without the love and support of my wife, Stacey, whom I love very much.

This work was sponsored by the NIH Grant PO1 DK43881.

Abstract

Lithotripsy is at the forefront of treatment of kidney stones. By firing shock waves at the stone, it can be broken down into small fragments. Although the treatment is non-invasive, both short- and long-term side effects occur. In order to understand and rectify these shortcomings, lithotripsy has been the subject of ongoing research. Based on *in vitro* experiments, it has been ascertained that the cloud of cavitating bubble produced in the wake of the shock wave is a crucial element in the stone comminution process.

Various solutions designed to maximize stone comminution and/or decrease tissue damage have been proposed over the years. However, the particulars of the comminution mechanism(s) are still undetermined.

In this work, a numerical model of the two-phase flow inside an electrohydraulic lithotripter was used to provide additional insight in the behavior of the bubble cloud. The numerical model is based on an ensemble averaged two-phase flow model for a compressible liquid. The differential equations were discretized following the WENO shock capturing scheme in prolate spheroidal and cylindrical coordinate systems. The initial conditions for the flow field are estimated based on empirical observations and then validated by comparing the predicted pressure measurements and bubble cloud behavior against experimental values.

In order to gain additional insight in the mechanism for stone comminution, a variety of relevant initial conditions were modeled. The following lithotripter configurations were analyzed: free-field, dual-pulse and single-pulse with an artificial stone at the focus. The impact of parameters such as the intensity of the initial shock wave and the pulse rate frequency (PRF) has been investigated. Based on an energy argument, conclusions regarding the efficiency of stone comminution are presented. In addition, based on these conclusions, avenues for improvement of the numerical model are highlighted.

Contents

List of Figures

List of Tables

Nomenclature

Roman characters

A	Radius of the bubble cloud
B	Coefficient in Tait's equation of state for water
$C(t)$	Scalar function
C	Speed of sound in liquid
C	Concentration of gas dissolved in liquid
D	Diffusivity of gas in liquid
d	Half focal length
$\mathcal{C}$	Set of bubble state variables
F_1	First focus of the lithotripter and origin of the wave
F_2	Second focus of the lithotripter and target of the wave
H	Enthalpy-like property for Gilmore bubble model
h	Coordinate system metric
$\mathbf{I}$	Identity matrix
IS_i	Measure of smoothness for polynomial template
L	Matrix of left eigenvectors
$\mathbf{M}$	Jacobian matrix
Mc	Reynolds stress tensor
N	Number of bubbles and bubble number density
$\mathbf{n}$	Normal vector
P, p	Pressure
P_B	Pressure at the exterior of the bubble surface
$\mathcal{P}$	Probability density distribution

R	Bubble radius
R	Matrix of right eigenvectors
r	Distance
$\dot{R}$	Bubble radial velocity
Re	Reynolds number
S	Surface tension
$\mathbf{s}$	Position vector
dS	Differential surface of integration
T	Temperature of bubble
t_c	Time to collapse for a bubble
$\mathbf{u}$	Liquid or mixture velocity
dV	Differential volume of integration
$\mathbf{w}$	Bubble translational velocity
We	Webber number
$\mathbf{y}$	Bubble location

Greek characters

α	Coefficient in Tait's equation of state for water
α	Polytropic exponent for equation of state of gas
β	Volume fraction
χ	Indicator function
δ	Dirac delta function
η	Curvilinear coordinates
γ	ratio of specific heats for gas
Λ	Matrix of eigenvalues
ρ	Density
ϕ	Potential field
ϕ_i	Scalar variable
Φ_i	Volume average of scalar variable
σ	Cavitation number

ζ	Curvilinear coordinates

Subscripts

$_{\text{air}}$	Non-condensible gas in the bubble
$_{C}$	Liquid or continuous phase
$_{D}$	Bubble or disperse phase
$_{M}$	Mixture phase
$_{o}$	Initial or reference value
$_{\text{rel}}$	Difference between liquid and bubble phase
$_{\text{vap}}$	Condensible vapor in the bubble
$_{\text{wall}}$	At bubble interface
$_{\infty}$	At infinity

Chapter 1

Introduction

Shock wave lithotripsy is the most common treatment for kidney stone disease. This form of therapy was developed over twenty years ago, and has proven to be fast, effective, and relatively free from the trauma and expense associated with surgery. Extracorporeal shock wave lithotripsy (ESWL) works by firing focused shock waves at the kidney stone inside the patient. A typical treatment consists of firing from one to three thousand shock waves at a rate of around one Hertz. The appropriate number, rate, and intensity of shock waves for a particular treatment is based on size, shape, composition, and location of the stone.

Different types of lithotripters have been approved for clinical use and are classified by the type of shock wave source they utilize. Figure 1.1 illustrates some particular configurations. In this study, we will focus on the Caltech-EHL which is a research electrohydraulic lithotripter based on the Dornier HM3 commercial lithotripter. A diagram of the lithotripter used in this study with relevant dimensions is shown in Figure 1.2.

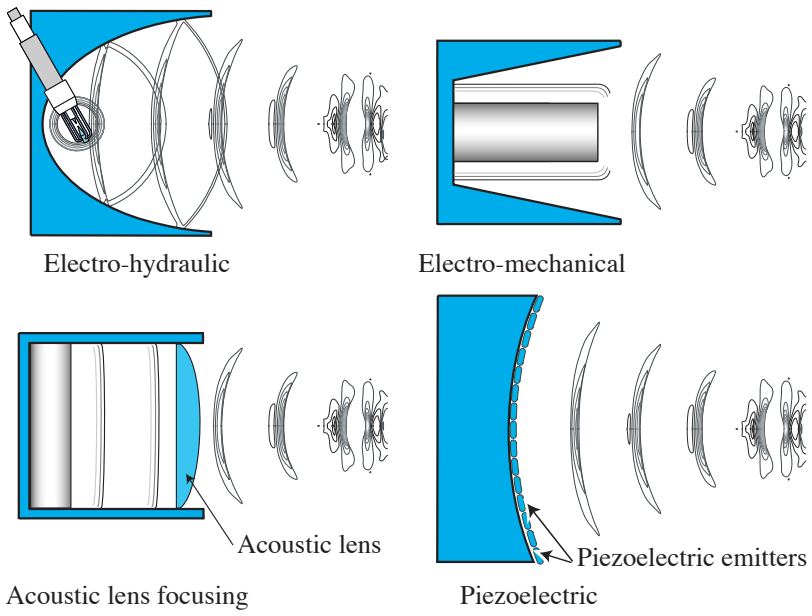

Figure 1.1: Classification of lithotripters.

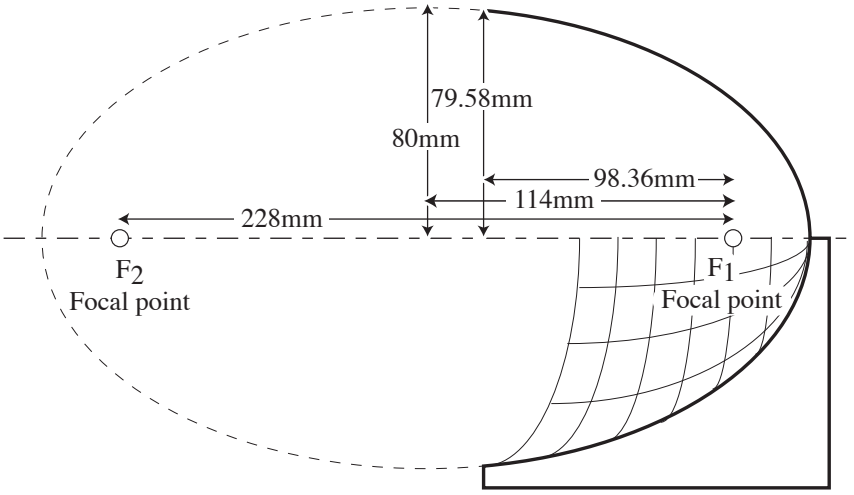

Figure 1.2: Dimensions of the reflector used for this study.

Although effective in breaking kidney stones, ESWL can also cause significant short- and long-term damage to the kidneys. Damage has been observed on both cellular[1] and systemic level[2]. A common side effect of a lithotripsy treatment is the presence of blood in the urine (hematuria). Typical legions in the

[1]See work of Blomgren *et al.* (1997), Lifshitz *et al.* (1997), Connors *et al.* (2000), Lokhandwalla *et al.* (2001), Paterson *et al.* (2002a) and Sapozhnikov *et al.* (2002)
[2]See work of Evan *et al.* (1997),Evan *et al.* (1998) and Connors *et al.* (2000)

kidney tissue caused by an ESWL treatment can be seen in Figure 1.3. Therefore, the shock wave dosage must be carefully prescribed to prevent loss of kidney function.

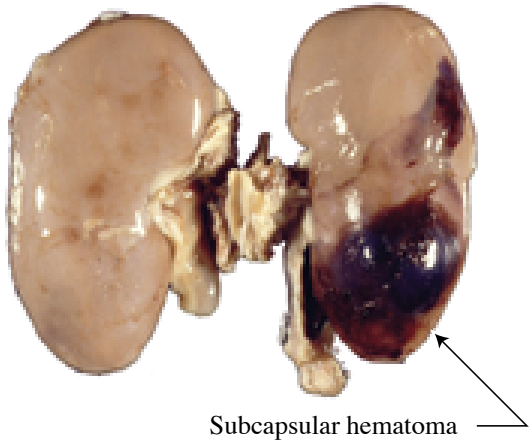

Figure 1.3: Damage to pig kidney after shock wave lithotripsy treatment. Courtesy of Philip M. Blomgren, Department of Anatomy and Cell Biology, Indiana University School of Medicine, Indianapolis.

Because of widespread use of lithotripsy and potential side effects, there have been numerous research efforts aimed at understanding the mechanisms of stone breakage and tissue damage. The exact mechanisms for stone comminution are still a topic of debate. Figure 1.4 illustrates two mechanisms that have been substantiated by empirical observation: spallation and erosion. Spallation is a material failure caused by tensile stress produced as the compressive part of the lithotripter wave is reflected by the distal stone–liquid interface as a tensile wave. In the case of a cylindrical artificial stone, this reflected wave combines with the tensile tail of the incident wave to produce a plane of maximum tensile stress that can cleave the stone. Erosion is caused by the action of cavitation bubbles near the stone. The tensile component of a lithotripsy shock wave typically generates a cloud of cavitating bubbles that collapse violently after the passage of the wave. Pitting is likely caused by micro-jetting or secondary shock wave generation during violent bubble collapse. The bulk of the empirical evidence suggests that cavitation is an important comminution mechanism (Crum 1988, Sass *et al.* 1991, Sass *et al.* 1992, Coleman & Saunders 1993 and Bailey *et al.* 2003).

Regarding cavitation, previous research has focused on determining the pressure field produced by a particular lithotripter, and the response of a single bubble at the lithotripter focus. The following sections present an overview of the previous research and also motivate the need for a more detailed modeling of cavitation in lithotripsy such as the present work.

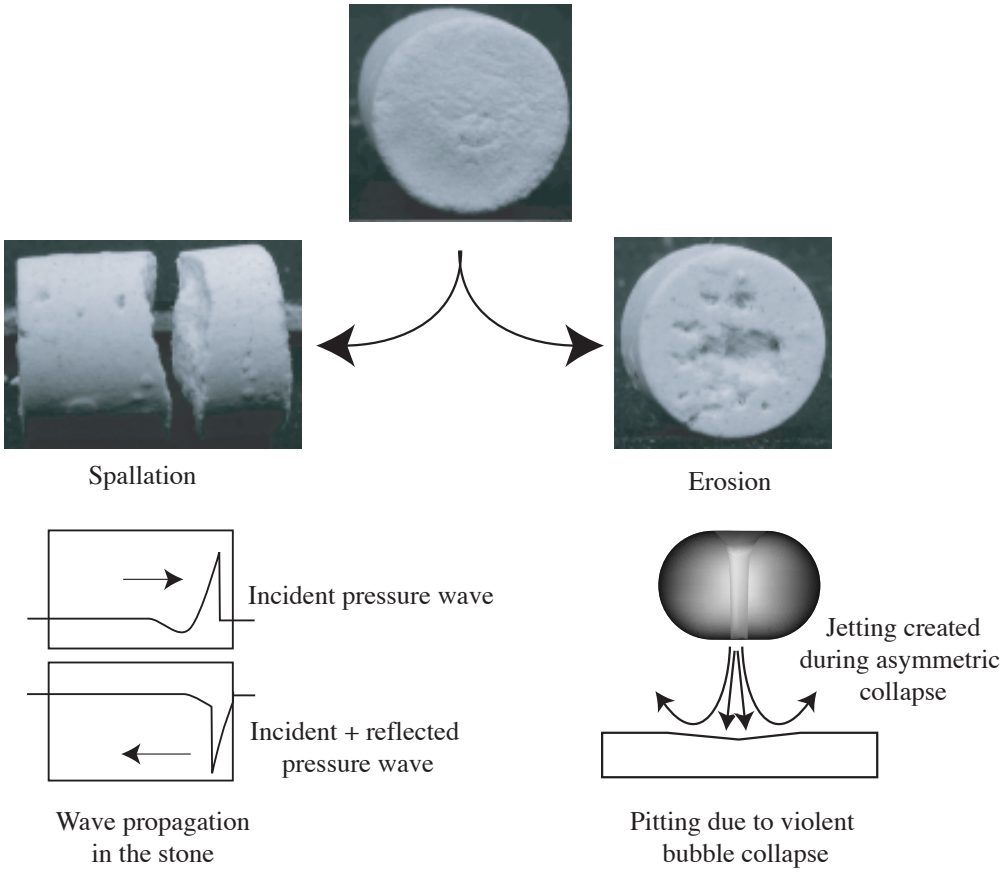

Figure 1.4: Mechanisms of stone comminution. Photographs courtesy of Erin Hatt, Department of Anatomy and Cell Biology, Indiana University School of Medicine, Indianapolis.

1.1 The pressure field produced by a lithotripter

The pressure field in an electrohydraulic lithotripter can be decomposed into several components. The initial shock wave is generated by the discharge across a spark gap (see Figure 1.5 and ① in Figure 1.6) located at the first focus of an ellipsoidal reflector. Since the reflector is not a complete enclosure, part of the shock wave is reflected towards the second focal point (reflected wave) while the rest expands unhindered (incident wave) (② and ③ in Figure 1.6). A diffraction or "edge" wave is created as the shock wave reaches the edge of the reflector (③ in Figure 1.6).

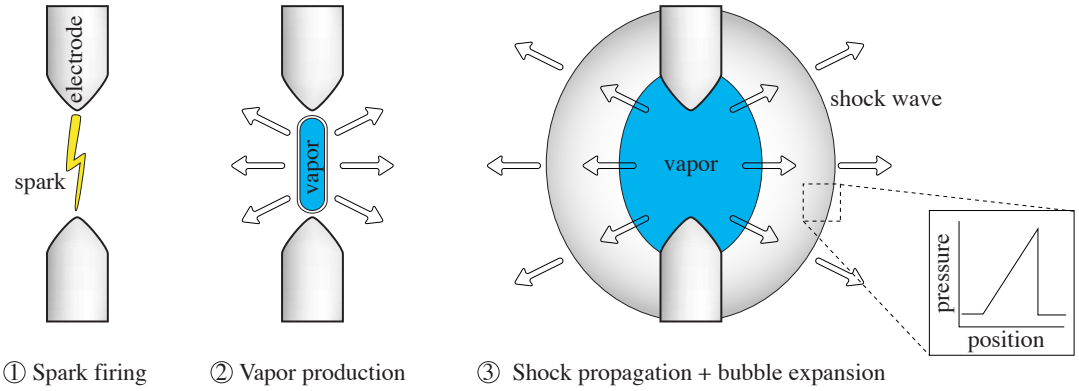

Figure 1.5: Initial shock wave generation.

Based on the work of Cole (1948) on underwater explosions, the initial shock wave generated by the spark gap can be approximated by a positive triangular pulse. As the spherical wave expands and reflects from the ellipsoidal surface, a region of negative pressure (tensile stress) develops because of curvature mismatch and finite wave thickness, as we show in Section 3.1.1. Therefore a pressure wave of large negative pressure can propagate in the liquid without generating a vapor explosion.

As the shock wave reaches the edge of reflector, an additional tensile wave (edge wave) is produced as a consequence of diffraction. The edge wave combines with the tensile tail of the reflected wave near the second focus of the reflector to produce the negative pressure tail as seen in Figure 1.7.

Many empirical measurements of the pressure field for the Dornier HM3 lithotripter have been reported in the work of Coleman *et al.* (1987) and (Müller) (1989, 1990). Because of difficulties in accessing clinical machines, a research lithotripter (Caltech-EHL) was designed after the HM3, and its pressure field was characterized in a similar manner (Cleveland *et al.* 2000). A typical measurement for the pressure at the focus (F_2) of the Caltech-EHL is shown in Figure 1.7. Although the pressure profile can vary significantly from lithotripter to lithotripter, the basic shape remains essentially the same. The peak pressure of the shock

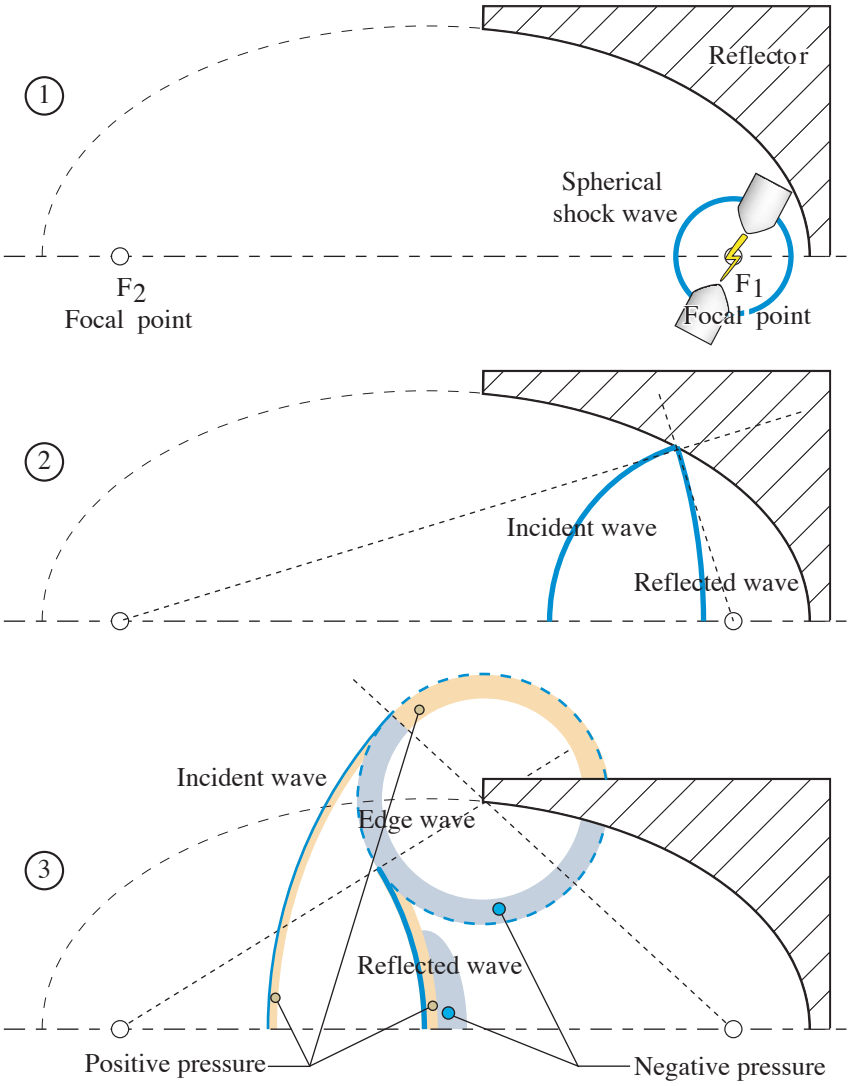

Figure 1.6: Shock wave propagation in an electrohydraulic lithotripter.

wave ranges from 20-100 MPa while the maximum negative pressure can vary from 7 to 15 MPa. Figures 1.8 and 1.9 present average pressure measurements made on the same lithotripter using a membrane and a fiber optic hydrophone, respectively. The bands in the Figures 1.8 and 1.9 represent the bounds for one and two standard deviations (σ) from the average measurement. These measurements are typically performed in clean degassed water for a small number of pulses. The variability is strongly influenced by the degassing and filtration of the water as well as the condition of the spark gap electrode.

Previous researchers have modeled the pressure field using linear and nonlinear acoustics. These models have an advantage over models based on the full equations (as considered here) in that they are not adversely

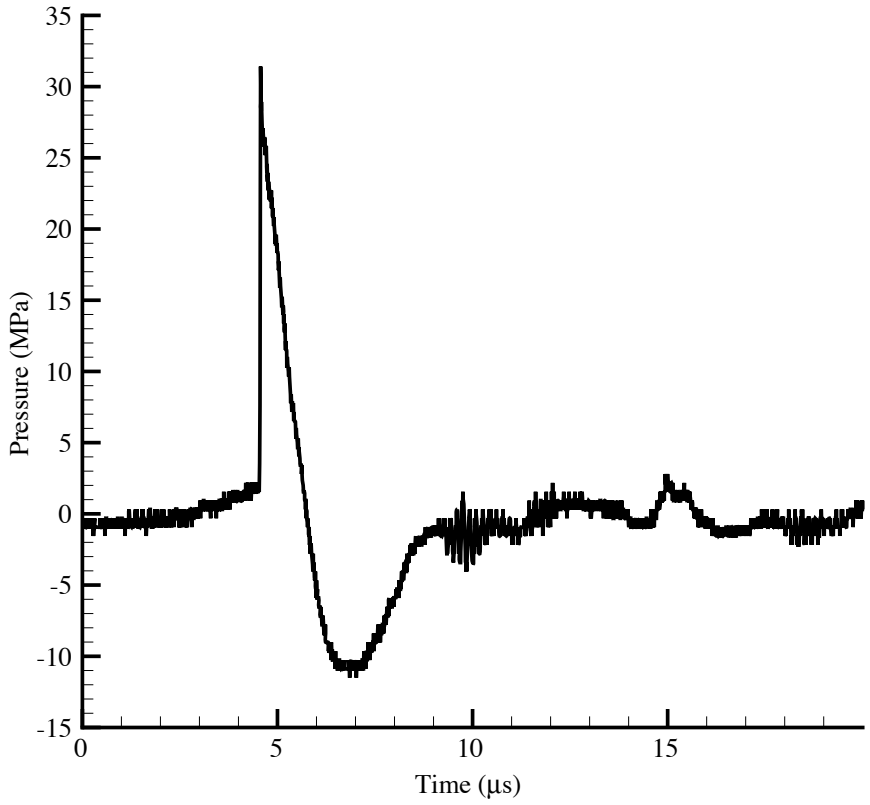

Figure 1.7: Experimental pressure measurement at the focal point of a Caltech-EHL lithotripter. Data courtesy of Michael R. Bailey, Center for Industrial and Medical Ultrasound, Applied Physics Lab, University of Washington, Seattle.

affected by the presence of the shock front; however, some form of modeling must be introduced to account for diffraction effects at the edge of the reflector. In the work of Hamilton (1993), the spherical wave was propagated to the wall of the reflector using linear geometrical acoustics and the reflection (and corresponding diffraction) were calculated analytically using the Kirchoff integral method (see the work of Born & Wolf (1980)). Similarly, Christopher (1994) reported pressure field results for the HM3 using a non-planar source algorithm. The work of Coleman *et al.* (1991) and Averkiou & Cleveland (1999) used models based on the KZK equation (see Zabolotskaya & Khokhlov 1969 and Kuznetsov 1970). Averkiou & Cleveland (1999) reported some agreement between the numerical model and experimental results. A different approach based on geometrical shock dynamics was used in the work of Cates & Sturtevant (1997). This approach is particularly suited for the propagation of strong shock waves and can represent the formation of a triple shock intersection.

The above-mentioned approaches are based on approximations to the Euler equations, and they do not

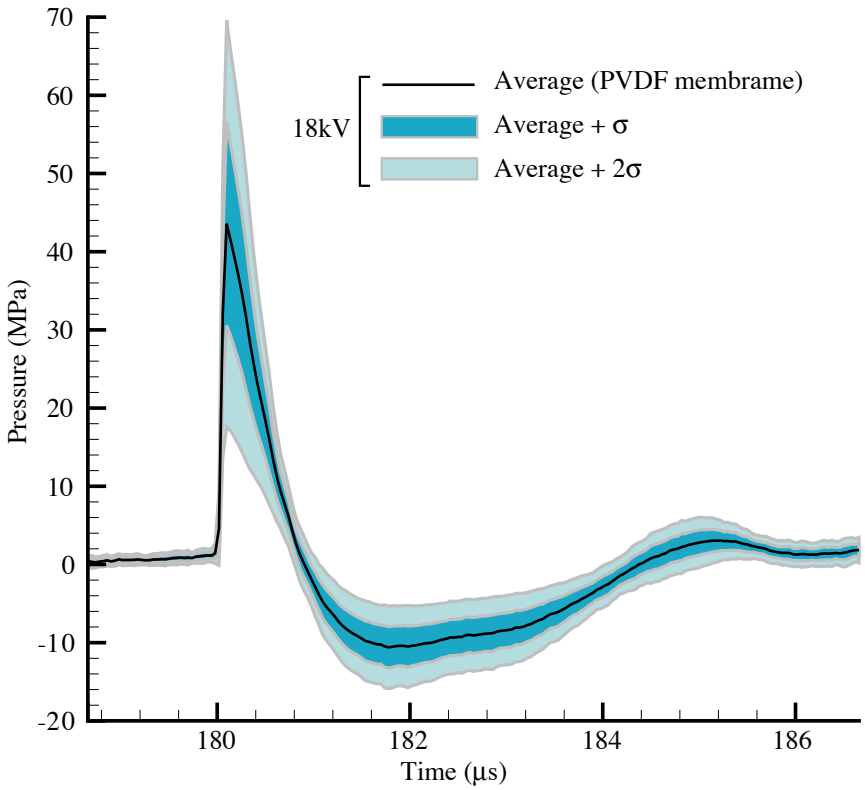

Figure 1.8: Average pressure measurement and variability (40 points) at the focal point of a Caltech-EHL (GALCIT) using PVDF membrane hydrophone at 18 kV. Data from (Cleveland *et al.* 2000).

represent all the wave features (nor the impact of cavitation). In the present work the pressure field is modeled by solving the full Euler equations which have been appropriately modified to account for the presence of bubbles. This model has the advantage of being able to fully represent diffraction. However, it does require a special algorithm for the propagation of shock waves, which are discussed in Section 2.5. In this area, several methods have been developed over the years to overcome problems related to shock induced spurious oscillations. For the purpose of this work, we have used the Weighted Essentially Non-Oscillatory method (WENO) developed originally by Liu *et al.* (1994). This approach ensures that only smooth polynomials are used in the construction of the finite difference template and prevents the formation of these oscillations.

1.2 Bubble dynamic response to the pressure field

As mentioned in the previous section, the pressure experienced in the focal area is composed of a high amplitude shock wave followed by a smooth tensile region that can be over one hundred atmospheres below

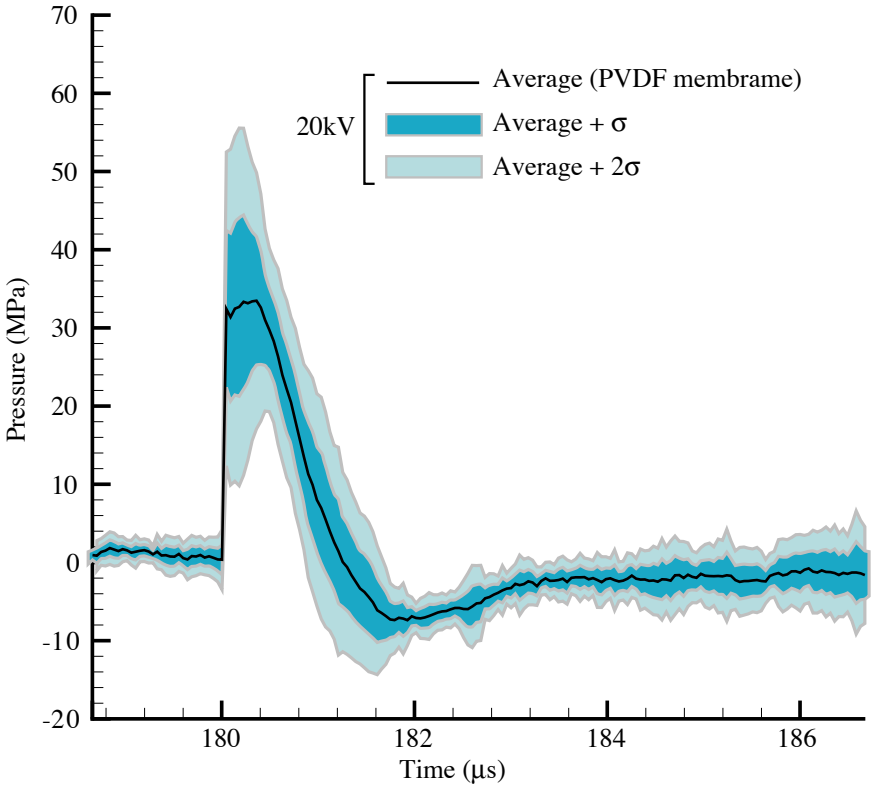

Figure 1.9: Average pressure measurement and variability (10 points) at the focal point of a Caltech-EHL (GALCIT) using a fiber optic hydrophone at 20 kV. The presented data is a courtesy of Robin O. Cleveland, Department of Aerospace and Mechanical Engineering, Boston University, Boston (2003).

the vapor pressure of water. Even though this loading only lasts for a few microseconds, it is more than sufficient to nucleate cavitation bubbles. Although degassing and filtering can be used to control the density of sites (small bubbles, impurities, etc.), it is not possible to control the nuclei *in vivo*. The study of the bubble field during lithotripsy poses several challenges. The density of bubble nucleation sites cannot be measured *a priori* because of their small size (see Appendix F for more details). In addition, bubble activity resulting from the passage of the shock wave only lasts for a fraction of a millisecond and high-speed cameras are needed to capture the details of the bubble cloud. Figure 1.10 shows a sequence of photographs of a typical cavitation cloud in the Caltech-EHL. On these photographs, the bubbles appear as dark spheres. At the scale shown here, only larger bubbles can be seen (bubble radius of at least 0.1 mm). The largest bubbles observed are of the order of 1 to 1.5 mm in diameter. Bubble nuclei are evenly distributed within the field of the lithotripter; however, as seen in Figure 1.10, only the bubbles located in a cigar-shaped region near the focal point achieve significant growth and duration.

In addition to high-speed photography, other diagnostic tools have been used to characterize the bubble

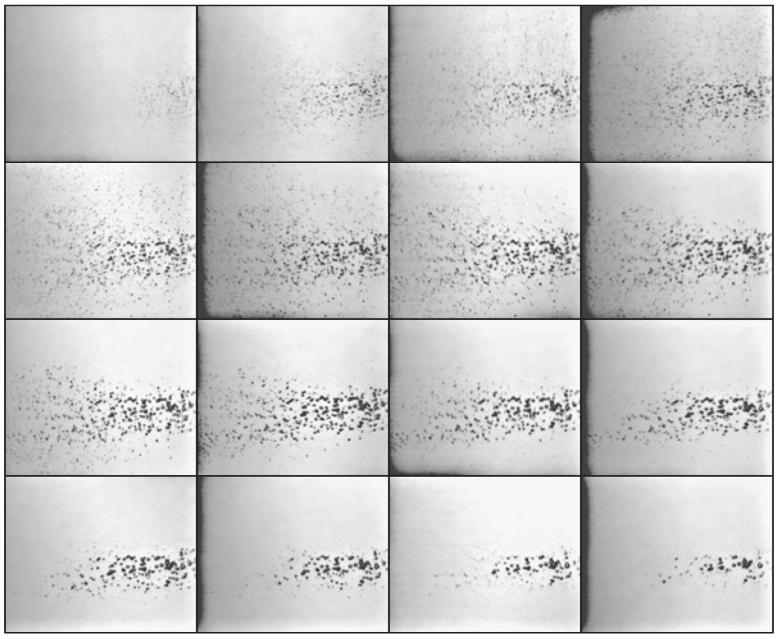

Figure 1.10: High-speed photographs of the bubble cloud in a Caltech-EHL lithotripter. Courtesy of Dahlia L. Sokolov, Center for Industrial and Medical Ultrasound, Applied Physics Lab, University of Washington, Seattle.

field: the passive cavitation detector and laser scattering. The passive cavitation detector (PCD) is composed of a semi-spherical piezoelectric shell and is used to capture spherical acoustic waves produced at the focal point. Because of its construction, only spherical waves emanating from the focal point of the detector will be amplified. The use of laser scattering to measure the bubble radius was first introduced by Jöchle *et al.* (1996) and Hubert *et al.* (1998). By measuring the fraction of laser light scattered by the surface, the bubble radius can be approximated.

Numerical models have also been used to provide a greater understanding of the impact of the shock wave on the bubble field. So far, all models presented have been based on the assumptions that

- the presence of bubbles had no impact on the propagation of the pressure wave,
- there was no interaction between the bubbles.

Empirical measurements of the pressure at the focal point and an approximate curve fit to the data (Church 1989) have been used as input to spherical bubble dynamics models such as the Gilmore equation in order to predict bubble activity at the focus.

More sophisticated bubble models, that account for heat and mass transfer in spherical isolated bubbles, have also been used. The work of Matula *et al.* (2002) compares results from such a model to laser scattering

measurements of the bubble field in the focal region of a lithotripter. The complex model showed some improvements over the conventional Gilmore model and gives predictions for the quantity of noncondensible gas coming out of solution into the bubble. The mass transfer across the bubble interface is an important issue in the impact of the pulse rate frequency. The additional mass in the bubble increases its equilibrium radius which in turn, changes the response to the next lithotripsy pulse. The role of pulse rate frequency has been noted in the work of Hubert *et al.* (1998) and Sapozhnikov *et al.* (2002) and is discussed in greater detail in Section 1.4 of this work. Even though the continuum approach for the bubbly mixture presented in this work does not model discrete bubbles, it does require a model for bubble dynamics in order to determine the internal state of the mixture. For the purpose of this analysis, the Gilmore model was used. Since the internal state of the mixture must be computed at every point in the grid (around 400000 points), the use of a more sophisticated bubble model was not practical. A model similar to the work of Matula *et al.* (2002) and Preston *et al.* (2002) was used as a post-processing stage to determine approximate increases in the bubble equilibrium radii after each pulse.

1.3 Bubble cloud effects in SWL

1.3.1 Mixture compressibility

The presence of bubbles in the liquid can considerably increase the compressibility of the mixture. Using a linearized model for the bubble dynamics, the speed of propagation of small perturbations in a low void fraction mixture can be shown to be

$$\frac{1}{C^2} \approx \frac{1-\beta_D}{C_L^2} + \frac{\beta_D}{\left[\frac{\rho_G}{\rho_L}C_G^2 + \frac{2}{3}\frac{S}{\rho_L R_o} - \frac{\omega^2 R_o^2}{3}\right]}, \tag{1.1}$$

$\omega =$ wave frequency,

where

C	is the speed of sound in the mixture
C_L	is the speed of sound in pure liquid
C_G	is the speed of sound in gas
β_D	is the void fraction
ρ_G	is the density of gas in bubble
ρ_L	is the density of pure liquid
S	is the surface tension
R_o	is the equilibrium bubble size
ω	is the frequency of wave

The resulting speed of sound in the low-frequency limit is plotted in Figure 1.11 as a function of void fraction for typical bubble radii reached in SWL. At low void fractions, the bubbly mixture can have a larger compressibility than either pure liquid or pure gas.

Based on the above result, one might expect the bubble field to have a significant impact on the focusing of the shock wave in a lithotripter. Although the propagation of the reflected shock wave is not significantly affected by the presence of cavitation, the propagation of the edge wave is. As it will be shown in Section 3.1.3, the edge wave expands in the bubbly mixture from the wake of the reflected wave. To our knowledge, this effect has not been analyzed in the literature.

In cases where obstructions are present in the focal area, interaction between the wave propagation and the bubble field are clearly visible. For these cases, part or all of the shock wave is reflected back into a mixture with a rapidly growing void fraction. The reflected waveform can be significantly affected by this rapid change in the compressibility of the mixture.

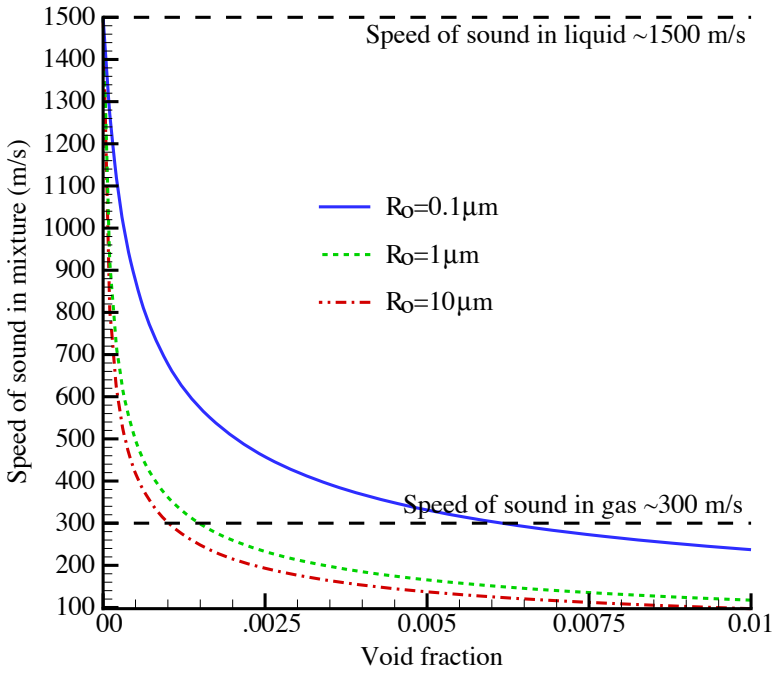

Figure 1.11: Speed of sound as a function of void fraction in the limit of zero frequency for different equilibrium radii.

A clear example of the effect of the bubble field on the wave propagation occurs in dual-pulse lithotripters. As depicted in Figure 1.12, the dual-pulse lithotripter consists of two coaxial conventional electrohydraulic lithotripters firing at the same target. This configuration was originally proposed by Sokolov *et al.* (2001) to improve control of the area of bubble activity. Based on geometrical acoustics, the peak pressure at the focal point is expected to be approximately doubled that of a conventional lithotripter.

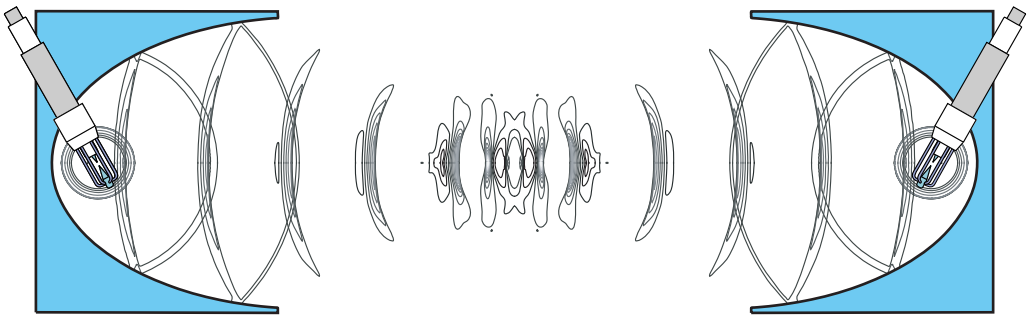

Figure 1.12: Diagram of a dual-pulse lithotripter as proposed by Sokolov *et al.* (2001).

In their study, Sokolov *et al.* (2001) collected high-speed images of the cavitation cloud in the focal region of a dual-pulse lithotripter (see Figure 1.13). As in Figure 1.10, the bubbles in Figure 1.13 appear as dark spots on the image. As anticipated, the bubble cloud in the focal region is much shorter but wider than its

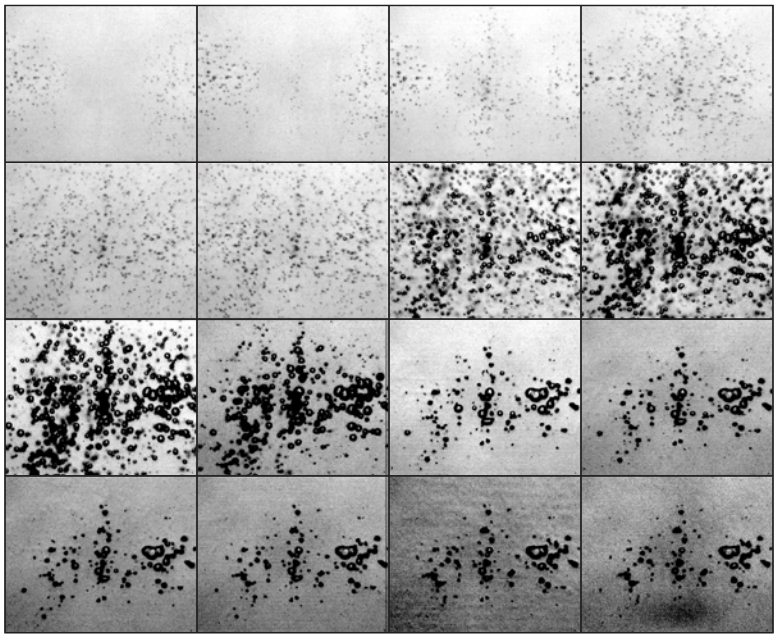

Figure 1.13: High-speed photographs of bubble cloud in a dual-pulse lithotripter. Courtesy of Dahlia L. Sokolov, Center for Industrial and Medical Ultrasound, Applied Physics Lab, University of Washington, Seattle.

single-pulse counterpart (¡50 cm compared to 10 cm). Moreover, pressure measurements at the focal point are approximately twice the amplitude of a single source as predicted by linear acoustics (Sokolov *et al.* 2001). An interesting feature noticeable in Figure 1.13 is appearance of bands where hardly any bubbles can be observed. The presence of these bands of minimal cavitation cannot be explained solely by the superposition of the incident and the delayed reflected wave. Another explanation based on bubble translation was put forward, but no significant bubble motion was observed in experiments (Sokolov *et al.* 2001). In the present work, we propose that this behavior arises from nonlinear coupling between the pressure and cavitation field. Using the numerical model described in this work, it can be shown that this coupling is an essential element to the formation of these structures in the bubble cloud.

1.3.2 Cloud dynamics

For a single bubble in a pure liquid, an analysis can be done to relate the time to collapse of the bubble and its maximum radius. In the work of Lord Rayleigh (1917), an approximate time for the collapse of a spherical cavity filled with vapor only was derived assuming an otherwise uniform incompressible flow field:

$$\text{Rayleigh collapse time: } t_{c/2} = 0.915 R_{\max} \sqrt{\frac{\rho}{P_\infty - P_v}}. \tag{1.2}$$

This derivation can also be extended to the growth of a bubble under certain conditions. For the cases prevalent in lithotripsy, a short duration high intensity pressure pulse perturbs a field of very small bubbles. Typically, the timescale associated with the pulse (5–10 μs) is much shorter than that of the bubble growth (150–300 μs). Given this large difference in timescale, the pressure pulse can be approximated by a impulse acting on the surrounding liquid. The ensuing bubble growth is then caused by the inertia of the moving liquid. For large bubble growth, the bubble interior can be approximated as being composed entirely of vapor. Given these assumptions, bubble growth is equivalent to a reverse collapse phase. Therefore, under these conditions, the total time to collapse for such a bubble is then twice the Rayleigh collapse time:

$$t_c = 1.83 R_{\max} \sqrt{\frac{\rho}{P_\infty - P_v}}. \tag{1.3}$$

This simple result is interesting in that it predicts a linear relationship between the maximum bubble radius and its lifetime given an impulse-like pressure perturbation. In Figure 1.14, this result is compared to Rayleigh-Plesset and Gilmore bubble models forced by shock waves based on Church's model for a pressure wave at the focus of a lithotripter (see Church 1989 and Figure 1.15). The maximum bubble size and time to collapse obtained from either numerical models agreed well with the above theoretical prediction.

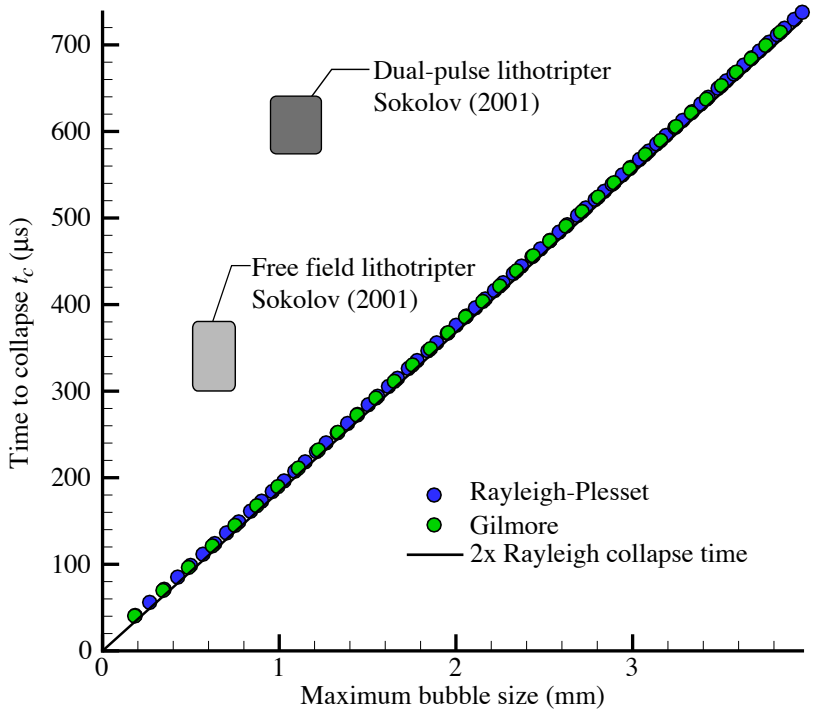

Figure 1.14: Relationship between time to collapse and maximum bubble radius.

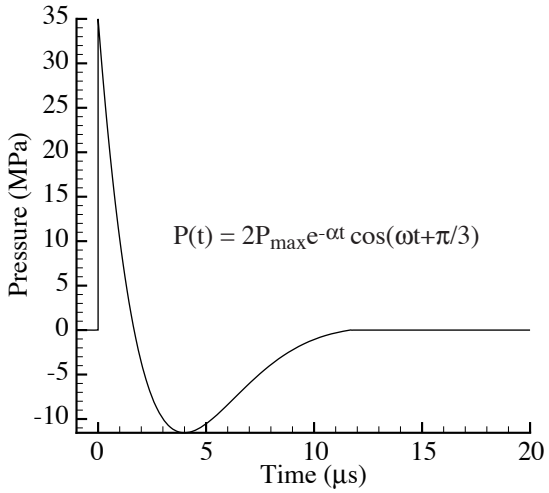

Figure 1.15: Pressure trace for a Church model waveform.

The linear relationship between the maximum bubble radius and time to collapse is particularly interesting in that it is not applicable in cavitating bubble clouds where the void fraction is non-negligible. Collective bubble behavior can differ greatly from that of individual bubbles. As seen in the work of Brennen (1995), Wang & Brennen (1995), Wang (1996), and Reisman *et al.* (1998), the growth and duration of bubbles within a cloud can greatly vary depending on position. In Reisman *et al.* (1998), a numerical model of a spherical bubble cloud was implemented and its response to a far field pressure fluctuation was analyzed (see Figure 1.16). Their results have shown that bubbles in the center of the cloud are partly shielded from the pressure fluctuation and do not grow as much as bubbles located near the edge. However, because of the coupling between the bubble cloud and the flow field, the bubbles at the core of the cloud exhibited a longer collapse time. During the expansion of the bubbles within the cloud, the surrounding liquid must flow outward in order to make room for the volume occupied by the growing bubbles. As a consequence of this flow field, the pressure decreases within the bubble cloud. Subjected to slightly lower pressures, bubbles at the core of the cloud expand for a longer duration.

The above results help explain observations made at the focal point of a lithotripter. Sokolov *et al.* (2001) reported approximate maximum bubble radii of 0.5 mm and 1.1 mm for free-field and dual-pulse lithotripter, respectively, and a time to collapse of 340 ± 31 μs and 608 ± 33 μs for each configuration. As shown in Figure 1.14, these values fall far from the theoretical prediction.

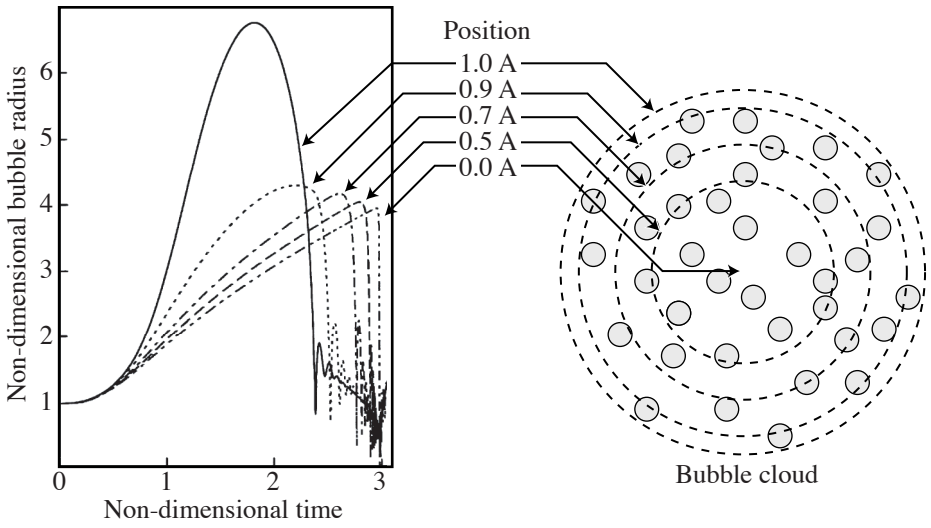

Figure 1.16: Comparison between the bubble response at different location within a bubble cloud of radius A. From the work of Reisman *et al.* (1998).

1.4 The role of pulse rate frequency in lithotripsy

A feature specific to treatment by lithotripsy is the rate at which the shock waves are delivered. Experimental studies have been conducted on this topic and have concluded that the firing rate of the lithotripter has a measurable impact on the effectiveness of the treatment (Paterson *et al.* 2002b). Frequency of pulses of 2 Hz and 1 Hz (which are typical rates used by clinicians) was found to be less effective in stone comminution than a rate of ½ Hz. A plausible explanation for this observation is that a higher PRF frequency leads to larger bubbles in the focal region that in turn, would deflect part of the shock wave and shield the stone (Bailey *et al.* 2003). During the period of large bubble growth, the non-condensible gas dissolved in the liquid diffuses into the bubbles. After they collapse, this gas remains trapped in the bubbles since the surface area available for diffusion is reduced by five to six orders of magnitude. Because of this one-sided diffusion, the equilibrium size of bubbles would then increase, raising the compressibility of the mixture which in turn, diverts more of the acoustic energy of the shock waves away from the objective. Based on this reasoning, it follows that a larger time delay between pulses would allow a greater amount of noncondensible gas to dissolve back into the liquid phase.

1.5 Overview of the thesis

This study provides a first complete numerical model for an electrohydraulic lithotripter where both pressure and bubble field are predicted conjointly. Unlike some of the previous works in this area, empirical measurements are only used to assist in proposing and validating initial conditions. Moreover, the mathematical model for the wave propagation is not approximated and can fully describe all relevant features. In addition to providing a virtual model for the lithotripter, this work also permits the analysis of the energy released by bubbles within the focal region. Although no direct quantification of comminution potential can be made, a measure based on the energy released by the bubbles is used as a surrogate. This approach differs from past work in that it considers the overall behavior of the bubble cloud and how it influences individual bubble dynamics. Based on this analysis, new recommendations can be formulated to improve the effectiveness of the treatment.

Chapter 2

Simulation model

2.1 Equations for continuum-based two-phase flow model

Numerical models for bubbly cavitating flow can be divided into two categories:

- a discrete approach where individual bubbles are tracked in the fluid and the coupling interaction is applied directly,
- a continuum model where the coupling between the bubble and pressure field is averaged in some way.

The first approach has the advantage of requiring less modeling, and has the potential of representing any type of bubbly flow. However, it is also computationally intensive. To be effective, flow features must be resolved on the order of the bubble size (microns in this case) and the axisymmetry of the lithotripter configuration can no longer be exploited. Numerical approaches are being developed for this kind of simulation but, at this stage, simulations with several thousands of bubbles are not practical.

In cases where the solution is not strongly dependent on the initial configuration of the bubbles, the spatial distribution of bubbles can be represented by a continuous number density field. This field describes the probability of finding bubbles at a given location. Similarly, the states of bubbles can be described with field variables. The coupling between the bubble field and pressure field is achieved by averaging. Two different types of averaging have been proposed in the past: volume averaging (Biesheuvel & van Wijngaarden 1984) and ensemble averaging (Zhang & Prosperetti 1994). For either case, the derivation of a closed system of homogenized equations requires that variations in the bubble states and number density field are small compared to the length-scales associated with the mixture flow field.

2.1.1 Flow field in the vicinity a bubble

The flow field in the neighborhood of a bubble can be very complex in general. In order to reduce the complexity of the numerical model to a manageable level, several assumptions regarding the flow field surrounding the bubble are necessary. In this work, the first assumption used is that bubbles remain spherical at all times. This has for direct consequence that bubble fission and fusion are neglected. An equally important assumption made in this work is that bubbles are sufficiently far apart to neglect direct bubble–bubble interactions which is typically valid for void fractions less than a few percent. The third assumption made here is that the fluid is inviscid and the fourth is with regards to whether or not the fluid is compressible.

2.1.1.1 Incompressible fluid

If the fluid surrounding a spherical bubble is inviscid and incompressible, it can then be represented by a potential function. Since the bubble is assumed to be spherical, it is limited to radial and translational motion. The kinematic boundary condition on the bubble-liquid interface is

$$(\nabla\phi - \mathbf{w}) \cdot \mathbf{n} = \dot{R}. \tag{2.1}$$

The total force applied by the liquid in the radial direction on the bubble-liquid interface must balance the force from the gaseous interior:

$$\int_{\text{bub surface}} p dA = 4\pi R^2 p_B. \tag{2.2}$$

As for translational motion, since the bubble is effectively massless, the net force applied on the bubble must be equal to zero.

$$\int_{\text{bub surface}} p\mathbf{n} dA = 0 \tag{2.3}$$

Given the above assumptions, equations for the rate of change of the bubble radius and position can be obtained. These classical derivations are presented in Appendix C and only the final equations are discussed here. From the radial force balance (equation 2.2), one obtains the Rayleigh-Plesset equation:

$$R\ddot{R} + \frac{3}{2}\dot{R}^2 - \frac{1}{4}(\mathbf{u} - \mathbf{w}) \cdot (\mathbf{u} - \mathbf{w}) = \frac{p - p_B}{\rho}, \tag{2.4}$$

where
- p is the pressure far away from the bubble,
- $\mathbf{u}$ is the velocity far away from the bubble,
- R is the bubble radius,
- $\mathbf{w}$ is the bubble translational velocity,
- p_B is the liquid pressure at the bubble surface.

From the axial force balance (equation 2.3), one obtains the following result:

$$(\dot{\mathbf{u}} - \dot{\mathbf{w}}) = 2\frac{\nabla p}{\rho} - 3\frac{\dot{R}}{R}(\mathbf{u} - \mathbf{w}). \tag{2.5}$$

It is interesting to note that this equation can be rewritten as

$$\frac{d}{dt}\left(\frac{3}{2}R^3(\mathbf{u} - \mathbf{w})\right) = \frac{\nabla p}{\rho}, \tag{2.6}$$

where the bracketed term on the left side is proportional to the added mass of the bubble times the relative velocity of the bubble with respect to the fluid.

2.1.1.2 Compressible fluid

If the fluid surrounding the bubble is compressible, then the finite speed at which waves propagate in the liquid must be considered. Several analyses (Gilmore 1952, Keller & Miksis 1980 and Prosperetti & Lezzi 1986 to name a few) have been presented over the years that introduce first and second order correction for the compressibility. The validity of these approaches is limited to low Mach number (i.e., $\dot{R}/C << 1$ where C is the speed of sound in the liquid and $\dot{R}$ is the bubble radial velocity). However, even at supersonic Mach numbers ($\dot{R}/C > 1$), the model predictions are still close to experimental observations (Gilmore 1952). The model used in this work to predict bubble motion was proposed by Gilmore (1952):

$$\left[1 - \frac{\dot{R}}{C}\right] R\ddot{R} + \frac{3}{2}\left[1 - \frac{1}{3}\frac{\dot{R}}{C}\right]\dot{R}^2 = \left[1 + \frac{\dot{R}}{C}\right] H + \frac{R}{C}\frac{dH}{dt} \qquad H = \int_p^{p_B(R,t)} \frac{dp}{\rho}, \tag{2.7}$$

where p_B is the pressure in the liquid at the surface of the bubble.

For small pressure fluctuations, the bubble radial velocity $\dot{R}$ is much less than the speed of sound in

liquid C and equation 2.7 can be simplified to

$$\frac{\dot{R}}{C} << 1, \tag{2.8}$$

$$H = \int_{p}^{p_B(R,t)} \frac{dp}{\rho} \approx \frac{p_B - p}{\rho}, \tag{2.9}$$

$$R\ddot{R} + \frac{3}{2}\dot{R}^2 = \frac{p_B - p}{\rho} \tag{2.10}$$

which is the same as the Rayleigh-Plesset equation discussed in the previous section.

There is no compressible counterpart to the translation equation 2.3. In cases such as Sokolov *et al.* 2001, the Gilmore equation was used to compute the bubble growth and collapse but used a model based on the incompressible model to determine bubble translation. However, it should be noted that equation 2.3 predicts unrealistic relative velocities for violent bubble collapse.

2.1.2 Phase averaged equations

Given one of the above models for the behavior of an individual bubble, equations for the averaged bubbly mixture can be derived. The phase average for the density and momentum can be expressed as

$$\langle \rho_M \rangle = \beta_C \langle \rho_C \rangle + \beta_D \langle \rho_D \rangle, \tag{2.11}$$

$$\langle \rho_M \mathbf{u}_M \rangle = \beta_C \langle \rho_C \mathbf{u}_C \rangle + \beta_D \langle \rho_D \mathbf{u}_D \rangle, \tag{2.12}$$

$$\beta_C = 1 - \beta_D, \tag{2.13}$$

where the subscripts M, D, C refer to mixture, disperse (bubble) and continuous (liquid) phase properties. In addition, the variable β_D is define as the volume fraction occupied by bubbles or void fraction. Since the density of the liquid is over three orders of magnitude larger than that of the bubble interior, the density of the disperse phase can be neglected:

$$\rho_D \approx 0, \tag{2.14}$$

$$\langle \rho_M \rangle \approx \beta_C \langle \rho_C \rangle, \tag{2.15}$$

$$\langle \rho_M \mathbf{u}_M \rangle = \beta_C \langle \rho_C \mathbf{u}_C \rangle. \tag{2.16}$$

An additional simplification to the above can be obtained by assuming that the fluctuations in the mixture caused by the bubble activity are incompressible. This effectively decouples the density and velocity

fluctuations:

$$\langle \rho_M \mathbf{u}_M \rangle = \langle \rho_M \rangle \langle \mathbf{u}_M \rangle. \tag{2.17}$$

The governing equation for the mixture continuum can be expressed in the following form:

$$\frac{\partial}{\partial t}\langle \rho_M \rangle + \nabla \cdot \langle \rho_M \mathbf{u}_M \rangle = 0, \tag{2.18}$$

$$\frac{\partial}{\partial t}\left(\langle \rho_M \rangle \langle \mathbf{u}_M \rangle\right) + \nabla \cdot \left(\langle \rho_M \rangle \langle \mathbf{u}_M \mathbf{u}_M \rangle\right) + \nabla \langle p_M \rangle = \langle \sigma \rangle. \tag{2.19}$$

Since both phases are assumed to be inviscid, the average stress tensor is zero $\langle \sigma \rangle = 0$. In addition, the momentum convection term can be rewritten in terms of the primitive variables ρ_M and $\mathbf{u}_M$, and a Reynolds stress term:

$$\frac{\partial}{\partial t}\langle \rho_M \rangle + \nabla \cdot \langle \rho_M \mathbf{u}_M \rangle = 0, \tag{2.20}$$

$$\frac{\partial}{\partial t}\left(\langle \rho_M \rangle \langle \mathbf{u}_M \rangle\right) + \nabla \cdot \left(\langle \rho_M \rangle \langle \mathbf{u}_M \rangle \langle \mathbf{u}_M \rangle\right) = -\nabla \langle p_M \rangle + \nabla \cdot \left[\rho_M (\langle \mathbf{u}_M \rangle \langle \mathbf{u}_M \rangle - \langle \mathbf{u}_M \mathbf{u}_M \rangle)\right]. \tag{2.21}$$

In order to close the above set of equations, details regarding the averaging must be introduced. The resulting expression can be dependent on the form of averaging used. For this work, an ensemble phase average based on the work of Zhang & Prosperetti (1994) was used to derive the final equations. A detailed derivation can be found in Appendix C. It is interesting to note that following a different approach to the averaging process, for the same order of accuracy, identical equations can be obtained.

Although the approach for the derivation of the average mixture pressure presented in Appendix C is more rigorous, the same result can be obtained by volume averaging the liquid and bubble pressure:

$$\langle p_M \rangle \approx (1 - \beta_D)\langle p_C \rangle + \beta_D \langle p_B \rangle, \tag{2.22}$$

where p_B is the pressure in the liquid at the surface of a bubble. Similarly, a bubble induced Reynolds stress term can be readily derived by assuming that the local perturbation of the flow field by a bubble is:

$$\mathbf{u}' = R^2 \dot{R} \frac{\mathbf{x}}{r^3}, \tag{2.23}$$

where $\mathbf{x}$ is relative position from the bubble center and $r = |\mathbf{x}|$. The velocity perturbation can then be

integrated to yield

$$\mathbf{u}'\mathbf{u}' = R^4\dot{R}^2\frac{\mathbf{xx}}{r^6}, \tag{2.24}$$

$$\int \mathbf{u}'\mathbf{u}'dV = R^3\dot{R}^2\int_{\text{bub surface}} \mathbf{nn}dA = \frac{4}{3}\pi R^3\dot{R}^2 I, \tag{2.25}$$

where I is the identity tensor. By taking this last result and multiplying it by the number of bubbles present per unit volume, we obtain an expression for the bubble induced Reynolds stress term which is identical to the one found in Appendix C:

$$\langle\mathbf{uu}\rangle = \beta_D\dot{R}^2. \tag{2.26}$$

It should kept in mind that these simple derivations are only applicable for a simple case where the properties of the disperse and continuous phases are approximately uniform over the averaging length-scale. This averaging volume must be sufficiently large such as to contain a large number of bubbles.

2.2 Final equations

The final form of the governing equations for the mixture are (the averaging brackets $\langle\rangle$ and mixture subscript $_M$ have been omitted in order to simplify the notation)

$$\frac{\partial\rho}{\partial t} + \nabla\cdot(\rho\mathbf{u}) = 0, \tag{2.27}$$

$$\frac{\partial\rho\mathbf{u}}{\partial t} + \nabla\cdot(\rho\mathbf{uu}) + \nabla p_C = \nabla\left[\beta_D(p_C - p_B(R) - \rho\dot{R}^2)\right], \tag{2.28}$$

$$p_C - p_o = \frac{\rho_o C^2}{\alpha}\left[\left(\frac{\rho_C}{\rho_o}\right)^{\alpha} - 1\right], \tag{2.29}$$

$$p_B = -\frac{2S}{R_o}\left[\left(\frac{R_o}{R}\right) - \left(\frac{R_o}{R}\right)^{3\gamma}\right] - (p_o - p_{\text{sat vap}})\left[1 - \left(\frac{R_o}{R}\right)^{3\gamma}\right] + p_o, \tag{2.30}$$

$$\rho_C = \frac{\rho}{(1-\beta_D)}, \tag{2.31}$$

$$\beta_D = \frac{4}{3}\pi N\bar{R}^3, \tag{2.32}$$

$$\frac{\partial N}{\partial t} + \nabla\cdot N\mathbf{u} = 0. \tag{2.33}$$

The governing equations for the bubble phase are

$$R\ddot{R} + \frac{3}{2}\dot{R}^2 = \frac{p_B - p_C}{\rho_C}, \tag{2.34}$$

or

$$\left[1 - \frac{\dot{R}}{C}\right] R\ddot{R} + \frac{3}{2}\left[1 - \frac{1}{3}\frac{\dot{R}}{C}\right]\dot{R}^2 = \left[1 + \frac{\dot{R}}{c}\right] H + \frac{R}{C}\frac{dH}{dt} \qquad H = \int_{p_C}^{p_B} \frac{dp_C}{\rho_C}, \tag{2.35}$$

for the Rayleigh-Plesset and Gilmore cases respectively.

2.3 Initial conditions

2.3.1 Bubble field

Establishing appropriate initial conditions for the simulation is difficult. Although the properties of the quiescent liquid can be readily obtained, the distribution of microscopic bubble nuclei cannot be measured empirically while at rest. Therefore, the initial conditions for the bubble field must be estimated and then validated by comparing the resulting larger scale bubble growth and pressure measurement to experimental observations (see Appendix F for details about initial estimates). This iterative process is illustrated in Figure 2.1. Based on past work and available literature, the bubble number density was estimated to be 5–50 bubbles/cm^3 while the equilibrium bubble radius to be 3–50 μm (see Appendix F).

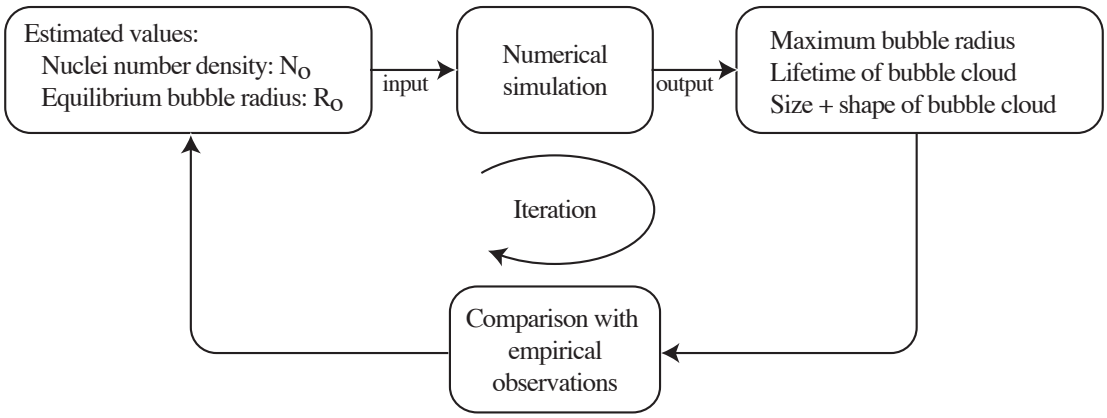

Figure 2.1: Iterative process for initial bubble conditions.

2.3.2 Pressure field at early times

In its early stages of propagation, the spherical shock wave can be modeled using the linearized Euler equations. This is applicable since cavitation effects are negligible[1] until a tensile region develops and the associated velocities are small (negligible momentum convection). Although nonlinear effects are present, this model is sufficient for the purpose of determining the initial condition. In spherical coordinates, the

[1] As mentioned previously, the initial void fraction is negligible and since the wave is strictly positive at this stage, there is no positive bubble growth.

relevant equations are

$$\frac{\partial \rho}{\partial t} + \frac{1}{r^2}\frac{\partial r^2 \rho v}{\partial r} = 0, \tag{2.36}$$

$$\frac{\partial \rho v}{\partial t} + c^2 \frac{\partial \rho}{\partial r} = 0, \tag{2.37}$$

$c =$ speed of sound.

These can be combined to give the wave equation:

$$\frac{\partial^2 \rho}{\partial t^2} + \frac{c^2}{r^2}\frac{\partial}{\partial r}\left(r^2 \frac{\partial \rho}{\partial r}\right) = 0, \tag{2.38}$$

whose solution is

$$\rho = \frac{f(r-ct)}{r} + \frac{g(r+ct)}{r}, \tag{2.39}$$

where the first solution is an expanding wave and the second is an imploding wave. The corresponding velocity field can be found by integration:

$$\rho v = -\frac{1}{r^2}\int \frac{\partial \rho}{\partial t} r^2 dr, \tag{2.40}$$

$$= -\frac{1}{r^2}\int \left[-c\frac{f'(r-ct)}{r} + c\frac{g'(r+ct)}{r}\right] r^2 dr, \tag{2.41}$$

$$= \frac{c}{r}\left(-f(r-ct) + g(r+ct)\right) \tag{2.42}$$

$$+ \frac{c}{r^2}\left(\int^{r-ct} f(z)dz - \int^{r+ct} g(z)dz\right) + \frac{h(t)}{r^2}.$$

where $h(t)$ is a constant of integration. Since the desired initial condition is an expanding wave, the solution should have the following form

$$\rho = \frac{f(r-ct)}{r}, \tag{2.43}$$

$$\rho v = c\left[-\frac{f(r-ct)}{r} + \frac{1}{r^2}\int_0^{r-ct} f(z)dz\right] + \frac{h(t)}{r^2}. \tag{2.44}$$

Because the numerical model does not account for the vapor cavity generated by the spark, the density and velocity fields must be prescribed even at the focal point ($r = 0$) so the integration constant $h(t)$ must be zero. Consequently, a strictly positive pressure wave form would require a non-zero radial velocity field

ahead of the pulse (see Figure 2.2).

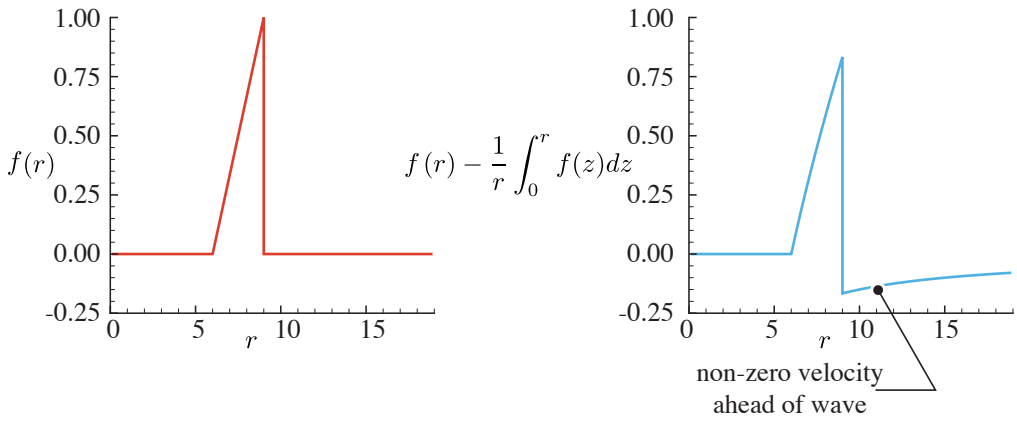

Figure 2.2: Positive pressure waveform and associated velocity field.

This is clearly not an appropriate initial condition for the velocity field. To alleviate this problem an artificial mass source is added to the equations. This source accounts, in a simplified way, for the vapor cavity generated by the spark process.

$$\rho v = \rho v' - \frac{1}{r^2}\int^r S(z)z^2 dz \tag{2.45}$$

$$\frac{\partial \rho}{\partial t} + \frac{1}{r^2}\frac{\partial r^2 \rho v'}{\partial r} = S(r) \tag{2.46}$$

$$\frac{\partial \rho v'}{\partial t} + c^2 \frac{\partial \rho}{\partial r} = 0 \tag{2.47}$$

Since the source term in the continuity equation is independent of time, the second order wave equation for the density 2.38 is still applicable. Therefore, the added mass source, $S(r)$, has no impact on the possible solutions for the density.

$$\rho = \frac{f(r-ct)}{r}$$

$$\rho v' = c\left[-\frac{f(r-ct)}{r} + \frac{1}{r^2}\int_0^{r-ct} f(z)dz\right] + \frac{1}{r^2}\int^r S(z)z^2 dz \tag{2.48}$$

The added source term must satisfy two conditions: the velocity field must be zero ahead of the shock wave

and the velocity must be zero at the center. Using these restrictions, the source term must have the form:

$$\rho v' = -c\frac{f(r-ct)}{r} + \frac{c}{r^2}\left[\int_0^{r-ct} f(z)dz - m_s H(r)\right], \tag{2.49}$$

$$m_s = \int_0^{r_{\text{shock}}} f(z)dz, \tag{2.50}$$

$$H(r) = \begin{cases} 0 & r \ll r_o \\ 1 & r \gg r_o \end{cases} \quad \text{where } r_o \text{ is before the shock wave.} \tag{2.51}$$

Figure 2.3 illustrates the impact of the source term. Curve ① is the uncorrected velocity. Curve ② includes the contribution of a source term satisfying the zero velocity condition ahead of the shock wave but is singular at the origin. The singularity is eliminated in curve ③ with an appropriate shape function $H(r)$. The velocity field behind the expanding shock wave is illustrated in Figure 2.4. The strength of the distributed mass source is constant which provides a constant decaying velocity field between it and the spherical shock wave.

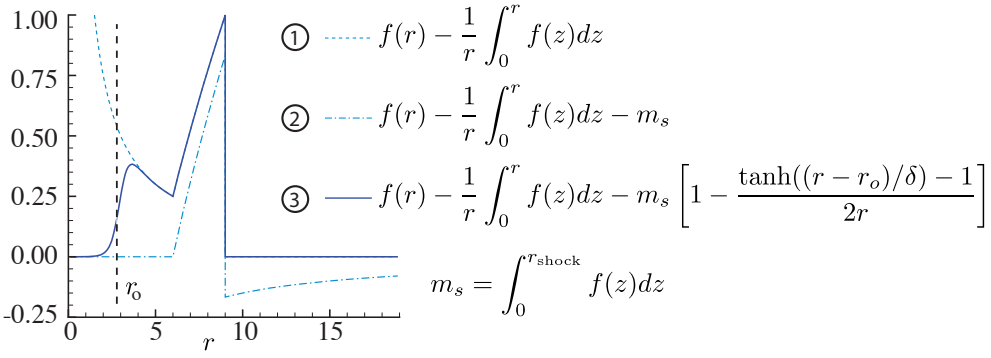

Figure 2.3: Contribution of the source term to the flow field.

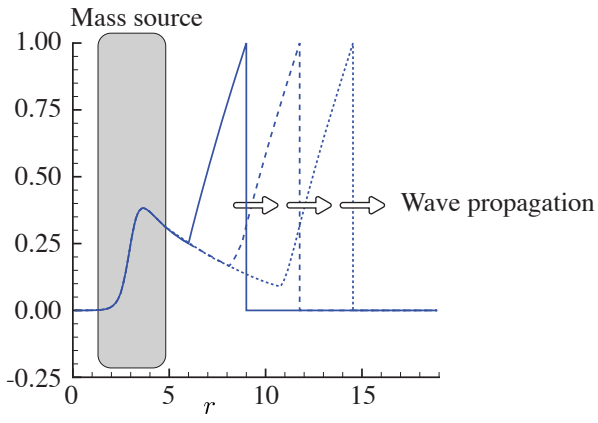

Figure 2.4: Wave propagation and corresponding velocity field.

2.4 Grid and boundary conditions

2.4.1 Computational grid

As mentioned previously, the boundary of the reflector is ellipsoidal. In order to minimize the discretization error in the implementation of the boundary condition, the boundary should coincide with the coordinate axis. In this case, the coordinate system of choice is prolate spheroidal. Given the position vector $\mathbf{R} = (x, y, z)$ defined by

$$\mathbf{R} = \left[\sqrt{\zeta_2^2 + d^2}\cos(\zeta_1), \zeta_2 \sin(\zeta_1)\cos(\zeta_3), \zeta_2 \sin(\zeta_1)\sin(\zeta_3)\right], \tag{2.52}$$

$$\zeta_1 \epsilon [0, \pi], \quad \zeta_2 \epsilon [0, \infty), \quad \zeta_3 \epsilon [0, 2\pi], \tag{2.53}$$

the metrics for this system are found to be

$$h_i = \left|\frac{\partial \mathbf{R}}{\partial \zeta_i}\right|, \tag{2.54}$$

$$h_1 = \sqrt{\zeta_2^2 + d^2 \sin^2(\zeta_1)}, \tag{2.55}$$

$$h_2 = \sqrt{\frac{\zeta_2^2 + d^2 \sin^2(\zeta_1)}{\zeta_2^2 + d^2}}, \tag{2.56}$$

$$h_3 = \zeta_2 \sin(\zeta_1). \tag{2.57}$$

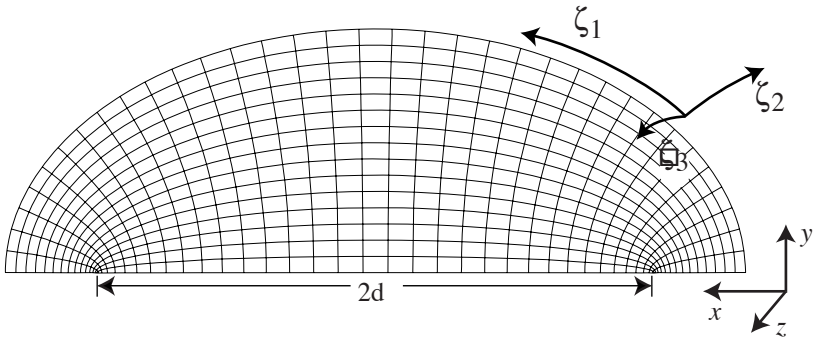

Figure 2.5: Prolate ellipsoidal grid.

Figure 2.5 illustrates the grid. There is a coordinate singularity located at each focal point of the domain. Similar to cylindrical and spherical grids, the distance between two grid points shrinks to zero as one approaches the singularities. Because of the stability requirements for explicit time integration, the

largest stable time step permissible is inversely proportional to the grid spacing. Consequently, the region surrounding the focal point must be treated specially in order to avoid an overly restrictive time step.

The prolate spheroidal grid is ideally suited for the modeling of the reflector. However, in the opposite region of the domain where the shock wave focuses on the target area, a cylindrical grid is better suited for the task. In the computational domain used in this work, both grids were used (see Figure 2.6). On the plane between both focal points, the spheroidal grid meshes to first order accuracy with the cylindrical grid in the axial direction (and exact in the radial direction). Figure 2.7 illustrates the junction between the two grids.

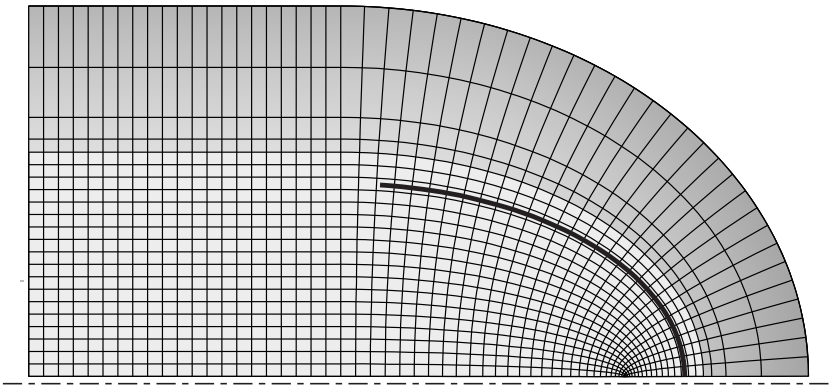

Figure 2.6: Schematic of the computational domain used in this work.

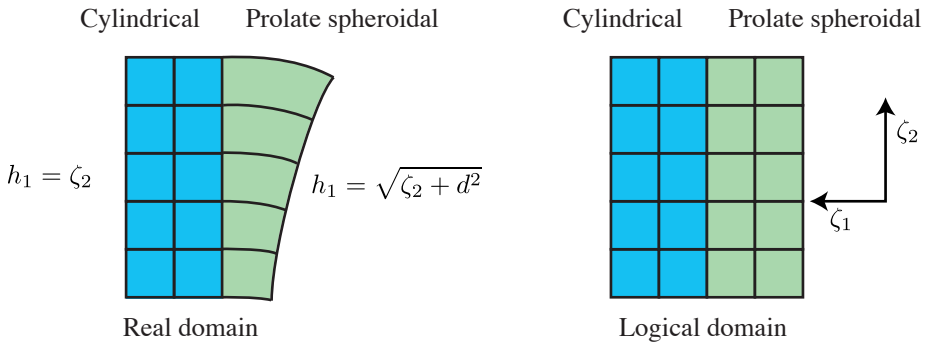

Figure 2.7: Schematic of the junction between prolate ellipsoidal and cylindrical grid.

There is a discontinuity in the derivatives at the junctions between domains. However, as seen from Figure 2.7, the jump between the two metrics grows as

$$h_1^{\text{spheroidal}} - h_1^{\text{cylindrical}} \approx \frac{\zeta_2^2}{2d} + O[\zeta_2^4].$$

The difference is negligible for all but the outer part of the domain. So far, the results obtained with the present model have shown no measurable reaction to this discontinuity in the grid.

2.4.2 Boundary conditions

The following boundary conditions are required for the modeling of a lithotripter:

- centerline boundary at the axis of symmetry
- reflective boundary at the surface of the reflector
- non-reflective boundary at the outer edge of the domain

The implementation of the centerline condition follows from the earlier work of Mohseni & Colonius (2000). In this approach, the first grid point is located half a grid spacing away from the axis of symmetry (see Figure 2.8). Fictitious (reflected) nodes are added to the domain with values taken from their image counterpart. Scalar quantities are mirrored while vector orientations are reflected. Using this approach, the nodes located near the boundary can be treated using the same numerical procedure as interior nodes.

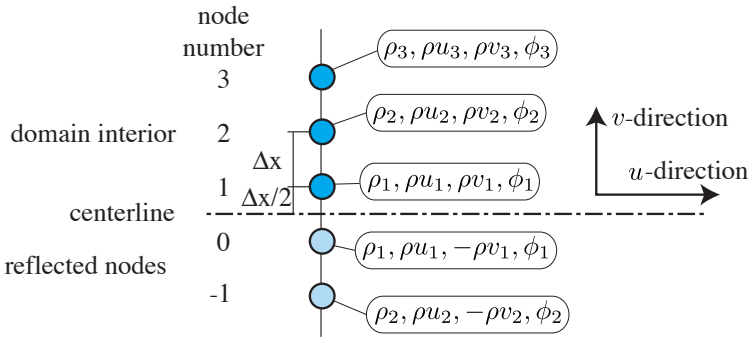

Figure 2.8: Centerline treatment.

A similar treatment is used for the solid boundary of the reflector. As mentioned previously, the fluid mixture is assumed to be inviscid so there can be no mass flow across the solid interface. The following set of equations describes the flow of at the boundary.

$$u_1\Big|_{\text{wall}} = 0, \tag{2.58}$$

$$\frac{\partial u_1}{\partial t}^{0} + \frac{u_1}{h_1}^{0}\frac{\partial u_1}{\partial \zeta_1} + \frac{u_2}{h_2}\frac{\partial u_1}{\partial \zeta_2}^{0} + \frac{\partial p}{\partial \zeta_1} = 0 \quad \rightarrow \quad \frac{\partial p}{\partial \zeta_1}\Big|_{\text{wall}} = 0. \tag{2.59}$$

By applying the same treatment as the symmetry boundary, the no through flow boundary condition can be approximately satisfied.

The treatment of the outer boundary requires a more detailed explanation. The non-reflective boundary condition is based on the work of Thompson (1987). This approach is based on a one-dimensional decomposition of the equation into (approximately) outgoing and incoming waves. This boundary condition is designed to absorb a flat wave hitting the edge of a Cartesian grid. However, in other types of curvilinear coordinates, this method can lead to spurious reflections. The error associated with the approximate boundary condition is inversely proportional to $h_1 h_2 h_3$ so it is minimal sufficiently far away (assuming that the metrics grow monotonically with coordinates). Therefore, given a sufficiently large domain, the Thomson boundary condition can be applied with minimal reflection.

2.4.3 Mesh stretching

Although essential for the accuracy of the non-reflective boundary condition at the outer edge, a larger computational domain is significantly more expensive to compute. To reduce the cost extending the domain, grid stretching is used in the outer part of the domain where accuracy is not a main concern. As discussed in Colonius *et al.* (1993), aliasing can occur in the stretched grid. The high-frequency content of outgoing wave can no longer be represented over the coarser grid and is aliased back into lower frequency wave traveling backwards into the domain. Following the approach of Colonius *et al.* (1993), spatial filtering is used over the outer edge of the grid to progressively eliminate the high frequency modes before they can be reflected.

For the purpose of this work, the following mesh stretching function was used:

$$\zeta_2 = A\left[x - D\log\left(\frac{\cosh((x-C)/D)}{\cosh(-C/D)}\right)\right] + B\left[x + D\log\left(\frac{\cosh((x-C)/D)}{\cosh(-C/D)}\right)\right], \tag{2.60}$$

$$\frac{d\zeta_2}{dx} = \frac{A}{2}\left[1 - \tanh\left((x-C)/D\right)\right] + \frac{B}{2}\left[1 + \tanh\left((x-C)/D\right)\right], \tag{2.61}$$

where

A = normal grid spacing,

B = stretched grid spacing,

C = location where grid stretching begins,

D = width of the transition region.

As mentioned above, filtering is especially necessary in the transition region between the normal and stretched grid. In the present work, a very simple filtering scheme with the following template was implemented:

$$\hat{\phi}_i = a\phi_i + \frac{2}{3}(1-a)\left[\phi_{i+1} + \phi_{i-1}\right] + \frac{1}{6}(a-1)\left[\phi_{i+2} + \phi_{i-2}\right]. \tag{2.62}$$

The parameter a controls the amount of filtering. Figure 2.9 shows the damping as a function of the input frequency. By progressively increasing the filter parameter a, the higher frequency components are eliminated before they can be aliased.

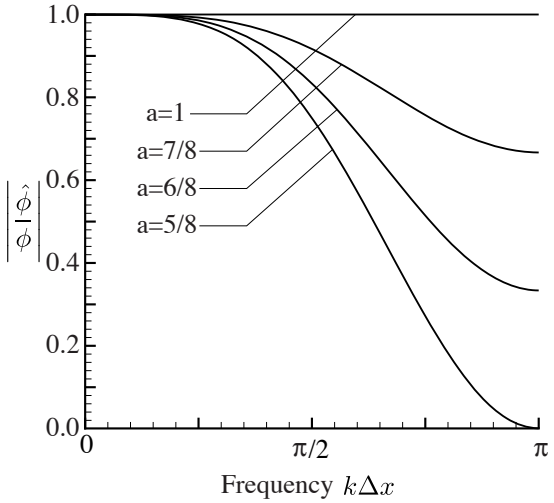

Figure 2.9: Spectral properties of filter.

2.5 Shock capturing algorithm

Typical finite difference methods exhibit poor performance for representing shock waves. As illustrated in Figure 2.10, any polynomial fitting across a steep gradient results in spurious oscillations. Various numerical devices, such as artificial viscosity, have been developed in the past to filter out the high frequency component of the wave. In some cases, these methods can be tuned such as to balance the added dissipation with the production of spurious oscillations.

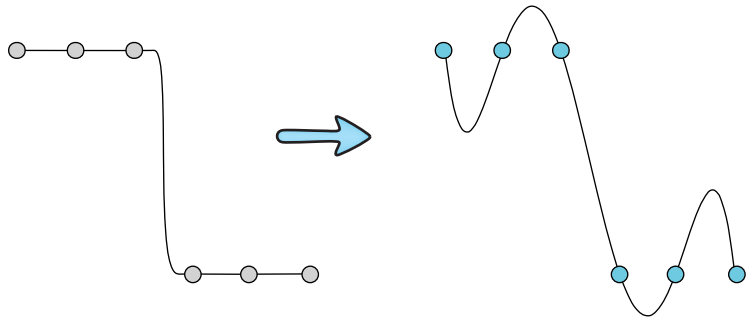

Figure 2.10: Polynomial fitting across sharp discontinuity.

Essentially non-oscillatory shock capturing methods are based on a different approach. Instead of attempting to filter the oscillations generated by the interpolation, these methods are designed to choose the interpolation template that will cause the smallest oscillations (Harten & Osher 1986, Harten *et al.* 1986). To illustrate this approach, let us consider the linear first-order wave equation.

$$\frac{\partial \phi}{\partial t} + U \frac{\partial \phi}{\partial x} = 0. \tag{2.63}$$

If we integrate the above equation over discrete control volumes, we obtain

$$\frac{\partial}{\partial t} \int_{x_{i-1/2}}^{x_{i+1/2}} \phi(x,t) dx + U \left(\phi(x_{i+1/2},t) + \phi(x_{i-1/2},t) \right) = 0, \quad i = 1...n. \tag{2.64}$$

If we use the notation

$$\Phi_i(t) \equiv \frac{1}{\Delta x} \int_{x_{i-1/2}}^{x_{i+1/2}} \phi(x,t) dx,$$

$$\phi_{i+1/2}(t) \equiv \phi(x_{i+1/2},t),$$

then the discretized equations have the form:

$$\frac{\partial \Phi_i(t)}{\partial t} = -\frac{U}{\Delta x}\left(\phi_{i+1/2}(t) - \phi_{i-1/2}(t)\right). \tag{2.65}$$

To solve the above system of ODE's, we must approximate the values of $\phi_{i+1/2}(t)$ given values for $\Phi_i(t)$. Figure 2.11 illustrates the available choices of polynomial for a fourth-order approximation of $\phi_{i+1/2}(t)$. Note that all five polynomials are upstream biased.

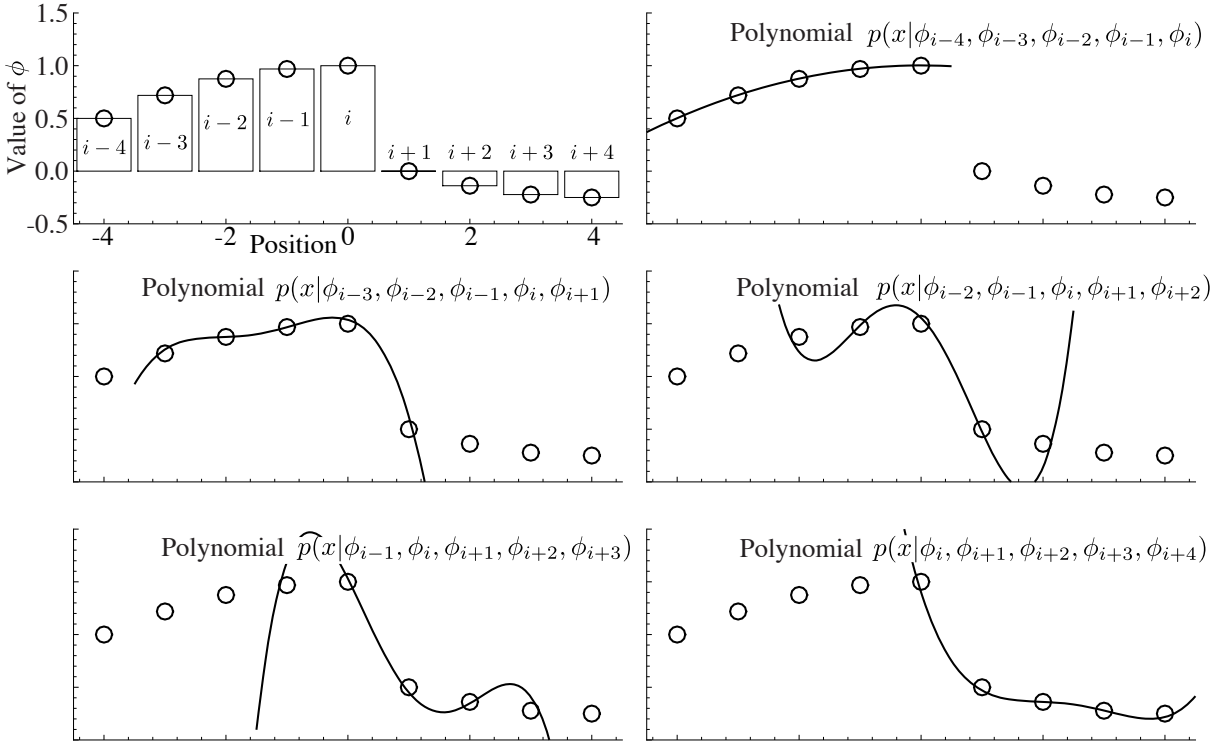

Figure 2.11: Possible polynomial template for fourth-order approximation of $\phi_{i+1/2}(t)$.

For the case presented in the above Figure, it is clear that the polynomial in the upper left corner is the best choice to evaluate the value of $\phi_{i+1/2}(t)$. In Liu *et al.* (1994), the authors present a procedure to determine the best interpolation template in the general case (illustrated in Figure 2.12). They further prove that this approach guarantees that the solution at the next time step will have minimum oscillation in the L_2–norm sense.

After careful consideration, one might notice that in regions where the solution is smooth, there is no real advantage to select one interpolation template over another. Furthermore, since there is no advantage in discarding templates, one should combine them to obtain a much higher-order interpolation polynomial.

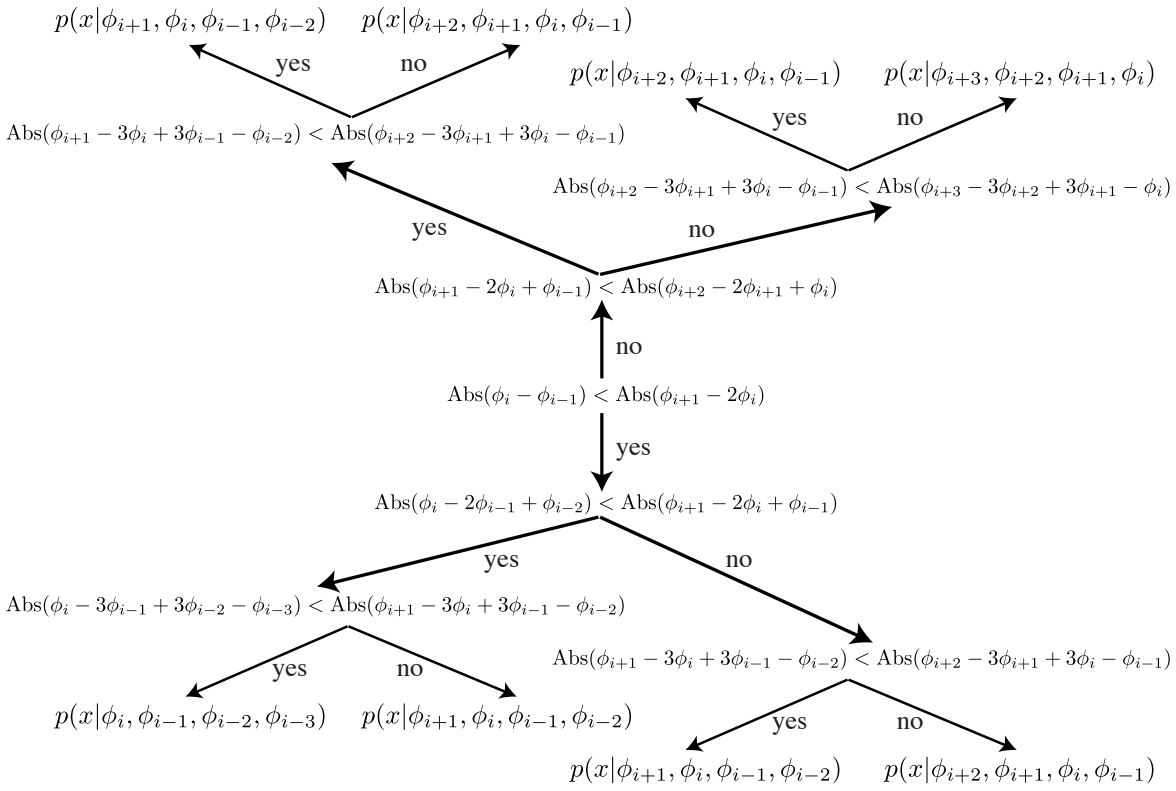

Figure 2.12: Flowchart for the selection procedure for the ENO interpolation template.

In Harten *et al.* (1987), the authors presented an approach in which interpolated values are given by a weighted average of all admissible templates (weighted ENO or WENO). The weights are functions of the norm of the derivatives such that in cases where sharp gradients are present the method reverts to the above ENO approach, and otherwise, to the highest order polynomial approximation possible. For the purpose of this work, the measure of smoothness for the polynomial template was taken from the work of Jiang & Shu (1996) and are given by

- Second-order polynomial:

$$IS_k = (\Phi_{k+1} - \Phi_k)^2.$$

- Third-order polynomial:

$$\begin{aligned} IS_k =& {}^1\!/_2 \left((\Phi_k - \Phi_{k-1})^2 + (\Phi_{k+1} - \Phi_k)^2 \right) \\ &+ (\Phi_{k+1} - 2\Phi_k + \Phi_{k-1})^2. \end{aligned}$$

- Fourth-order polynomial:

$$\begin{aligned} IS_k =& 1/3\left((\Phi_{k-1}-\Phi_{k-2})^2+(\Phi_k-\Phi_{k-1})^2+(\Phi_{k+1}-\Phi_k)^2\right) \\ &+1/2\left((\Phi_k-2\Phi_{k-1}+\Phi_{k-2})^2+(\Phi_{k+1}-2\Phi_k+\Phi_{k-1})^2\right) \\ &+(\Phi_{k+1}-3\Phi_k+3\Phi_{k-1}-\Phi_{k-2})^2. \end{aligned}$$

- Fifth-order polynomial:

$$\begin{aligned} IS_k =& 1/4\left((\Phi_{k-1}-\Phi_{k-2})^2+(\Phi_k-\Phi_{k-1})^2+(\Phi_{k+1}-\Phi_k)^2+(\Phi_{k+2}-\Phi_{k+1})^2\right) \\ &+1/3\left((\Phi_k-2\Phi_{k-1}+\Phi_{k-2})^2+(\Phi_{k+1}-2\Phi_k+\Phi_{k-1})^2+(\Phi_{k+2}-2\Phi_{k+1}+\Phi_k)^2\right) \\ &+1/2\left((\Phi_{k+1}-3\Phi_k+3\Phi_{k-1}-\Phi_{k-2})^2+(\Phi_{k+2}-3\Phi_{k+1}+3\Phi_k-\Phi_{k-1})^2\right) \\ &+(\Phi_{k+2}-4\Phi_{k+1}+6\Phi_k-4\Phi_{k-1}+\Phi_{k-2})^2. \end{aligned}$$

The admissible polynomial stencils are then be combined using the following weights (Jiang & Shu 1996):

$$\alpha_k = \frac{C_k^r}{(\epsilon + IS_k)^p}, \tag{2.66}$$

$$\omega_k = \frac{\alpha_k}{\alpha_1 + ... + \alpha_r}, \tag{2.67}$$

$$P(x) = \sum_{i=1}^{r} p_i(x)\omega_i, \tag{2.68}$$

where ϵ is a small number ($\epsilon = 10^{-8}$ in this work), p is some power greater than unity ($p = 3$ in this work), and r is the order of the polynomial stencil. The coefficients C_k^r are found in Table 2.1 and represent the optimal weights if all stencils are equally smooth.

	k=1	k=2	k=3	k=4	k=5
r=2	1/3	2/3	—	—	—
r=3	1/10	6/10	3/10	—	—
r=5	4/504	80/504	240/504	160/504	20/504

Table 2.1: Optimal weights for combination of polynomial stencils.

Additional methods have been devised to reduce the excessive dissipation of the WENO method at sharp interfaces. Methods such as the sub-cell resolution approach (Harten 1989) and artificial compression method (Yang 1990). For the purpose of this work, the artificial compression method (ACM) was implemented. Details for this approach can be found in the work of Yang (1990) and Jiang & Shu (1996). This method requires the input of a parameter α. In cases presented here, a value of $\alpha = 11$ was selected instead of the

$\alpha = 33$ proposed in Yang (1990). This value was obtained through trial and error and was found to be a reasonable compromise between compensating the WENO dissipation and preventing spurious oscillations.

2.6 Time marching algorithm

To ensure the smoothing properties of the WENO scheme, the discretized equations must be integrated using a TVD (total variation diminishing) time marching algorithm. A family of TVD Runge-Kutta scheme can be found in the work of Shu & Osher (1988) and Gottlieb & Shu (1998). In the present work, a third-order method was used.

$$\frac{d\mathbf{x}}{dt} = \mathbf{f}(\mathbf{x}, t) \tag{2.69}$$

$$\mathbf{x}^* = \mathbf{x}^n + \mathbf{f}(x^n, t)\Delta t \tag{2.70}$$

$$\mathbf{x}^{**} = \frac{3}{4}\mathbf{x}^n + \frac{1}{4}\mathbf{x}^* + \frac{1}{4}\mathbf{f}(\mathbf{x}^*, t)\Delta t \tag{2.71}$$

$$\mathbf{x}^{n+1} = \frac{1}{3}\mathbf{x}^n + \frac{2}{3}\mathbf{x}^{**} + \frac{2}{3}\mathbf{f}(\mathbf{x}^{**}, t)\Delta t \tag{2.72}$$

Although this time marching scheme is well suited for the integration of the discretized average mixture equations, it is not optimal for the disperse bubble phase. Very violent bubble activity occurs in lithotripsy so the time integration must be accurate to extremely small timescales. Since bubble collapse is of very short duration, it is much more efficient to use adaptive time stepping. The Rosenbrok adaptive time marching scheme performs well with stiff systems of equations and was used to compute the bubble activity in this work (see Press *et al.* 1996).

$$\frac{d\mathbf{x}}{dt} = \mathbf{f}(\mathbf{x}) \tag{2.73}$$

$$M \equiv \frac{d\mathbf{f}}{d\mathbf{x}} \tag{2.74}$$

$$\left(\frac{2}{\Delta t}\mathbf{I} - \mathbf{M}\right)\mathbf{x}^1 = \mathbf{f}(\mathbf{x}^n) \tag{2.75}$$

$$\left(\frac{2}{\Delta t}\mathbf{I} - \mathbf{M}\right)\mathbf{x}^2 = \mathbf{f}(\mathbf{x}^n + 2\mathbf{x}^1) - \frac{8}{\Delta t}\mathbf{x}^1 \tag{2.76}$$

$$\left(\frac{2}{\Delta t}\mathbf{I} - \mathbf{M}\right)\mathbf{x}^3 = \mathbf{f}\left(\mathbf{x}^n + \frac{48}{25}\mathbf{x}^1 + \frac{6}{25}\mathbf{x}^2\right) + \frac{371}{25\Delta t}\mathbf{x}^1 + \frac{12}{5\Delta t}\mathbf{x}^2 \tag{2.77}$$

$$\left(\frac{2}{\Delta t}\mathbf{I} - \mathbf{M}\right)\mathbf{x}^4 = \mathbf{f}\left(\mathbf{x}^n + \frac{48}{25}\mathbf{x}^1 + \frac{6}{25}\mathbf{x}^2\right) - \frac{112}{125\Delta t}\mathbf{x}^1 - \frac{54}{125\Delta t}\mathbf{x}^2 - \frac{2}{5\Delta t}\mathbf{x}^3 \tag{2.78}$$

$$\mathbf{x}^{n+1} = \mathbf{x}^n + \frac{19}{9}\mathbf{x}^1 + \frac{1}{2}\mathbf{x}^2 + \frac{25}{108}\mathbf{x}^3 + \frac{125}{108}\mathbf{x}^4 \tag{2.79}$$

$$\mathbf{error} = \frac{17}{54}\mathbf{x}^1 + \frac{7}{36}\mathbf{x}^2 + \frac{125}{108}\mathbf{x}^4 \tag{2.80}$$

Clearly, the time integration for the mixture is incompatible with that of the bubble phase. However,

two observations allows for the coupling of these two methods.

1. Even if the bubbles present within a control volume were to change rapidly, the associated pressure waves can only propagate at the speed of sound in the liquid. Therefore, waves caused by rapid fluctuations of the bubble radius do not have time to travel outside the control volume and are averaged out.

2. The timescale associated with bubble dynamics can be much shorter than that of the pressure field. However, much of the bubble behavior is dominated by the inertia of the surrounding liquid. Therefore, large amplitude bubble motion is rather insensitive to fluctuations in the far field pressure.

Following these two observations, we can conclude that for a sufficiently small timescale (smaller than that associated with the average mixture but larger than that associated with bubble dynamics), both phases can be integrated independently of one another over very short times. In other words, all fluctuations beyond this frequency will be averaged out over the control volume and are therefore neglected. This approach is beneficial in two ways: an appropriate time marching algorithm is used for each phase and the adaptive shrinking/enlarging of the time step for a bubble at a particular location is independent of other locations.

This segregated time integration method for the continuous and disperse phase is not as accurate as a combined approach where the same adaptive time step is used for the entire domain and all equations are integrated simultaneously. However, the computational cost associated with the combined approach is prohibitively large as the time step for the domain would shrink by several order of magnitude whenever a bubble in the domain would be near collapse. In terms of performance, it is therefore more advantageous to use a segregated time marching with a small time step in order to compensate for the lower accuracy of the method. The errors associated with the time-step segregation are quantified in the next section.

2.7 Spatial and temporal resolution study

To ensure that the results presented in this study are accurate, a grid resolution study was conducted. Two simulations were performed (**Run35c** and **Run35d**[2]) with identical parameters with the exception that the grid for **Run35d** has 150% of the number of grid points of **Run35c** in each direction. Furthermore, because of the greater spatial resolution, the time step for **Run35d** was half that of **Run35c**. Figures 2.13 and 2.14 compare the pressure field and bubble response for both simulations.

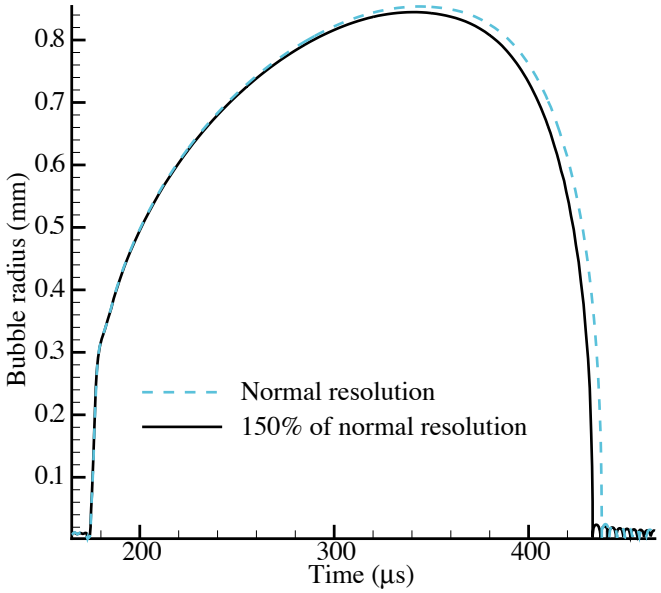

Figure 2.13: Comparison of the bubble response at the focus for high and normal resolution simulations.

In Figure 2.13 and 2.14, some differences between the high and normal resolution simulations can be noticed. The pressure amplitude of the shock wave is larger with the enhanced grid (see Figure 2.13). In addition, the time to collapse for a bubble at the focal point of the lithotripter is slightly larger for the regular grid (see Figure 2.14). However, in the present context, these differences are relatively minor and the general behavior of the bubble cloud is the same in both cases. Therefore, the spatial grid used was considered sufficient for the purpose of this study.

To ensure that the time step used is appropriate, comparisons were made for the same conditions of **Run35c** but for different time steps. Table 2.2 presents peak pressures, maximum bubble growth and time to collapse at the focus as a function of the time step used in the coupled integration. It is interesting to note in the following table that the peak pressures are relatively insensitive to the choice of time step. This

[2]A table of input parameter and results for various simulations can be found in Appendix A.

is to be expected since the accuracy of the propagation of the shock wave is determined mainly by the CFL number which is well below the stability requirement (CFL ≤ 1) for all cases. Because of the segregated time integration, the bubble dynamics can be affected by the choice of time step. As mentioned in the previous section, a larger time step may result in a loss of accuracy in the coupling between the two phases. Based on the results from Table 2.2, we can determine that the time steps used in the present work ($\Delta t = 0.020\ \mu s$ and $0.025\ \mu s$) are sufficiently small to ensure that the error introduced by the segregated time integration is much smaller than that introduced by other modeling aspects.

Δt (μs)	CFL	$P_{\max}$(MPa)	$P_{\min}$(MPa)	$R_{\max}$ (mm)	t_c (μs)
.0125	0.056	27.25	-13.44	0.770	225.9
.0170	0.076	27.47	-13.59	0.769	226.2
.0210	0.094	27.20	-13.64	0.770	226.0
.0250	0.112	27.38	-13.58	0.771	226.6
.0300	0.135	27.31	-13.45	0.777	228.0
.0350	0.157	27.43	-13.66	0.777	228.4
.0400	0.180	27.38	-13.44	0.781	229.4
.0450	0.202	27.40	-13.33	0.789	231.3
.0500	0.225	27.41	-13.29	0.795	232.7

Table 2.2: Impact of time step on pressure and bubble results.

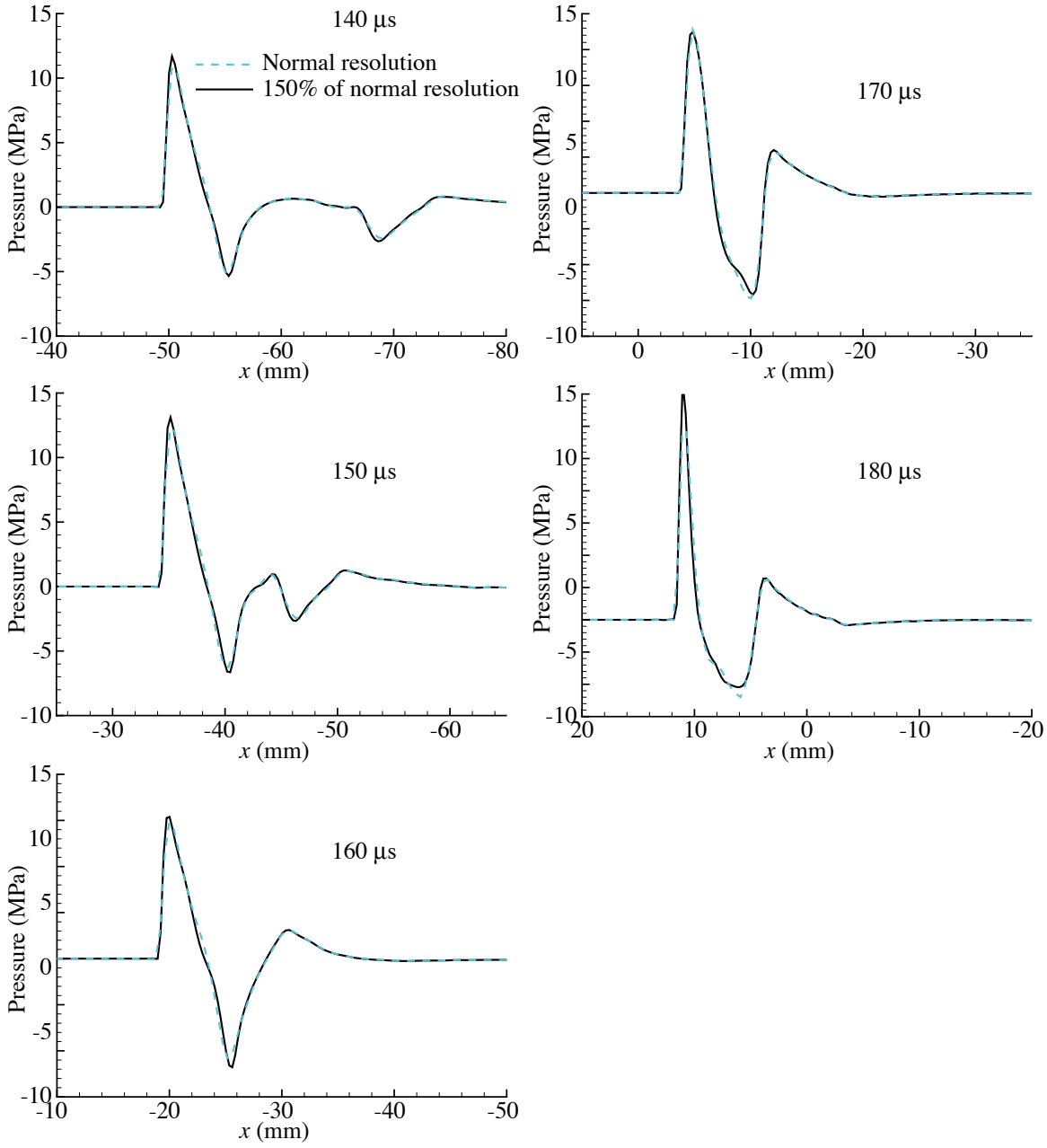

Figure 2.14: Pressure along side the axis of symmetry for high and normal resolution simulations.

Chapter 3

Results on shock wave focusing and cloud cavitation on SWL

3.1 Shock wave focusing in lithotripters

In the past, various approaches have been used to analyze shock wave focusing in lithotripsy. Cates & Sturtevant (1997) used shock propagation to compute the reflection of a planar shock wave from a parabolic reflector. Results for the incident and reflected wave based on a linear acoustic approach were presented in Hamilton (1993) and Averkiou & Cleveland (1999). In Averkiou & Cleveland (1999), the authors used nonlinear geometrical acoustics to propagate the initial wave inside the reflector, and a nonlinear KZK model (Zabolotskaya & Khokhlov 1969 and Kuznetsov 1970) for the wave propagation outside. This approach can represent the diffraction of the wave at the edge of the reflector. However, it is limited to waves with wavelength much smaller than the characteristic length of the domain. In the present work, we compare several approaches including the nonlinear Euler equations, the second order wave equation, and a geometrical acoustics approximation.

3.1.1 Closed ellipsoidal bowl

To demonstrate the differences between these approaches and their relevance to the modeling of lithotripsy, we can look at the propagation of a spherically expanding wave from the focal point of a closed ellipsoidal reflector (see Figure 3.1).

In addition, to ensure that grid resolution was not an issue in these tests, a long smooth initial pulse was used. Figure 3.2 compares the initial pulse used for this test to a typical initial condition used for lithotripsy simulation.

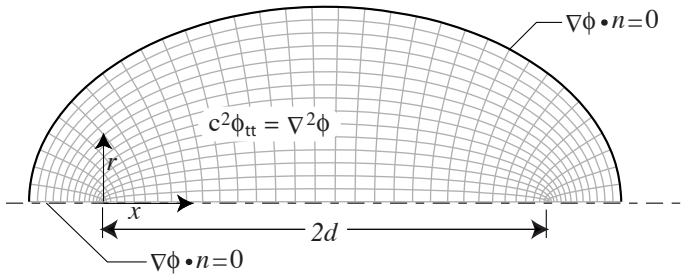

Figure 3.1: Geometry of closed ellipsoidal reflector bowl.

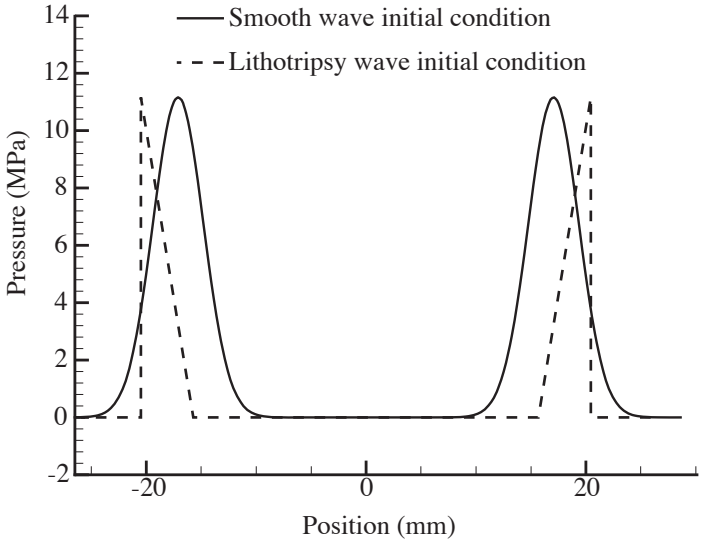

Figure 3.2: Comparison of smooth initial condition and the lithotripsy initial condition.

Figure 3.3 presents the results for the pressure along the axis of symmetry at different times. Geometrical acoustics are compared to linear wave propagation, linearized Euler and nonlinear Euler equations. The point F_1 indicates the first focal point of the reflector and the location of the spherical expanding wave. The linear wave propagation and linearized Euler curves are indistinguishable from each other in Figure 3.3. Since both model are equivalent, the only difference between them is due to small numerical errors in their respective implementation.

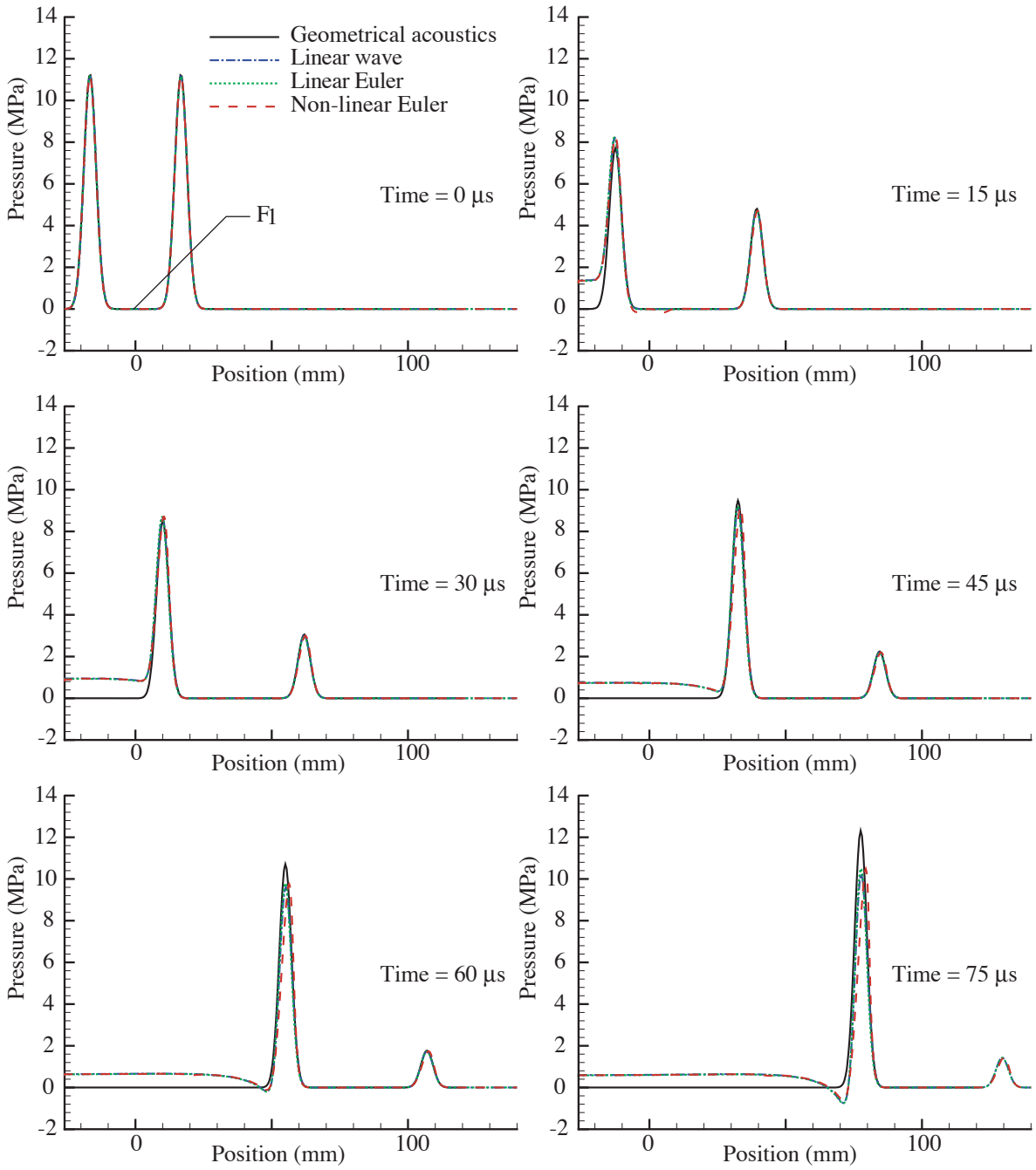

Figure 3.3: Pressure along the axis of symmetry for closed bowl using: geometrical acoustics, linear wave propagation, linear Euler equations and nonlinear Euler equations.

The results presented in Figure 3.3 illustrate several important features of a wave propagating inside an ellipsoidal bowl. These features are detailed in Figure 3.4:

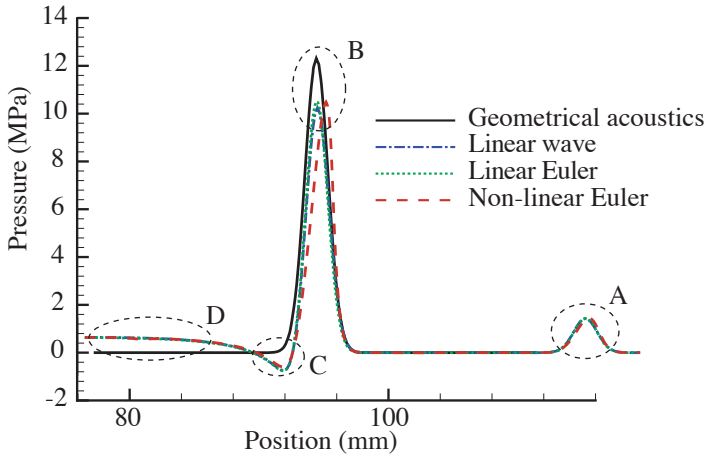

Figure 3.4: Comparison between methods: highlights of important features.

A The incident wave is well represented in all methods. Because of the dependence of speed of sound on pressure, the wave propagates slightly faster in the nonlinear Euler case.

B The amplitude of the reflected wave is too large in the geometrical acoustic approach. The amplitude and position of the reflected wave in the nonlinear model are slightly larger and propagates faster than linear cases, as expected (see A).

C An important feature not predicted by geometrical acoustics is the growth of a tensile region behind the reflected wave. This region of negative pressure is an important factor in the modeling of lithotripsy. As some of the numerical results will show, this zone can contribute to as much as half of the negative pressure measured at the focus (the other half is generated by an edge wave produced by the truncated reflector, as discussed in 1.1).

D Another important feature is the elevated pressure between the reflected wave and the bowl. The pressure in this region decreases as the reflected wave travels towards the second focus. Once again, this flow feature is not represented by the geometrical acoustics method. However, results from the linear wave propagation and nonlinear Euler equations agree very well with each other.

Both C and D are caused by the finite thickness of the incident wave. If the thickness of the pulse is reduced to a value much smaller than the length-scale associated with the reflector then the agreement with the geometrical acoustic method would be better. However, given the thickness of the lithotripsy incident wave, these effects cannot be neglected.

3.1.2 Edge wave and diffraction effects

As previously described in Section 1.1, the edge wave is caused by the diffraction of the wave (both incident and reflected) from the edge of the reflector bowl. In previous work such as Averkiou & Cleveland (1999), special modeling was required to represent diffraction. Acoustic models such as the KZK equation (Zabolotskaya & Khokhlov 1969, Kuznetsov 1970) can account for diffraction in a limited way. Other approaches such as Hamilton (1993) use Kirchhoff's integral (Born & Wolf 1980) to solve for the reflected and edge wave. In all previous works, special treatment was required to account for diffraction. Since Euler equations account for all acoustical effects, no special treatment was required in this work to produce the edge wave.

3.1.3 Pressure field in a lithotripter

The pressure field calculated using the numerical model presented here can be compared to experimental results and previously proposed theoretical models. In Figure 3.5, the maximum and minimum pressure recorded at the reflector's opening are compared to the pressure estimated using geometrical acoustics (see Appendix D for details on geometrical acoustics). The results are similar to those presented in Section 3.1.1. Since the initial pulse is now thinner, the agreement between the these results and the acoustical approach is somewhat better. However, this comparison still highlights the limitation of the acoustical approach. Our model predicts the development of a tensile region behind the reflected shock wave that cannot be represented using the geometrical acoustic approach. Similarly, the finite thickness of the pulse can be observed as a two and a half millimeter pressure rise region following the reflector.

Although the exact details of the edge wave are difficult to quantify, several observation can be made. Although its initial intensity is very small (order of 0.1 MPa), the strength of the edge wave increases as it propagates toward the axis of symmetry. Figure 3.6 shows a snap shot of the pressure field in the area of the edge of the reflector a few microseconds after the passage of the reflected wave.

The propagation of the edge wave is more complex than the propagation of the reflected wave itself. The reflected wave propagates in a relatively quiescent medium. Although the bubble field is perturbed by the incident wave, the time delay between its passage and that of the reflected wave is sufficient for the bubble activity to decay. However, bubbles in the wake of the reflected wave absorbed a considerable amount of energy and are growing rapidly (see Figure 3.7). The propagating edge wave distorts and, depending on the void fraction, develops a positive component (see Figure 3.8).

In the focal region, the reflected wave and edge wave are combined. In Figure 3.9, the pressure at the focal point of lithotripter is compared to experimental measurements in the Caltech-EHL. Numerical

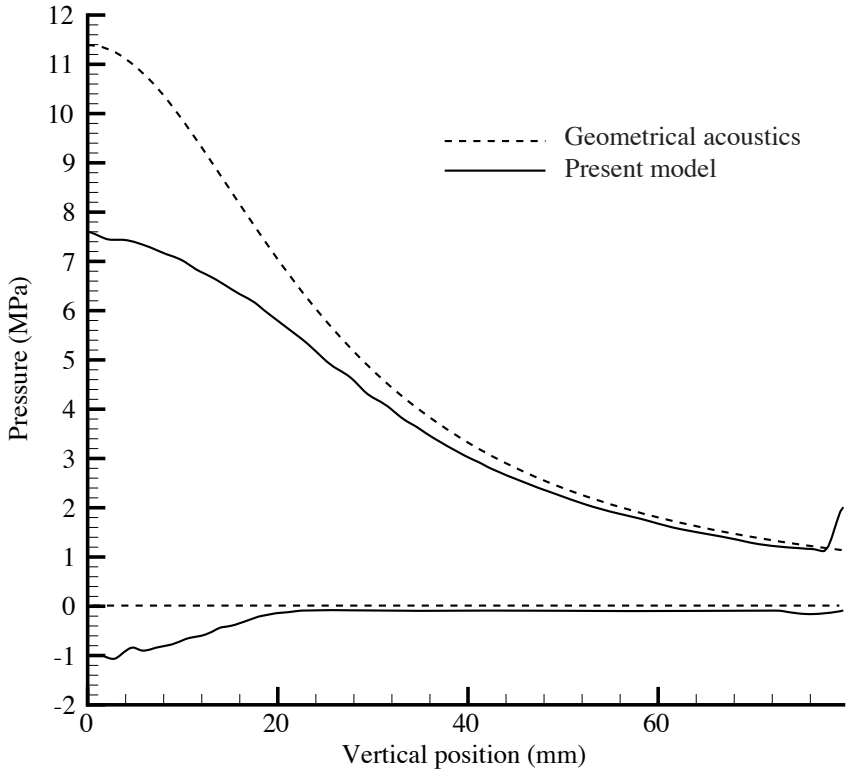

Figure 3.5: Minimum and maximum pressure at the mouth of the reflector for the present model and geometrical acoustics.

results compare well with the experimental observations in terms of the amplitude and duration of the tensile component. As for the discrepancy in the pressure rise of the shock wave, the sharp pressure jump is prevented by the dissipative properties of the WENO method used in the present numerical model. A grid with significantly higher resolution (10–100 times) would reduce this damping and allow for a sharp pressure rise at the shock wave. However this would increase the computing cost by a prohibitive factor (10^3–10^6 times).

The size of the focal region is often used as a means of comparing different lithotripter models. This area, often defined by the 6dB drop from the peak pressure, can provide some insight into the spatial distribution of the shock wave energy. The peak pressure amplitudes for a typical simulation case (**Run000**) is shown in Figure 3.10.

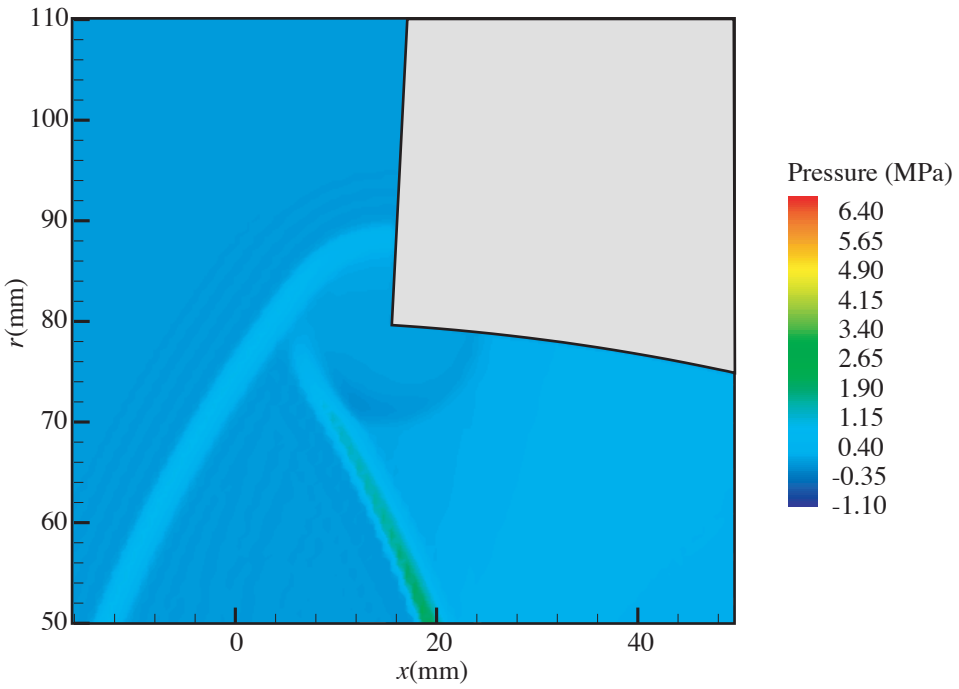

Figure 3.6: Pressure field near the edge of reflector: production of the edge wave.

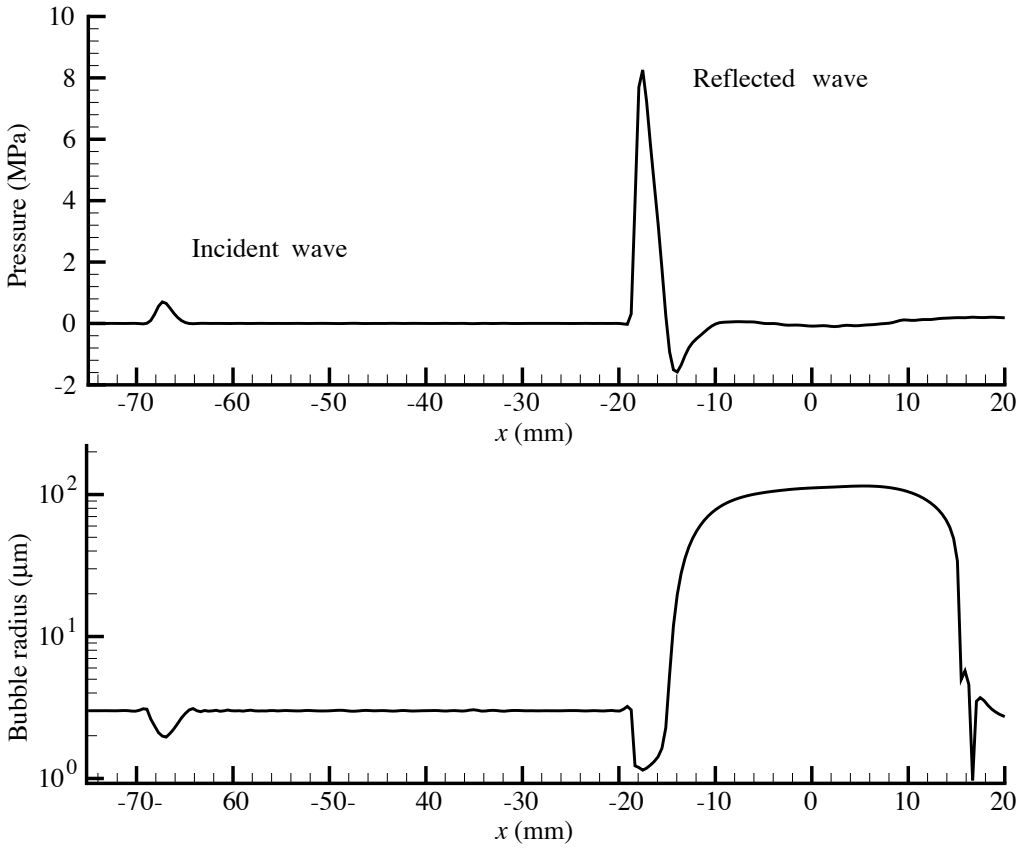

Figure 3.7: Snapshot of the pressure and bubble field along the axis of symmetry prior to the arrival of the edge wave.

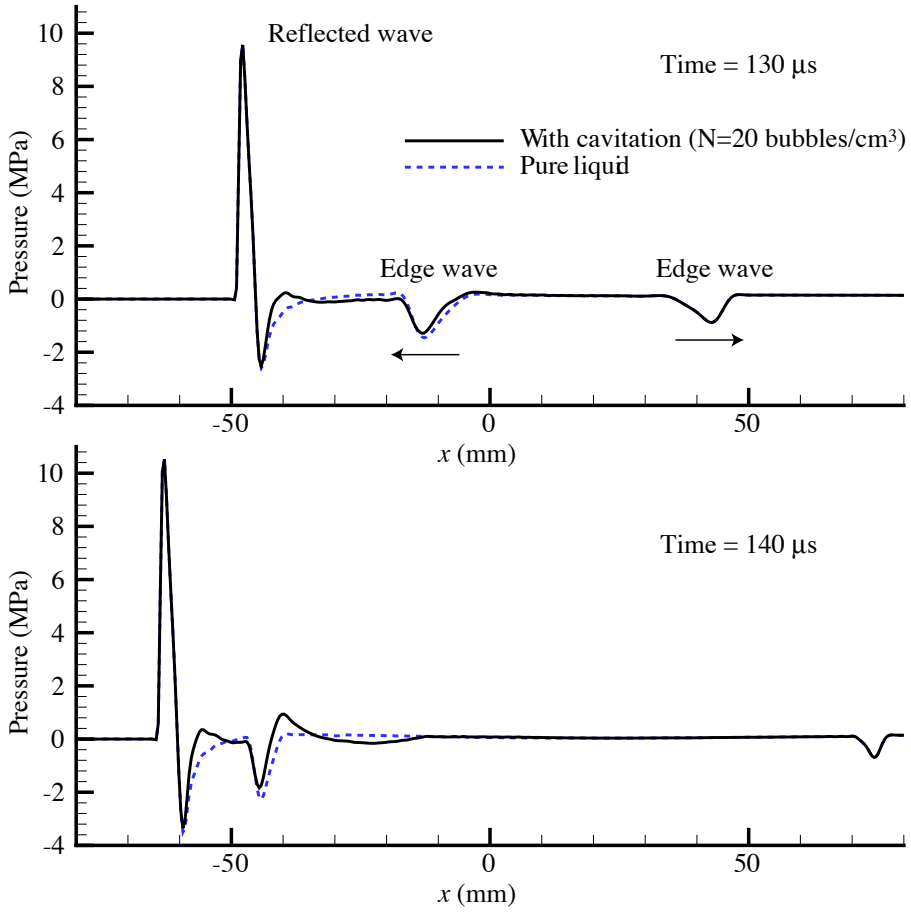

Figure 3.8: Impact of bubble activity on the propagation of the edge wave along the axis of symmetry.

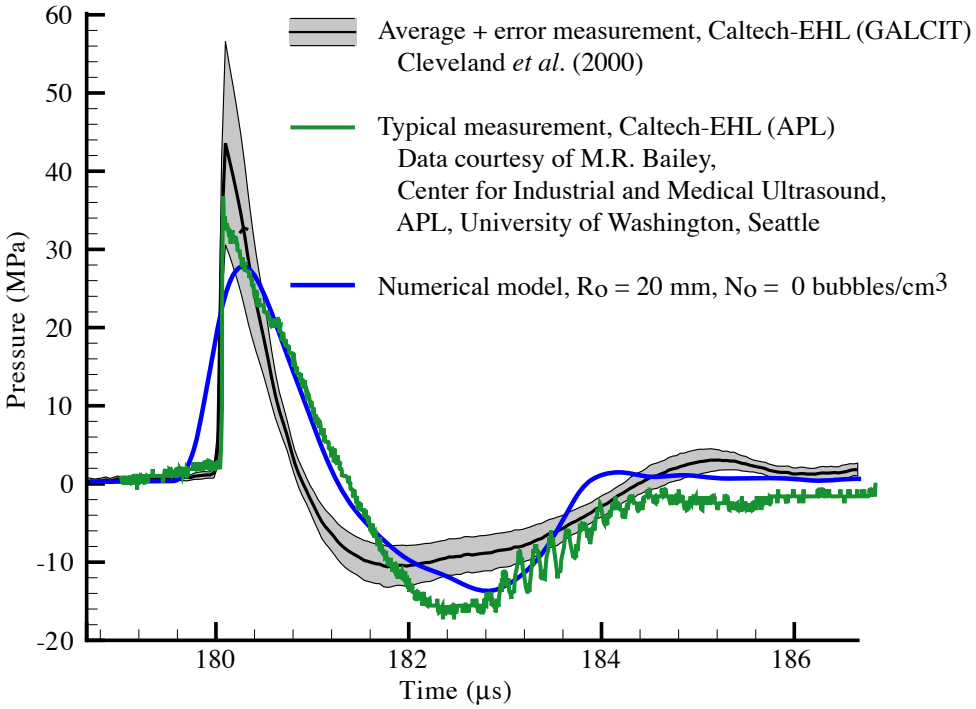

Figure 3.9: Pressure at the focal point of the lithotripter: comparison between experimental results and the present model for pure liquid.

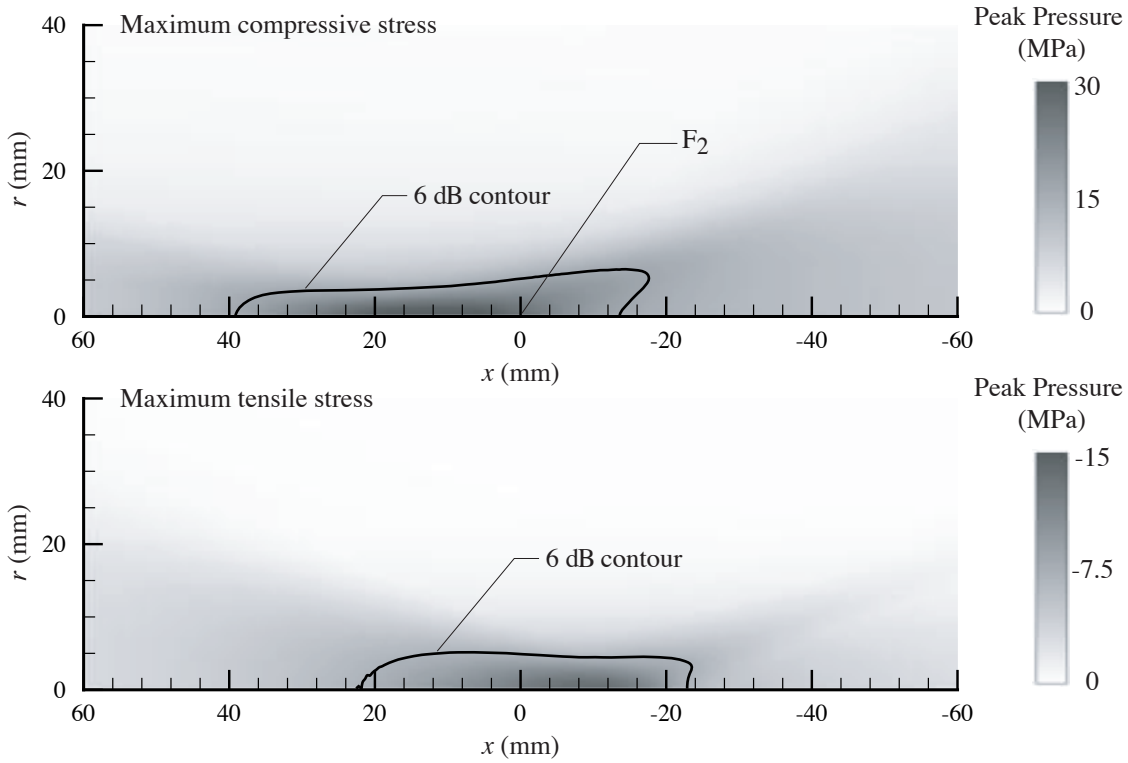

Figure 3.10: Distribution of maximum and minimum pressure in the lithotripter field using the present numerical model.

3.2 Bubble clouds in lithotripsy

3.2.1 Cloud cavitation in a free-field lithotripter

3.2.1.1 Exploration of the initial parameter space

In their work, Sokolov *et al.* (2001) reported that the bubble cloud in the focal area of a Caltech-EHL lithotripter can be approximated by a 1.5 cm wide by 10 cm long cylinder. Using the present numerical model, estimated size and shapes of bubble cloud were obtained and compared to the empirical observations. Changes to the initial bubble number density and equilibrium bubble size in the simulation can lead to visible difference in the shape and duration of the bubble cloud in the focal region. Figure 3.11 compares four different simulations to high-speed pictures from a typical experimental run. This comparison clearly shows that the duration of the bubble cloud (t_c) is a function of both the equilibrium radius and the bubble number density. As for the comparison with the experimental images, both similarities and discrepancies can be noted. At first glance, it appears that the experimental bubble cloud (dark spots on the photographs) is wider than its numerical counterpart. However, since void fraction contours are presented in the numerical results (proportional to the cube of the bubble radius), the comparison with experiments should only be made with the larger bubbles. Consequently, if we disregard the smaller bubble on the outer edge of the cloud, the agreement between the two results is better. Furthermore, the numerical model represents an ensemble average of possible bubble configuration and should therefore be compared to the average of many experiments.

Another point of interest is the discrepancy in the location of the center of the bubble cloud between the experiment and the numerical calculations. It is difficult to ascertain the cause of this discrepancy. As seen in Figure 3.12, the experimental bubble cloud does not appear to be centered about the focus of the lithotripter as expected. It should be noted that this pre-focal location of the bubble cloud appears to be consistent with the results reported by Sokolov *et al.* (2002) that shows improved stone comminution for stones placed two centimeters in front of the focal point.

The discrepancy between the observed and predicted location of the bubble cloud could be caused by an error in the initial shape of shock wave. As shown in Staudenraus & Eisenmenger (1993), PVDF membrane hydrophone can under-predict the duration of the negative (tensile) component of the pressure at the focal point. Crum (2003) has suggested that the actual tensile component could be as much as twice the duration of the measured one. Since the width of the initial spherical pulse used in this work was determined by matching the duration and intensity of the focal pressure measured using PVDF hydrophone (see Figure

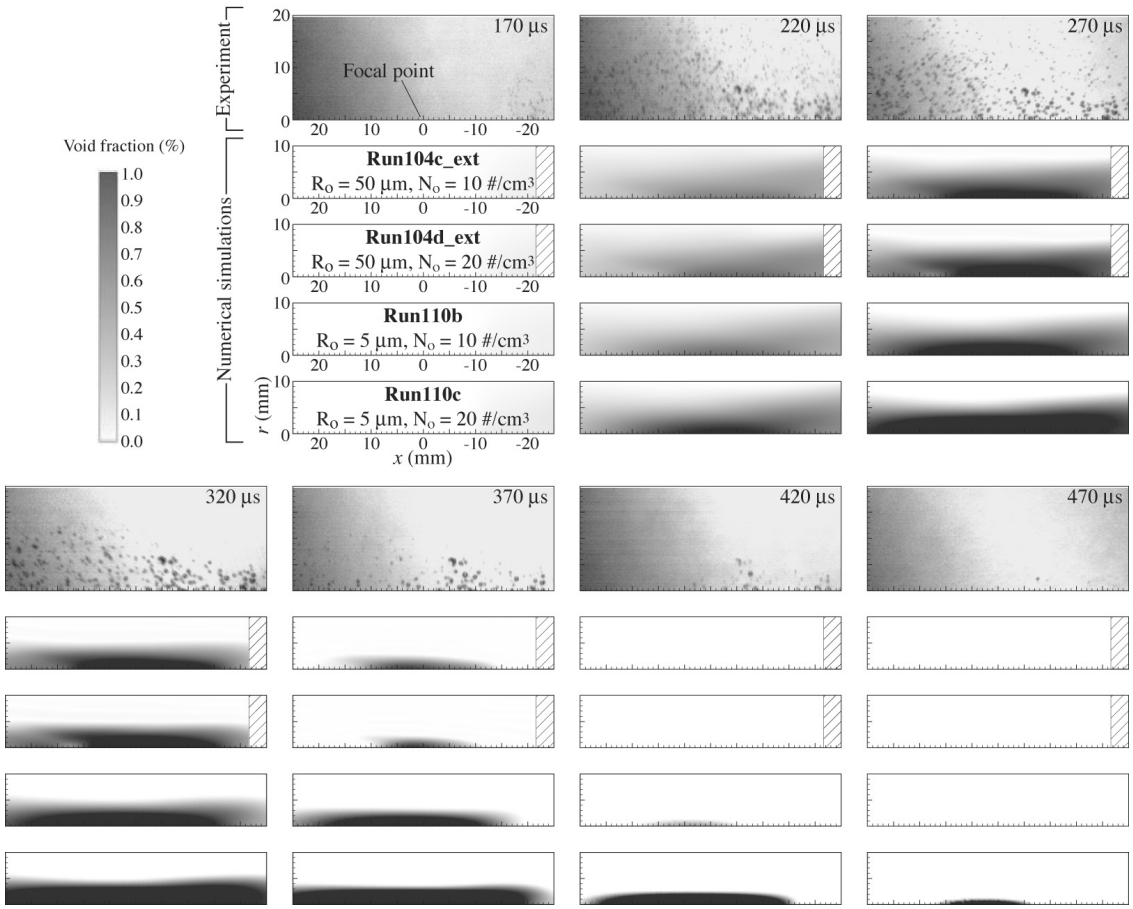

Figure 3.11: Comparison of bubble cloud between numerical simulations with various parameters and experiments. High-speed images are a courtesy of Dahlia L. Sokolov, Center for Industrial and Medical Ultrasound, Applied Physics Lab, University of Washington, Seattle.

3.9), a wider initial pulse may be required. A wider initial pulse would increase the tensile component generated behind the reflected wave due to the curvature mismatch between the wave and the reflector (see Section 3.1.1). This would also result in increased bubble activity in the wake of the reflected wave. Consequently, the edge wave generated as the reflected wave leaves the ellipsoidal bowl would travel slower in the higher void fraction mixture. Therefore, the location of the maximum tensile stress would be located before (prefocally) the current location and predict the center of the bubble cloud closer to the observed value.

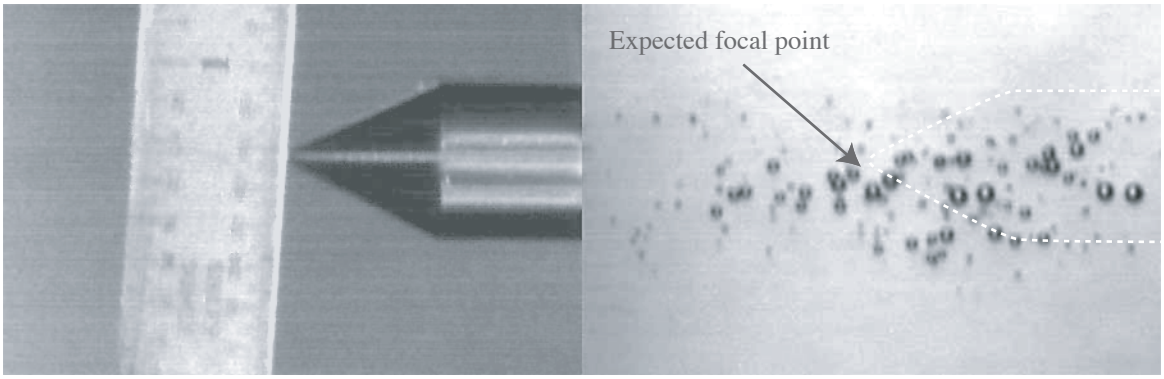

Figure 3.12: Expected position of the focal point for the experimental lithotripter. Courtesy of Dahlia L. Sokolov, Center for Industrial and Medical Ultrasound, Applied Physics Lab, University of Washington, Seattle.

3.2.1.2 Time to collapse

The measured time to collapse for the Caltech-EHL has been reported to be in the vicinity of 320 μs.[1] This value provided a guide for the calibration of some of the simulation parameters. As mentioned in Appendix F, the equilibrium bubble radius is typically estimated in the literature using the measured value for the time to collapse from PCD and a numerical model for the bubble dynamics. However, as seen in Figure 3.13, the relationship between the equilibrium radius and the time to collapse is complicated by a dependency on the bubble number density.

By conducting series of simulations with different initial bubble conditions, parameters which yielded the appropriate time to collapse were identified. Cases **Run105a** (t_c = 333 μs) and **Run105d** (t_c = 315 μs) compared well with experimental images not only in terms of the lifetime but also in terms of the dimensions of the bubble cloud (see Figure 3.14).

3.2.1.3 Maximum bubble size

In their description of the bubble field, Sokolov *et al.* (2001) reported a peak bubble radius in the focal area to be approximately 0.5 mm. It should be noted that the maximum bubble size does fluctuate from experiment to experiment. For example, the maximum bubble radius in the high-speed picture used in Figures 3.11 and 3.14 is approximately 0.75 mm. The numerical model can predict a wide range of maximum bubble radius (from 0.52 mm to 0.91 mm) depending on the initial simulation parameters. However, selecting appropriate bubble equilibrium radii and number density to yield matching values of $R_{\max}$ and t_c for bubbles in the

[1] In the work of Sokolov *et al.* (2001), the authors reported a value of t_c of 340 ± 31 μs using a passive cavitation detector (PCD) and a value of 300 ± 20 μs based on high-speed photography.

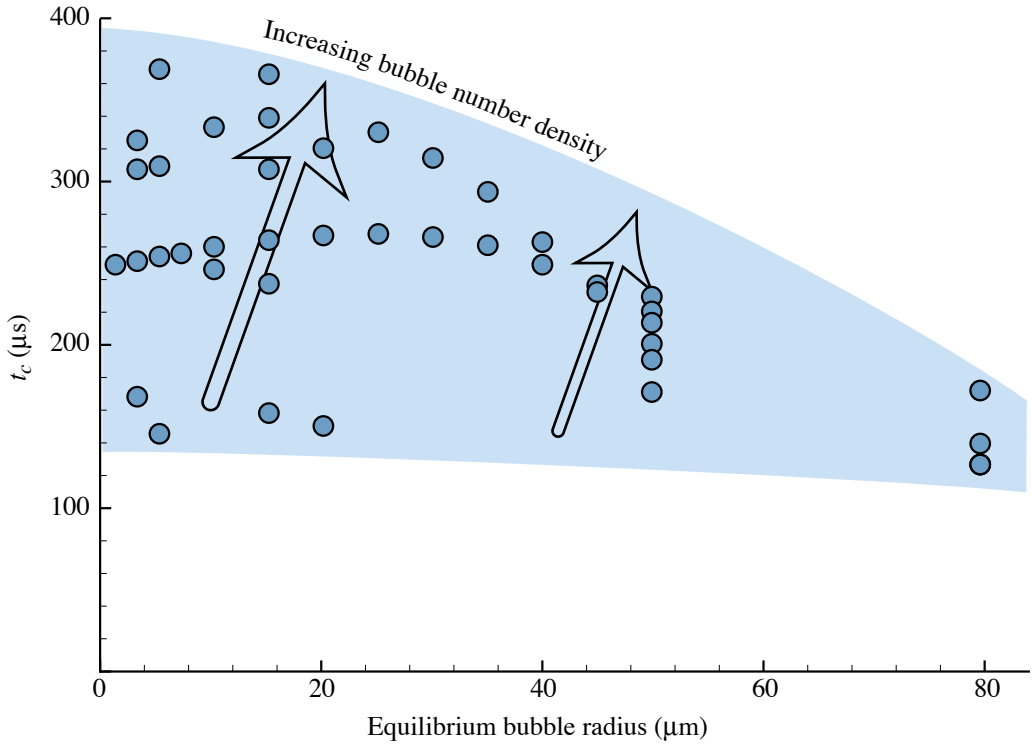

Figure 3.13: Time to collapse for the bubble cloud predicted by the present numerical model as a function of the initial bubble radius. Data shown was taken from table A.3 in Appendix A.

focal region proved difficult. Figure 3.15 shows the maximum radius and time to collapse for a variety of simulation parameters. The Rayleigh collapse relationship between $R_{\max}$ and t_c is shown by a straight line while the grey rectangle represents the range of empirical observations. Using the present numerical model, we were unable to exactly match values corresponding to what has been presented in the literature. However, the first order coupling between the bubble field and pressure field used here is clearly present a better approximation than any decoupled approach which, as mentioned previously in Section 1.3.2, would fall very close to the Rayleigh collapse line.

3.2.1.4 Selection of appropriate simulation parameters and relevant results

Based on the comparisons made in the previous sections, a few combinations of simulation parameters (density and size of bubble nuclei and intensity of initial spherical shock wave) provided results closest to empirical observations. As seen in Table A.3 in Appendix A, simulations using a bubble number density in the range of 10 to 20 bubbles/cm^3 and an equilibrium bubble radius in the range of 3 to 35 μm provided the closest match to empirical observations made in Sokolov *et al.* (2001). These values for the bubble

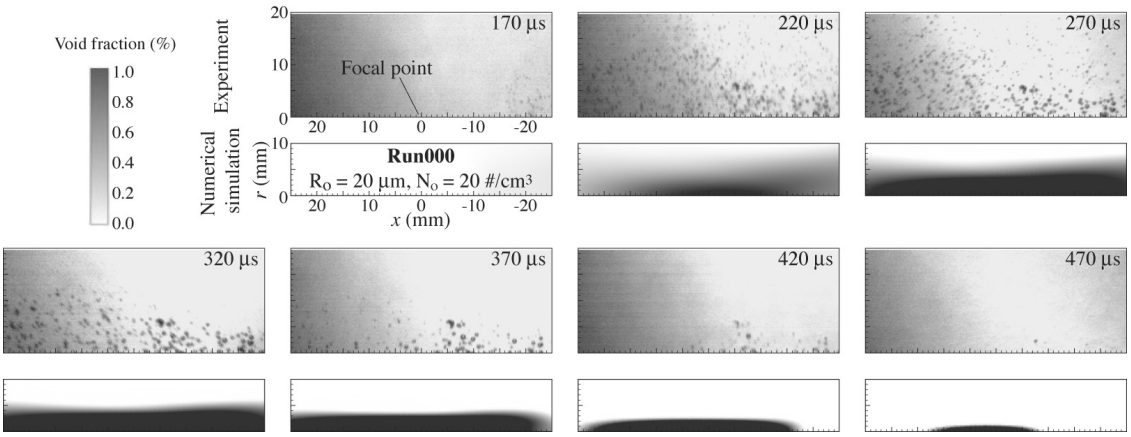

Figure 3.14: Comparison of bubble cloud between experiments and numerical simulations with similar time to collapse. High-speed images are a courtesy of Dahlia L. Sokolov, Center for Industrial and Medical Ultrasound, Applied Physics Lab, University of Washington, Seattle.

density and initial radius are close to the previously reported estimates of approximately 3 to 30 μm and 70 bubbles/cm^3 (Sokolov *et al.* 2001). A more detail discussion on estimated values can be found in Appendix F. Results for a typical simulation with this range (**Run000**) are presented in Figures 3.16 to 3.18.

As discussed previously, the bubble cloud observed in the experimental Caltech-EHL is centered at some distance before the focal point (from 1 to 2 cm). This is contrary to what is generally observed in the present numerical results. As seen in Figure 3.16, the bubble cloud is approximately centered about the focus. With regards to the size and shape of the bubble cloud, the numerical results compare well with the expected size if we define the edge of the cloud by the 0.2% void fraction contour level (see Figure 3.16). Although this value may seem rather small, it should be kept in mind that it represents bubbles of approximately 0.3 mm which is 35% of the maximum bubble size for this simulation.

The pressure at the focus for **Run000** is slightly different from the trace shown in Figure 3.9 for the pure liquid case. As mentioned previously, the presence of the growing bubble field in the wake of the reflected wave impacts the propagation of the edge wave (see Figure 3.8). As a result, a trailing positive pressure peak can be seen at the focal point (see Figure 3.17).

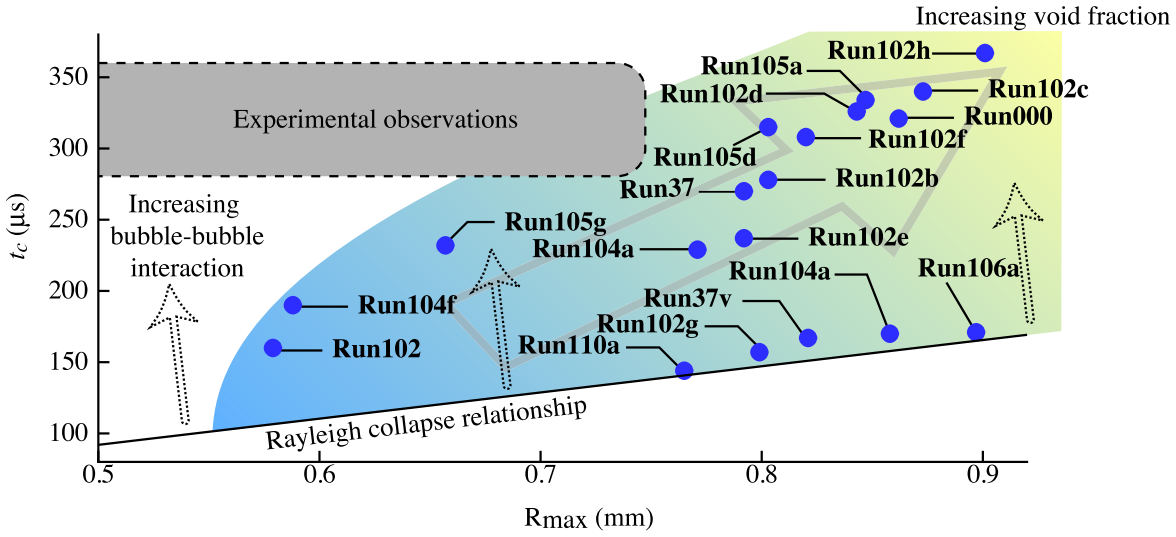

Figure 3.15: Relationship between $R_{\max}$ and t_c for various simulations compared to experimental observations. Data shown was taken from Table A.3 in Appendix A.

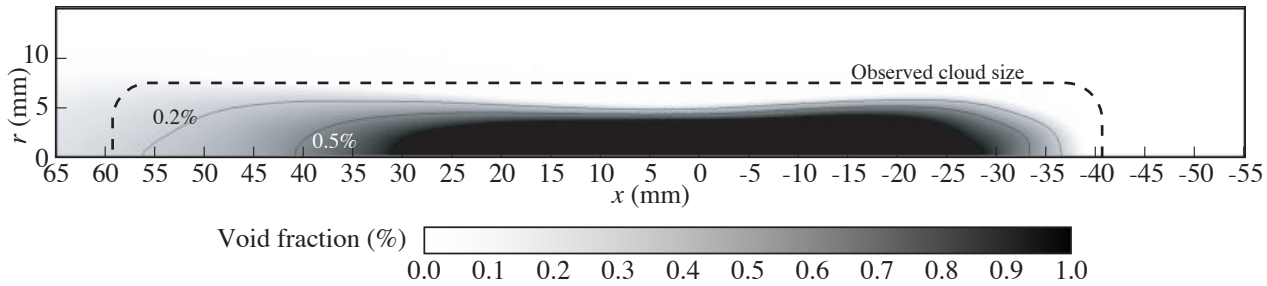

Figure 3.16: Comparison of the bubble cloud for **Run000** (at time 320 μs) and a typical size of bubble cloud seen in experiments (dashed line).

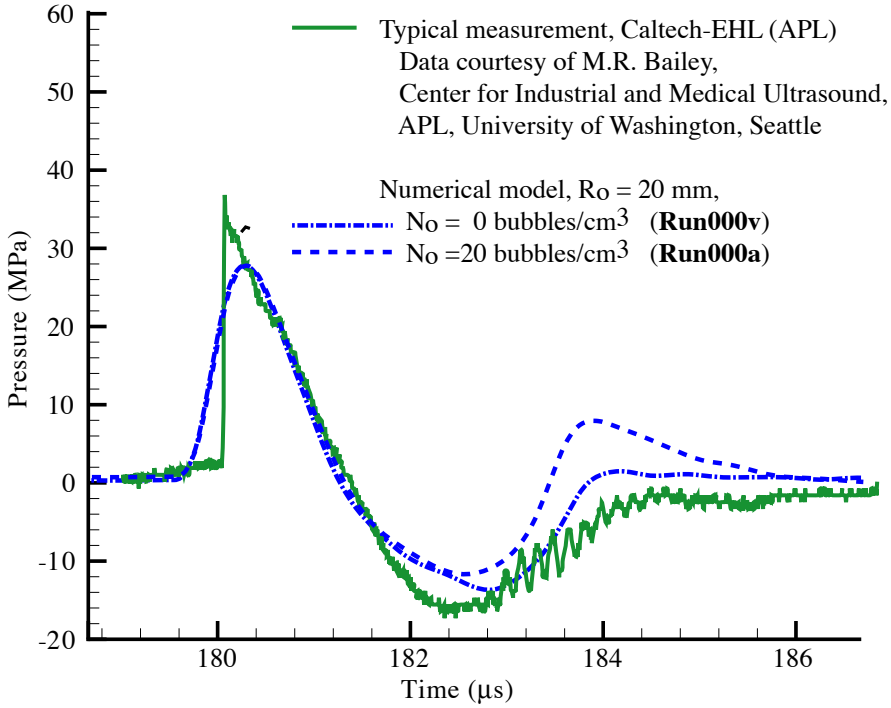

Figure 3.17: Impact of cavitation on the pressure at the focal point of a lithotripter.

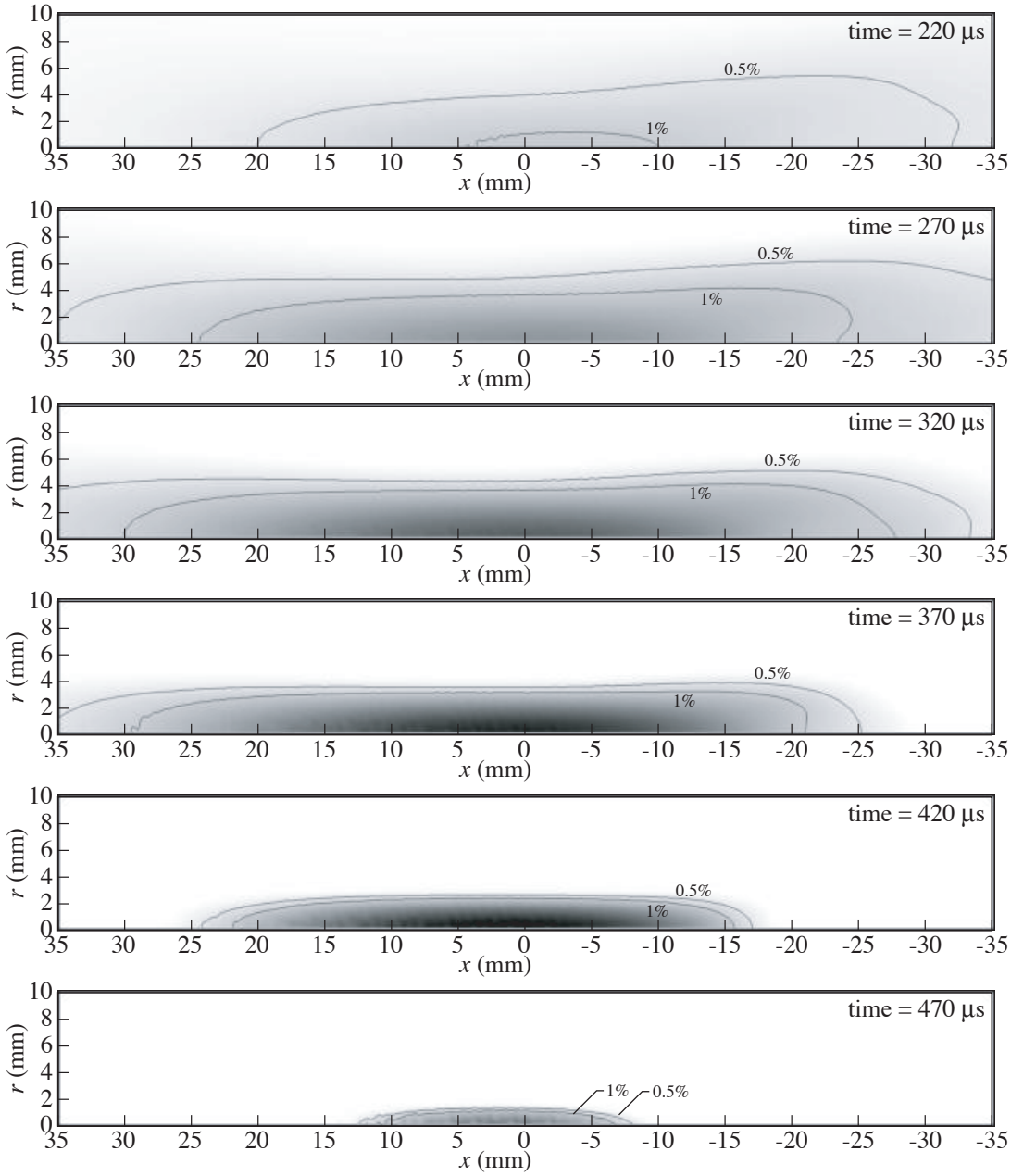

Figure 3.18: Bubble cloud evolution for **Run000**. Color contour levels range from 0–5% void fraction. Void fraction contour .5% and 1% are shown as black line.

3.2.2 Pressure waves in collapsing cloud

As mentioned in Section 1.3.2, interactions within a cloud of bubbles can have a significant impact on the response of individual bubbles. For cases with large bubble number densities, pressure waves are produced during the collapse of the bubble cloud. Figure 3.19 shows a simplified illustration of the features of the collapsing bubble cloud.

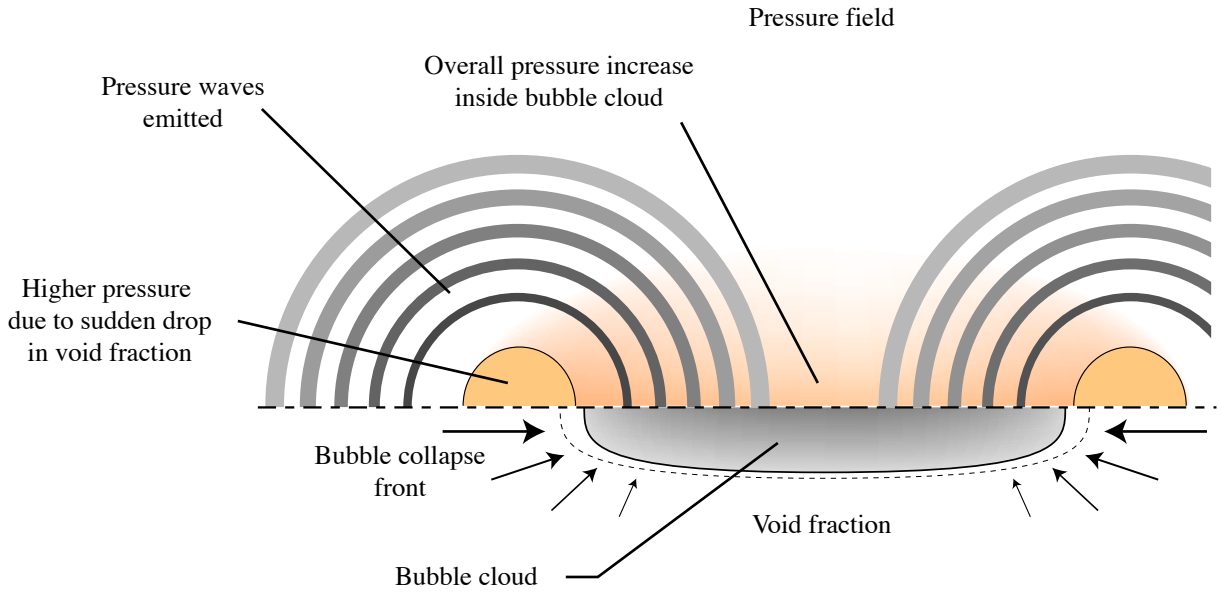

Figure 3.19: Illustration of the pressure field during collapse of the bubble cloud.

Figure 3.20 presents the numerical results for the void fraction and pressure field for a collapsing bubble cloud. Although some of the features are complex, the structures illustrated in Figure 3.19 can be identified. This effect is not due to the pressure wave emitted by collapsing bubbles but rather by changes in the bulk density of the mixture. As the bubble collapse front advances towards the center of the cloud, the liquid must rush in to fill the volume which was originally occupied by the collapsed bubbles. As a consequence of this flow field, the pressure increases in front of the receding edge of the bubble cloud. This effect is the reverse of the interaction which allow bubbles at the core of the cloud to have a longer time to collapse (see Section 1.3.2).

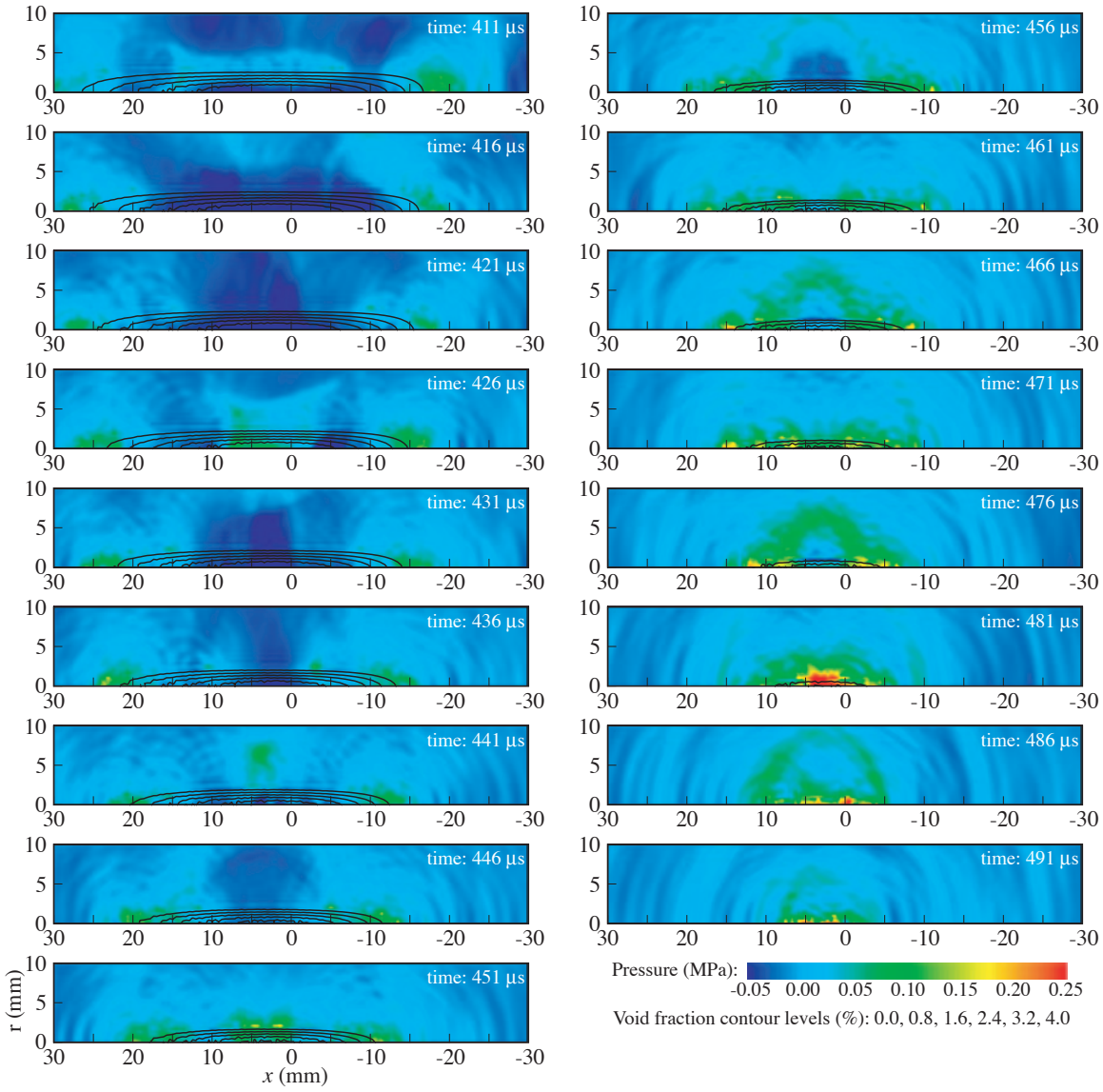

Figure 3.20: Pressure field (color contours) and void fraction (black lines) in the focal region during collapse of the bubble cloud. Data from **Run000**.

3.2.3 Energy focused by bubbles

The energy stored by a cavitating bubble as it initially interacts with the pressure field is ultimately released during its violent collapse. Part of this energy will be released in the form of an expanding spherical pressure wave (which can be measured by a passive cavitation detector (PCD)). In the case where the collapse is asymmetric, part of the stored energy will be released in the form of a micro-jet which, if close to a solid

object such as a kidney stone, can cause pitting of the surface. The details of the amount of energy release in jetting versus pressure wave or heat generation are complex and have not yet been modeled in this work. However, it is clear that the stone comminution capability of a cavitating bubble is a function of the work done on it by the mean pressure field.

In post-processing the simulation data, the energy released by a bubble was computed using a slightly different bubble model. We consider the Herring model (Herring 1941):

$$\left[1-2\frac{\dot{R}}{c}\right]R\ddot{R}+\frac{3}{2}\left[1-\frac{4}{3}\frac{\dot{R}}{c}\right]\dot{R}^2=\frac{p_B-p_\infty(t)}{\rho}+\frac{R}{c}\frac{d}{dt}\left(\frac{p_B-p_\infty(t)}{\rho}\right), \tag{3.1}$$

which is nearly identical to the Gilmore model discussed earlier and has the advantage that certain terms can be integrated analytically. Rewriting the above equation:

$$\frac{1}{R^2}\frac{1}{2}\frac{d}{dR}\left(R^3\dot{R}^2\right)+\frac{1}{R^2}\frac{3}{2c}\frac{d}{dR}\left(R^3\dot{R}^3\right)=\frac{p_B-p_\infty(t)}{\rho}+\frac{R}{c}\frac{d}{dt}\left(\frac{p_B-p_\infty(t)}{\rho}\right). \tag{3.2}$$

Integrating the equation once:

$$\frac{1}{2}\left(1+3\frac{\dot{R}}{c}\right)R^3\dot{R}^2=\int\frac{p_B}{\rho}R^2dR+\int\frac{R^3\dot{R}}{\rho c}\frac{dp_B}{dR}dR-\frac{1}{\rho}\int\left[p_\infty+\frac{R}{c}\frac{dp_\infty}{dt}\right]R^2dR+\text{constant}. \tag{3.3}$$

The $\dot{R}/c$ dependence on the left hand side of the above equation was found to be negligible in cases relevant to this work. Similarly, the second term on the right hand side was also found to be negligible. The above equation can therefore be simplified down to

$$\frac{1}{2}R^3\dot{R}^2\approx\int_{R_o}^{R}\frac{p_B}{\rho}R^2dR-\frac{1}{\rho}\int_{R_o}^{R}\left[p_\infty+\frac{R}{c}\frac{dp_\infty}{dt}\right]R^2dR, \tag{3.4}$$

Kinetic energy: $\frac{1}{2}\rho R^3\dot{R}^2$,

Bubble potential energy: $\left[\int p_BR^2dR\right]_R$,

Initial bubble energy: $\left[\int p_BR^2dR\right]_{R_o}$,

Work done by liquid: $\int_{R_o}^{R}\left[p_\infty+\frac{R}{c}\frac{dp_\infty}{dt}\right]R^2dR$.

To analyze the energy absorbed by a bubble during collapse in the context of lithotripsy, we compared

a simulation with and without bubble cloud cavitation. The parameters for the two simulations were the same except for the bubble number density. In the 'no bubble cloud' case, the bubble number density was set to zero which decouples the pressure field from the bubble dynamics. The bubble number density for the 'bubble cloud' simulation was set to 10 bubble/cm^3. As a first comparison, Figure 3.21 shows the pressure at the focus for both cases. It is interesting to note that apart from the pressure rise in the tail of the pulse, the two waves are very similar.

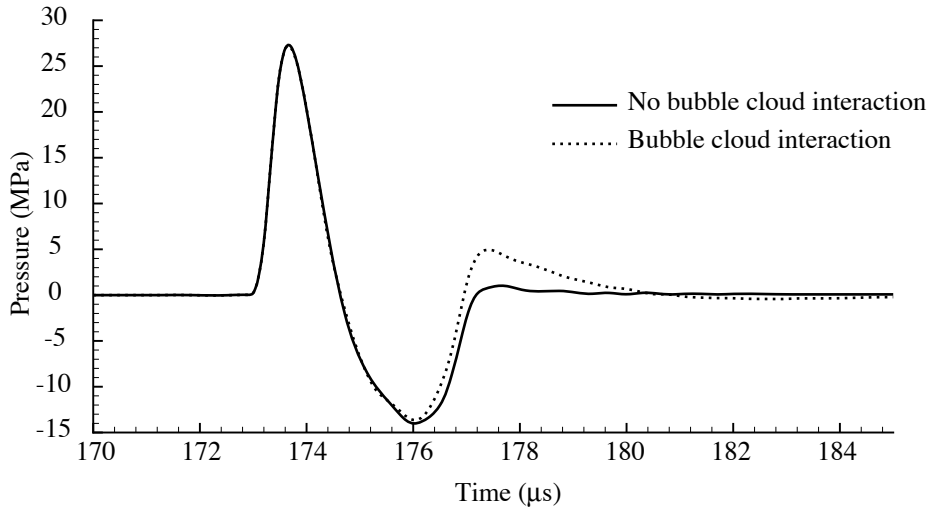

Figure 3.21: Impact of bubble cloud on pressure at focus. Data from **Run000** and **Run000v**.

Given the similarity between the above pressure waves, it would be expected that the resulting bubble dynamics should be also similar. However, the computer model predicts significantly different bubble behavior for these cases. Figure 3.22 compares the bubble history, small-scale pressure fluctuation and bubble energy at the focal point for coupled and uncoupled cases. As seen in the upper part of Figure 3.22, the bubble growth and collapse for the bubble cloud case is far from symmetric. Due to the presence of the bubble cloud, the bubble does not absorb as much energy from the passage of the shock wave and exhibits a slower growth rate than in the case without the bubble cloud because of the trailing positive peak in the pressure (Figure 3.21). Furthermore, the expansion of the bubbles within the cloud displaces liquid outward and decreases the mixture pressure inside. Consequently, bubbles can grow for a longer duration and the maximum radius is achieved much later than in the noninteracting case. It is also important to note that based on the history of the bubble radius, bubble collapse inside the cloud appears more violent.

From the bottom plot of Figure 3.22, it is interesting to note that the energy at the peak bubble radius $R_{\max}$, is approximately the same, which leads to the conclusion that the exact details of the lithotripter

waveform are not as important as the maximum bubble size. Without the pressure rise due to interactions within the cloud, all waveforms producing similar peak bubble growth would be equivalent (assuming similar size bubble cloud). A second, perhaps even more important conclusion from these results, is that the collapsing bubble cloud provides nearly half the work done by the fluid on a bubble. This is particularly surprising since the pressure amplitudes related to the cloud collapse are two orders of magnitude smaller than that of the lithotripter shock wave. However, the work done (PdV work) by the fluid is very large because the bubble radius changes several orders of magnitude. In addition, since cloud interactions are a direct function of the void fraction, the energy released increases steadily with the maximum void fraction (see Figure 3.23),

As seen in Figures 3.22 and 3.23, a bubble at the focal point can absorb and release up to 50 μJ. Considering that a bubble cloud can contain up to several hundred large bubbles, the amount of energy contained within the cloud can be estimated to be of the order of 1-10 mJ. This value appears relatively small compared to the energy contained in the initial spherical pulse which is of the order of 100 mJ. However, since the shock wave propagates relatively unhindered past the bubble cloud, only a small portion of the wave energy is expected to be retained by the cloud.

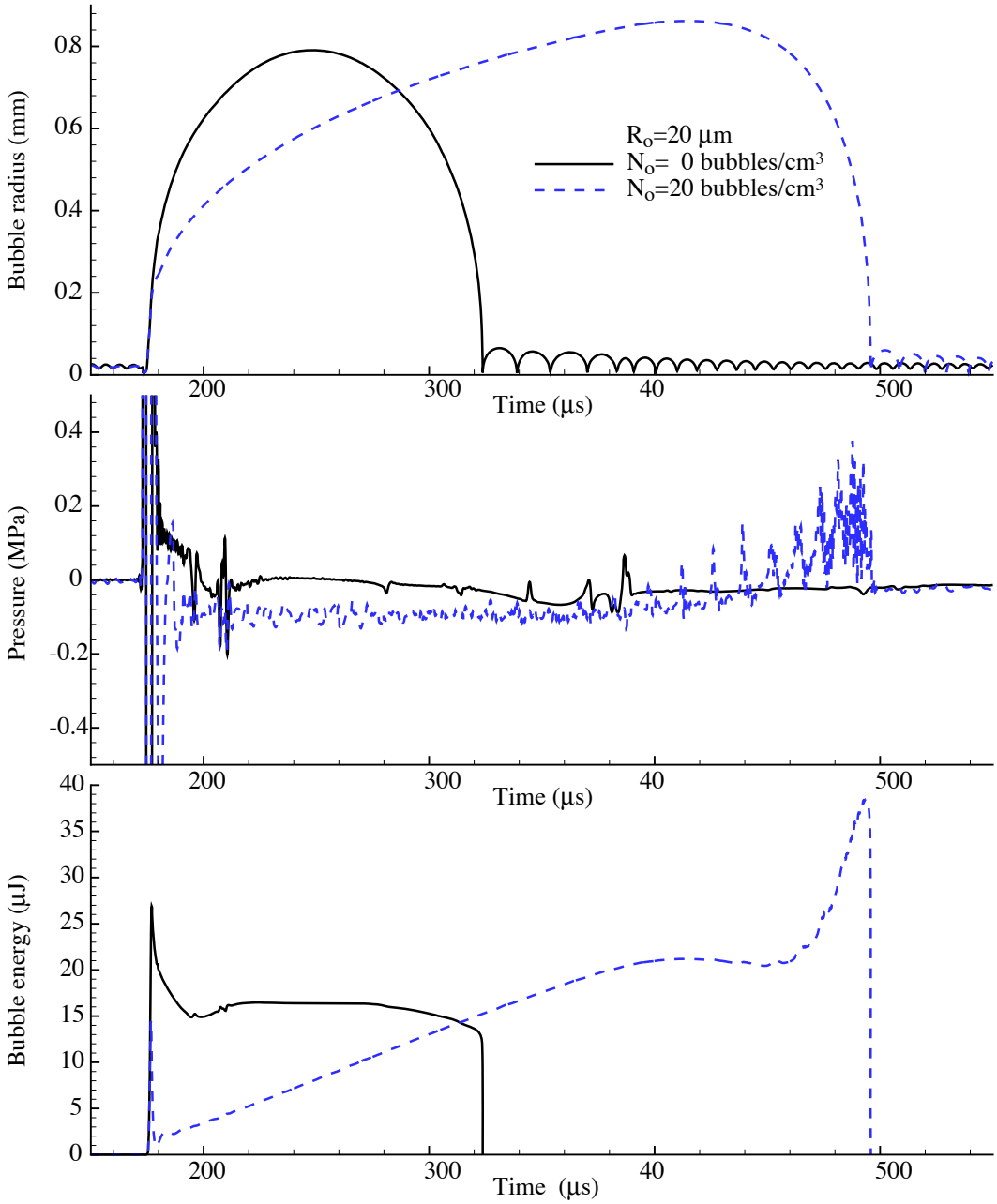

Figure 3.22: Impact of bubble cloud on bubble radius, small-scale pressure and bubble energy at focus. Data from **Run000** and **Run000v**.

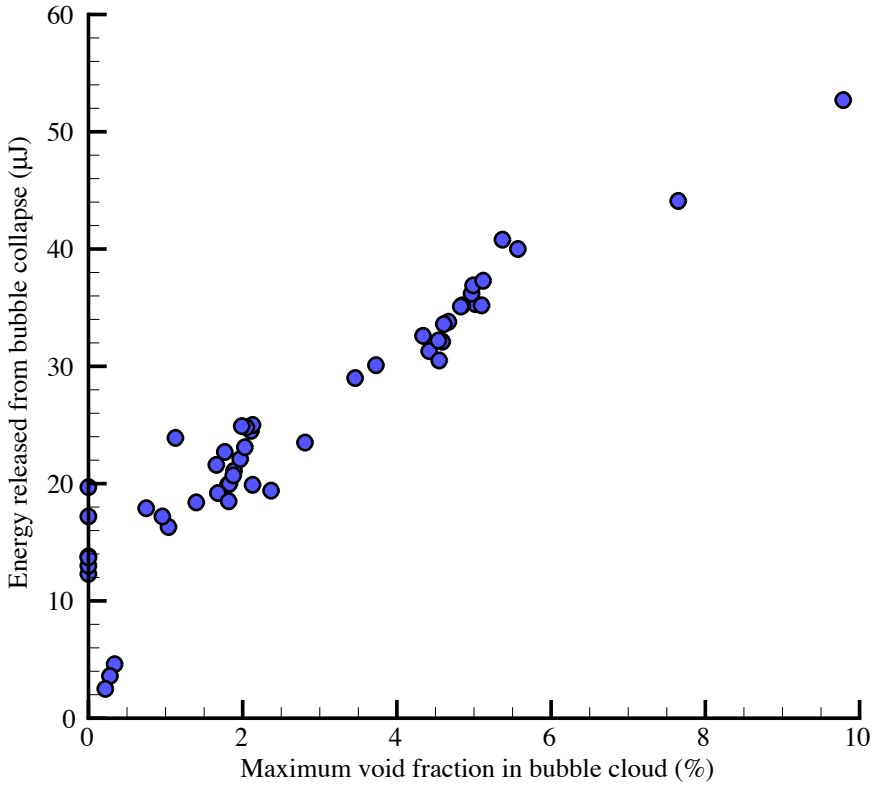

Figure 3.23: Relationship between the energy released by bubble collapse and maximum void fraction. Data shown was taken from Table A.3 in Appendix A.

3.3 Dual-pulse and partially obstructed lithotripter

3.3.1 Bubbles and pressure superposition in dual-pulse lithotripter

In the work of Sokolov *et al.* (2001), the pressure at the focus of a dual-pulse lithotripter was observed to be approximately equal to twice that of a single-pulse lithotripter. Since pressure-related nonlinear effects are small[2], it would be expected that the pressure field of the dual-pulse lithotripter can be approximated by the superposition of the pressure field from two single-pulse lithotripter. As expected, Figure 3.24 shows that the pressure at the focal point for the dual-pulse lithotripter model is approximately twice that observed in the conventional lithotripter for identical simulation parameter in the absence of bubbles.

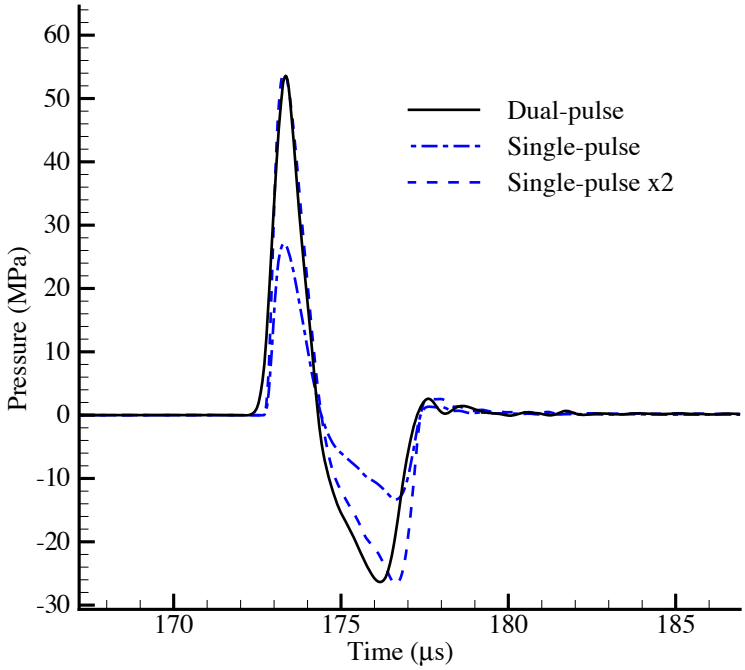

Figure 3.24: Comparison between pressure at focus for the dual-pulse and single-pulse lithotripter using the present model with zero void fraction.

Using the pressure profiles presented in Figure 3.24, the following bubble response can be obtained (see Figure 3.25). For the decoupled case ($N_o = 0$), the time to collapse for the dual-pulse is approximately 430 μs while it is 167 μs in the conventional lithotripter. This is an increase of over 2.5 times which is larger than the 1.8 factor reported in Sokolov *et al.* (2001). An interesting effect seen in all dual-pulse simulation is the impact of the refocused wave. The propagating waves originated from each lithotripter are eventually

[2]At the maximum pressure, the speed of sound in the liquid increases by less than 3%.

refocused by the reflector of the opposing lithotripter and reach the F_2 point at approximately 544 μs. The impact of the refocused wave can be seen in Figure 3.25 where the pressure pulse created a small spike in the bubble response.

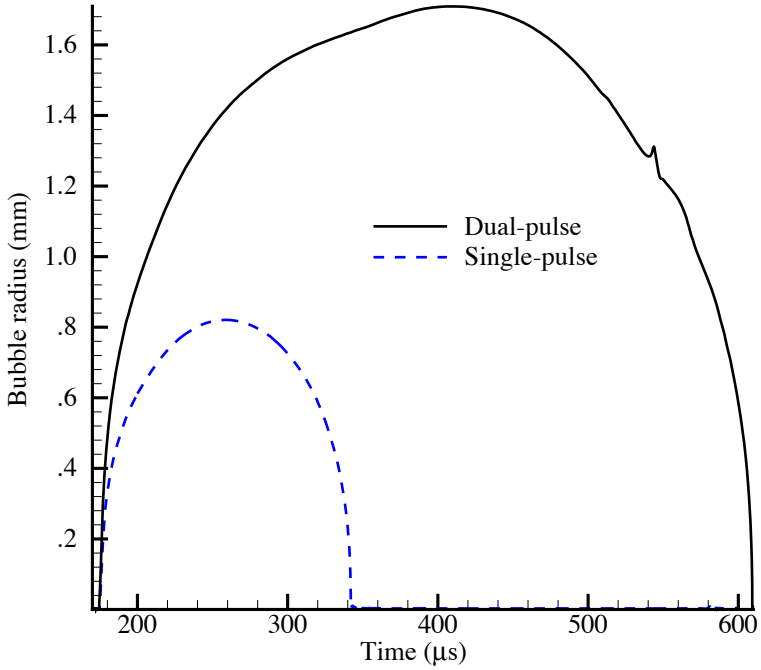

Figure 3.25: Comparison between bubble response at focus for the dual-pulse and single-pulse lithotripter using the present model with zero void fraction.

3.3.2 Structure in the dual-pulse bubble cloud

If the zero void fraction assumption is relaxed, differences begin to appear in the shape of the bubble cloud in the focal region of a dual-pulse lithotripter. Figure 3.26 presents a comparison between a decoupled simulation (rightmost column) where the void fraction is assumed to be negligible for the purpose of computing the mixture pressure, a simulations with coupled interaction (third and fourth columns from the left) and experimental results (first three columns from the left). It is interesting to note that the portion of the bubble cloud along the axis of symmetry for the decoupled case is similar in size and shape to the ones observed in the coupled simulations. However, the coupled approach is able to predict the observed growth of bubbles in the prefocal region. The fundamental shape of the bubble cloud in the simulations has been altered by the coupled effects between the pressure and bubble field.

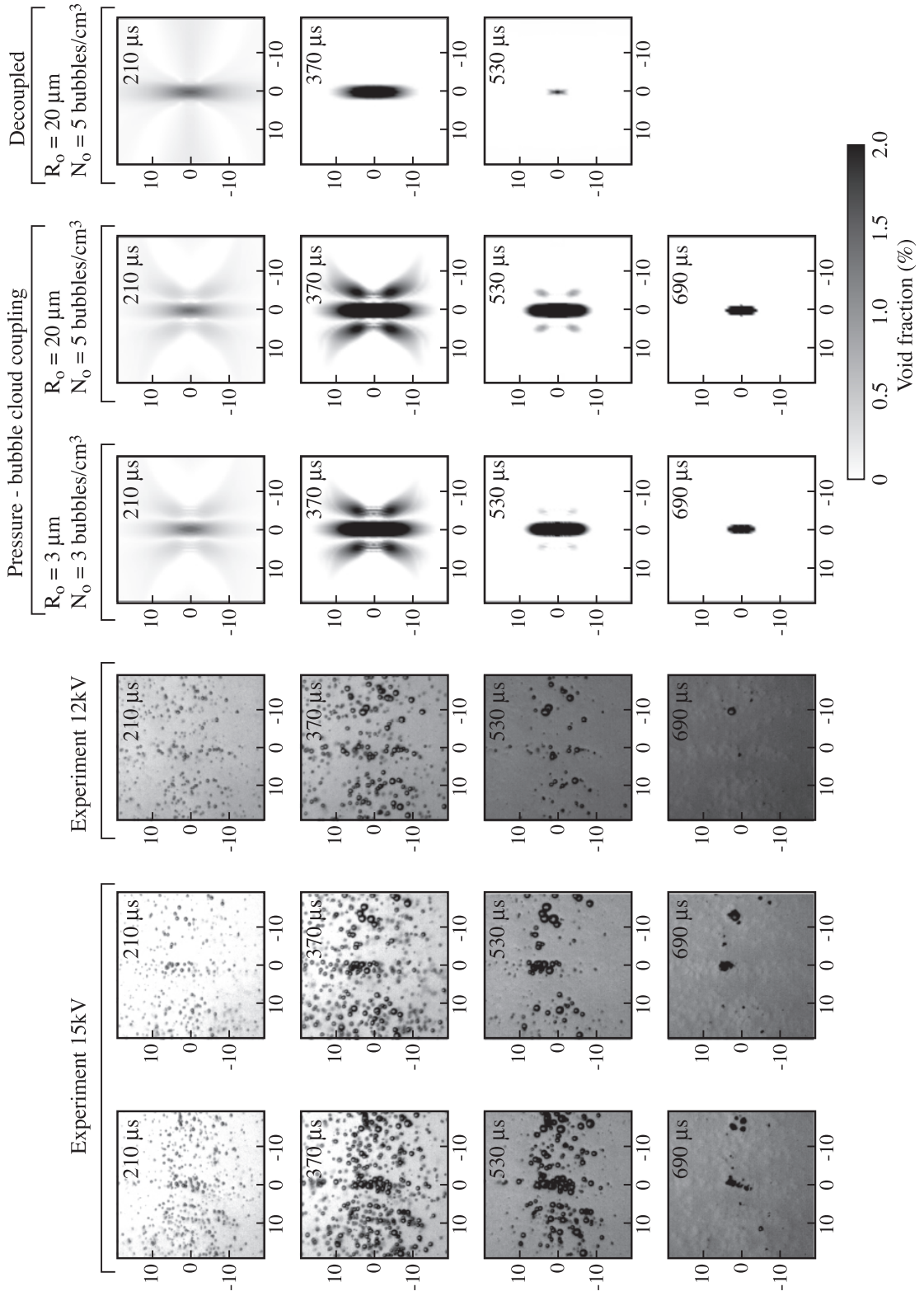

Figure 3.26: Comparison between experimental observation and numerical simulations of the bubble cloud in the focal region of a dual-pulse lithotripter. Experimental results are a courtesy of Dahlia L. Sokolov, Center for Industrial and Medical Ultrasound, Applied Physics Lab, University of Washington, Seattle.

Although the dimensions of the modeled bubble cloud are not an exact match to the experimental photographs, the present coupled approach does provide a significant improvement over the previous decoupled model, which is equivalent to the zero void fraction case. The numerical model predicts a smaller (3 cm wide instead of the 4 cm reported in Sokolov *et al.* (2001)) and shorter (3 cm long instead of the 4 cm reported) bubble cloud. However, the numerical model does predict the presence of a gap of lesser cavitation activity. This band is found at the observed location but is smaller than the 2 mm gap reported Sokolov *et al.* (2001). A clearer view of the gap in the cavitation cloud can be seen in Figure 3.27 where the bubble radius along the axis of symmetry is plotted. Based on these results, it is clear that the presence of the observed gap in the bubble cloud can be explained by the interaction of the bubble field and the propagation of the shock waves. The discrepancies in the cloud dimensions can be explained by void fraction limitations in the numerical model. The void fraction in the focal region of the dual-pulse lithotripter can rise up to the order of 15% while the effectiveness of the numerical model decreases rapidly for void fraction larger than 1%.

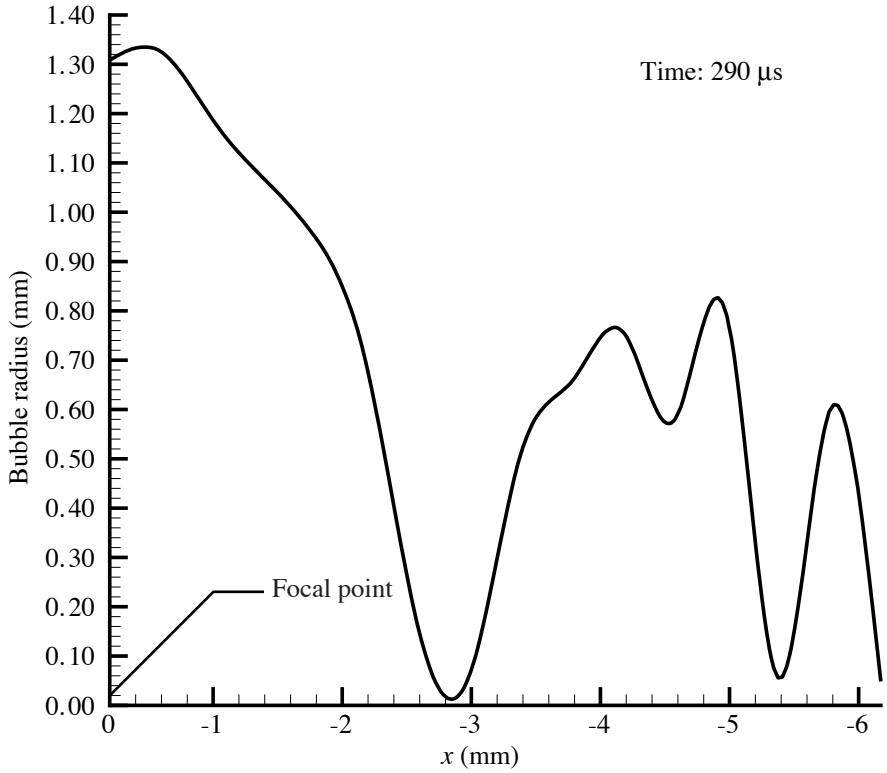

Figure 3.27: Bubble radius along the axis in the focal region of a dual pulse lithotripter (focus $x = 0$, $t = 290$ μs, $R_o = 5$ μm, $N_o = 5$ bubbles/cm^3).

For typical dual-pulse lithotripter simulations with non-zero void fraction, the maximum bubble radius was found to be approximately 1.9 mm, which is about a 2.3 times increase over the peak bubble radius

in the single-pulse lithotripter model. This value is significantly larger than the 1.1 mm peak bubble size reported in Sokolov *et al.* (2001).

3.3.3 Impact of an artificial stone in the lithotripter field

To facilitate laboratory experiments, many different materials have been used to make artificial stones. Typically, these stones will be cylindrical in shape and of the order of a half a centimeter in diameter and one centimeter in length. Although the present model is limited to the representation of perfectly rigid objects, the numerical results can nonetheless present interesting results. Figure 3.28 present the void fraction contour for a low void fraction simulation where a rigid cylindrical object has been placed at the focal point.

From the numerical simulations, the time to collapse for the bubble cloud generated in front of the stone can be found to be between 247 and 323 μs depending on the initial conditions (see table A.5). These values are significantly smaller than collapse time observed in experiments (approximately 700 μs Bailey *et al.* (2003)). In order to understand the cause of this discrepancy, two factors must first be considered. First, the numerical results for cases without cloud cavitation yield a collapse time between 159 to 179 μs (see table A.5). Therefore, the presence of cloud cavitation caused an increase of approximately 1.7 times in the time to collapse which is similar to the increase seen in the dual-pulse lithotripter. A second observation is the impact of the reflection due to the artificial stone. In the numerical simulations where the stone is treated as a perfect reflector, the reflected wave significantly reduced bubble growth and lifetime. However, the actual material behavior of an artificial stone, although much less compressible than the liquid, is far from acting as a perfect reflector. The occasional spalling failure observed in experiments clearly indicate that a non-negligible part of the incident shock wave is transmitted through the stone. At the present stage, we believe that given a more realistic boundary condition for the numerical representation of the stone (possibly including the effect of shear waves), the region in front of the stone would exhibit longer bubble growth. Combined with the effects of cloud cavitation, we would expect a time to collapse much closer to the experimental observations. This hypothesis can be verified in future work by the introduction of a numerical model for the behavior of the stone and also by performing similar experiments with materials with significantly different sound speeds[3].

In their work, Sokolov *et al.* (2002) reported that prefocal positioning (of the order of 20 mm) of an

[3]For hardened steel or Pyrex glass, we would expect the reflection to be stronger and yield bubble cloud with shorter time to collapse.

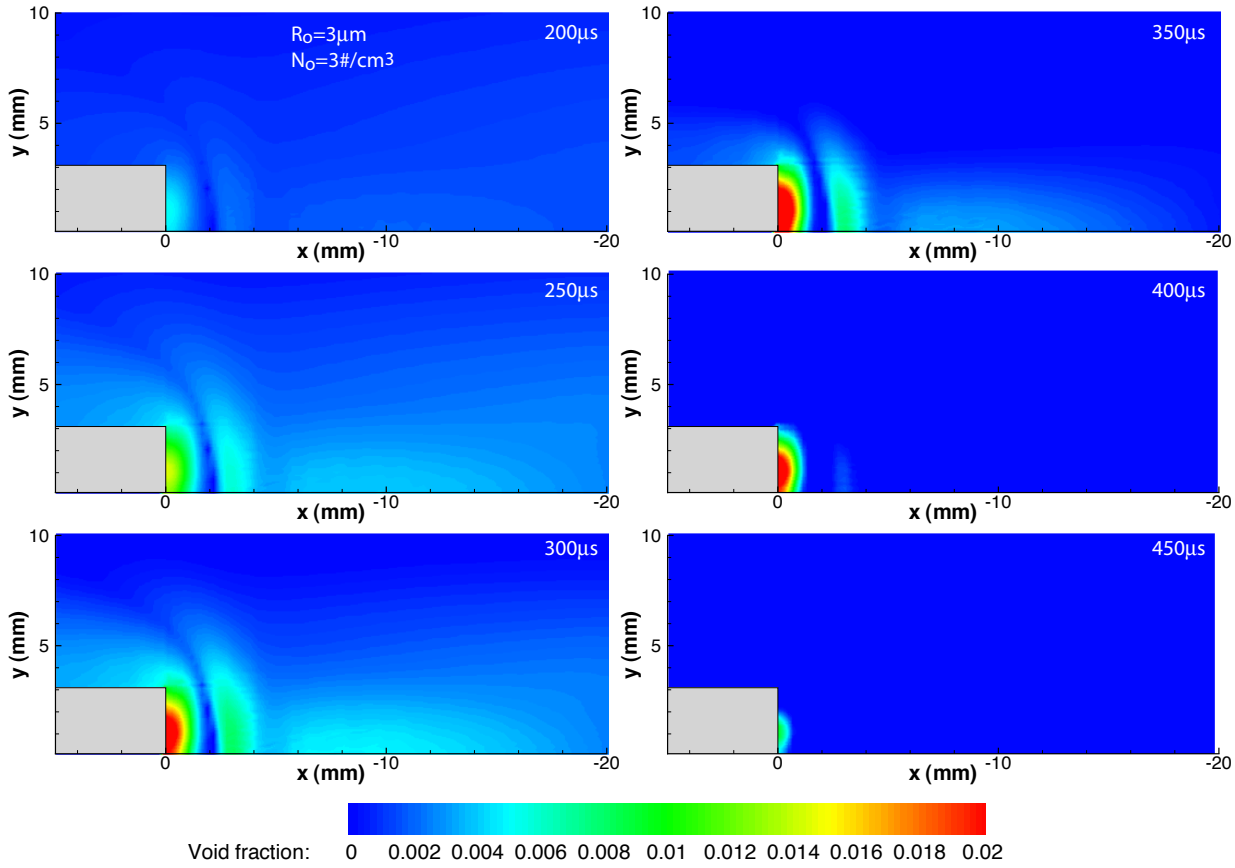

Figure 3.28: Snapshot of void fraction contours for lithotripter with artificial stone at focus.

artificial stone resulted in faster comminution in *in vitro* experiments. Using the present model, various simulations were conducted to investigate this empirical observation. As seen in Figure 3.29, the present numerical model predicted similar shapes and sizes for the bubble cloud in front of the stone. Based on these preliminary calculations, the differences in the intensity of the pressure field and minor fluctuation in maximum void fraction would suggest that optimal stone comminution should occur anywhere between the focal point and a few millimeter (less than 5 mm) behind it (post-focal). It is important to note that as mentioned previously in discussing the comparison between the observed and predicted bubble clouds in the free-field lithotripter, the high-speed photography shows that the bubble cloud is typically centered approximately 10–20 mm before the focal point. Consequently, a more general conclusion is that stone comminution should be the most effective at the center of the free-field bubble cloud. If correct, this conclusion would be consistent with the numerical results shown in Figure 3.29.

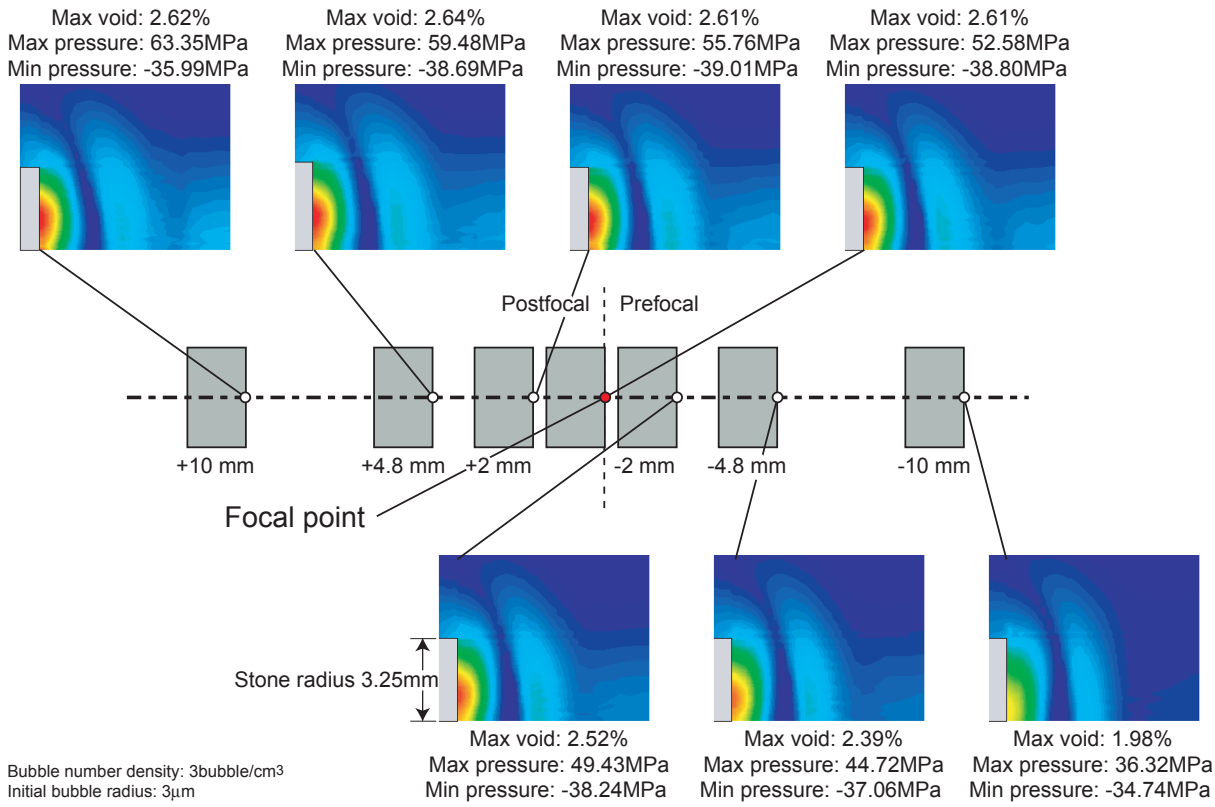

Figure 3.29: Snapshot of void fraction contours for different stone positions.

3.3.4 Impact of a large cylindrical reflector in the field of a lithotripter

In the work of Lokhandwalla (2001), a two-inch metal cylinder was introduced in the field of the Caltech-EHL. For cases where the reflector was located 20 mm post-focus, the part of the bubble cloud in the neighborhood of the focal point was observed to behave differently from the part located in front of the reflector. At the focal point, cavitation detectors measured a time to collapse similar to the free-field case ($t_c \approx 287 \pm 19\ \mu s$). This suggests that the reflector is sufficiently far away such as not to impact the bubble field at the focus. Additionally, in the region in front of the reflector, the observed time to collapse was approximately doubled ($t_c \approx 452 \pm 89\ \mu s$) which suggests that the reflector is sufficiently large to behave in a similar fashion as the dual-pulse reflector. A similar behavior is predicted by the present model. Figure 3.30 presents a comparison for the bubble cloud for two different set of input parameters (bubble nuclei size and density). Although the value for the time to collapse for the different locations are smaller than the observed one, the ratio of the t_c at the base of the reflector and the focal point compares very well to the empirical observations (left case: 1.53; right case: 1.57; experiments: 1.58).

An important observation that can be made from Figure 3.30 is the presence of a gap in the bubble field in front of the reflector. This is not surprising since this configuration is similar to the dual-pulse case. However, an noteworthy difference is that in this case, the lithotripter wave has a much smaller amplitude when it reaches the reflector (20MPa instead of 70MPa).Accordingly, the maximum void fraction reached is significantly less than for dual-pulse cases (3% instead of 7-15%) and consequently, permits a more accurate representation of the cavitating field by the numerical model.

It is interesting to note that similar pressure wave as observed in the collapse of a bubble cloud in a free-field lithotripter can be observed during the collapse of the bubble cloud in front of the reflector. Although the pressure waves in this case are not as clear, pressure increase due to the overall cloud collapse can be seen in Figure 3.31.

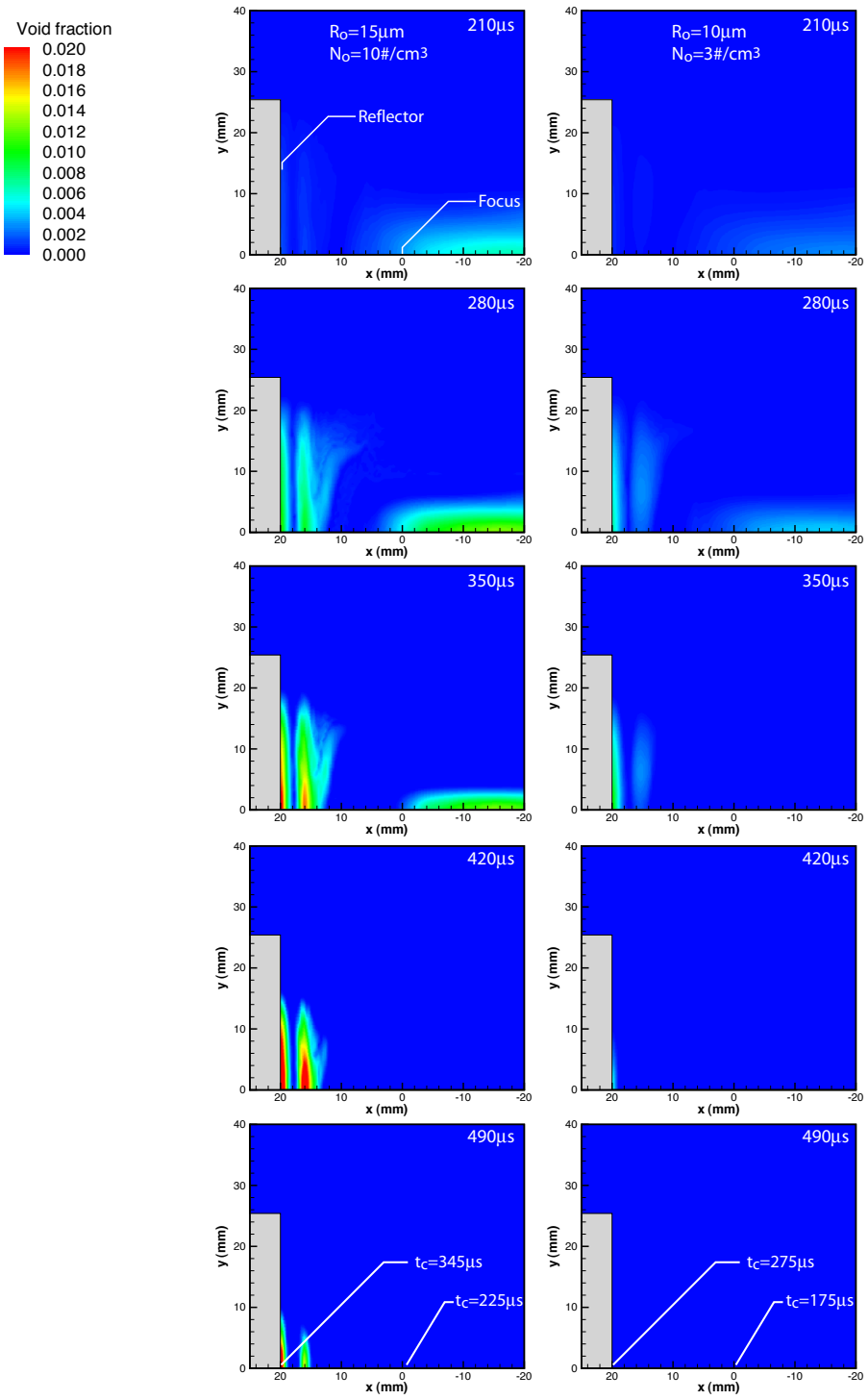

Figure 3.30: Comparison of predicted void fraction contours for flat reflector located 20 mm post-focal.

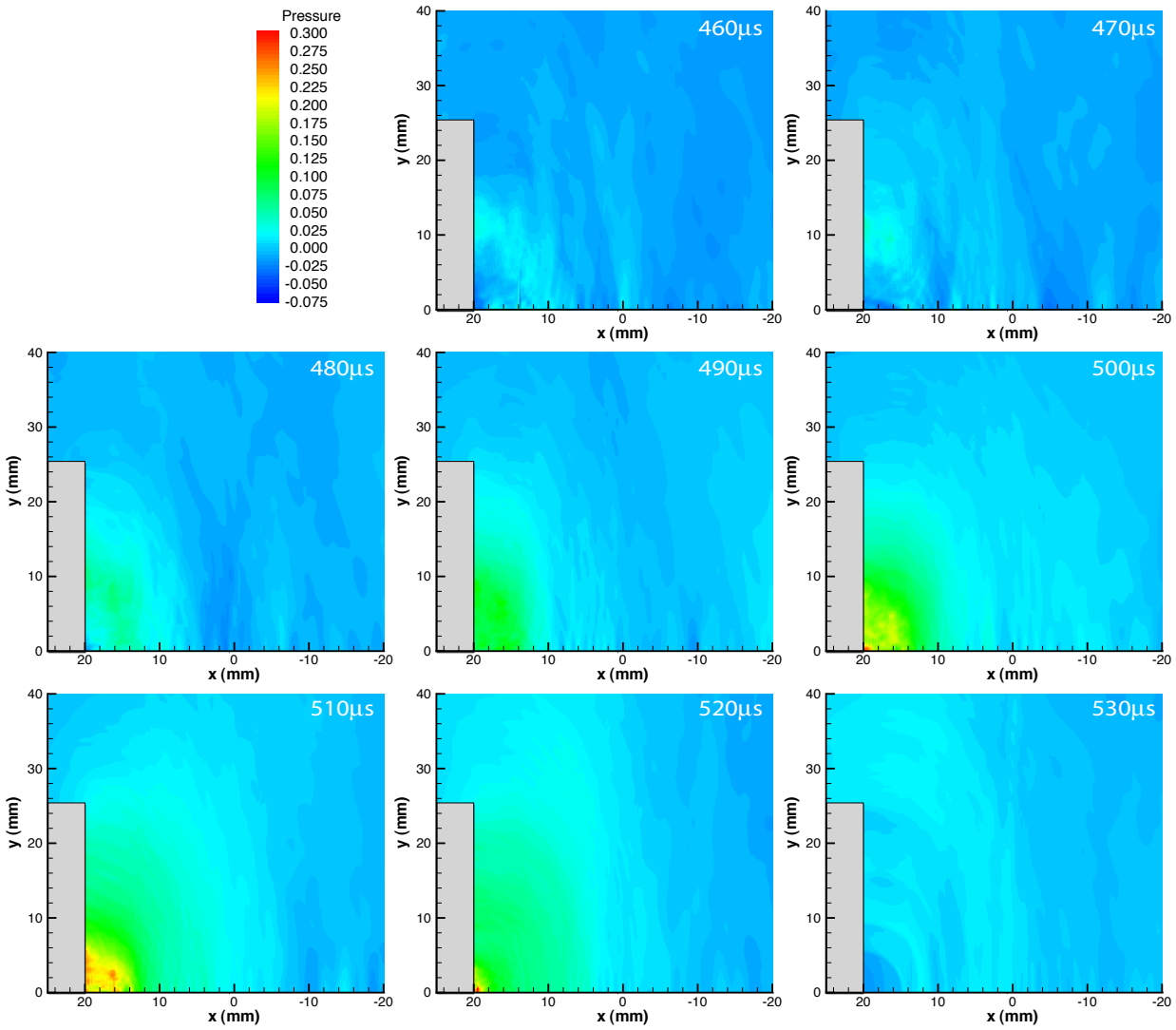

Figure 3.31: Pressure field in the focal region during collapse of the bubble cloud in front of a flat reflector located 20 mm post-focal.

3.4 Pulse-repetition frequency

From *in vitro* experiments, it has been noted that the frequency of shock firing can have a measurable impact on the amount of damage inflicted on the stone (Lifshitz *et al.* 2000, Weir *et al.* 2000 and Paterson *et al.* 2002b). Typical pulse-repetition frequency for clinical treatment is of the order of 1 Hz. While many clinicians tend to use frequencies up to 2 Hz in order to minimize the duration of treatment, empirical evidence suggests that a frequency of 1/2 Hz is not only more effective at stone comminution but also minimizes tissue damage (Paterson *et al.* 2002b). As previously mentioned in Section 1.4, one mechanism by which PRF impacts the treatment performance is by altering the equilibrium size of bubbles in the mixture. Using the model describe in Appendix G, we were able to compute the net amount of gas diffusing from the liquid into a bubble subjected to a typical lithotripsy pulse and the resulting equilibrium bubble radius. For the results presented here, the calculations were based on the assumption that the liquid was degassed to 100 Torr, or 13.2% of saturation concentration, a typical value used in experiments.

3.4.1 Single bubble analysis

Using the single bubble with gas diffusion model, we can obtain a first level analysis of the pulse-repetition case. For a given time delay between pulses, the bubble model can be used to predict the accumulation of gas inside the bubble after a series of identical pulses. Figure 3.32 shows the increase in noncondensible gas and the bubble radius for four consecutive pulses half a second apart using the pressure waveform developed by Church (1989). As mentioned in Section 1.2, this waveform has been used to fit experimental measurements and has been used as a pressure pulse model for single bubble numerical simulation (Matula *et al.* 2002). The pressure model and the parameter used here were taken from Matula *et al.* (2002) and are shown below (see Figure 3.33):

$$P(t) = 2P_{\max} e^{-\alpha t} \cos\left(\omega t + \frac{\pi}{3}\right), \tag{3.5}$$

$P_{\max} = 35$ MPa,

$\alpha = 35$ MHz,

$\omega = 2\pi 50$ kHz.

After a sufficient number of pulses, the bubble reaches an equilibrium where the mass of gas acquired

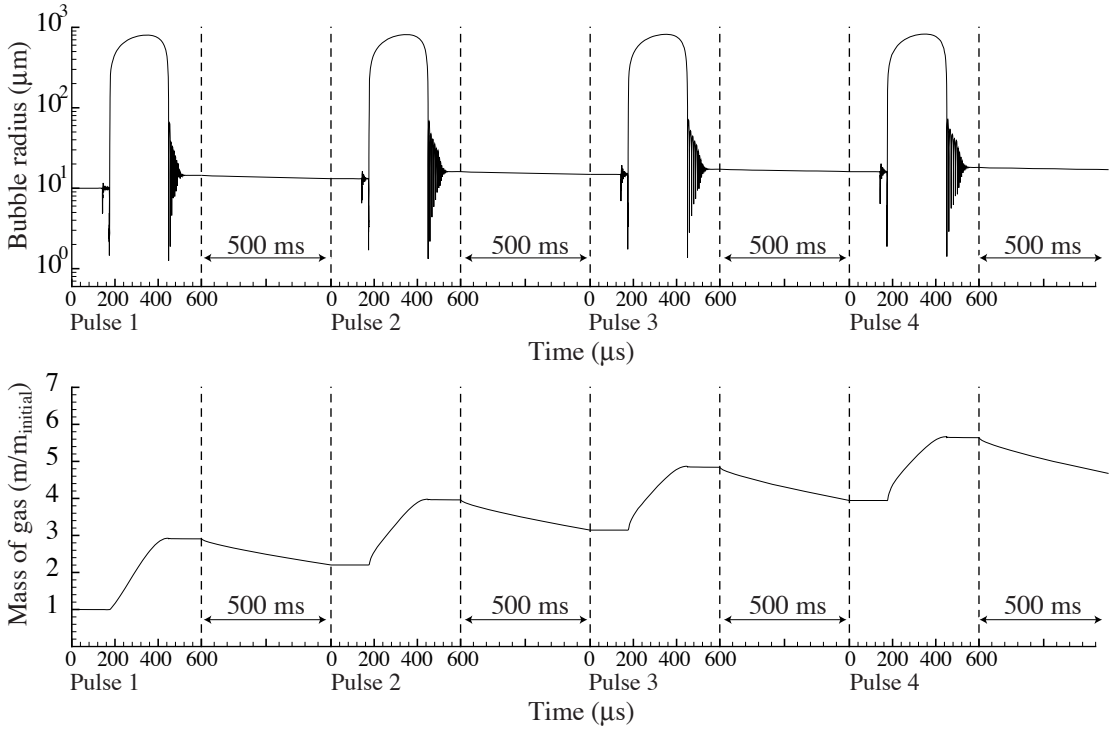

Figure 3.32: Equilibrium radius for single bubble stimulated by train of lithotripsy pulse at 1/2 Hz.

during growth is balanced by the gas lost during the interval between pulses. In Figure 3.34, the increase in bubble radius between two pulses is plotted as a function of the initial bubble radius. The zero increase crossover point thus determines the bubble radius for which a dynamic equilibrium is reached. From Figure 3.34, the bubble radius converges to 57 μm for a 0.5 Hz pulse frequency while the bubble radius converged to 84 μm for the 2 Hz pulse frequency (for the Church waveform).

3.4.2 PRF in free-field lithotripter

The impact of the pulse rate frequency on the effectiveness of the lithotripter is far ranging. As seen in Table A.3, the results are strongly dependent on the equilibrium bubble radius R_o which, as discussed in the previous section, is determined by the PRF.

Based on the theory covered in the previous section and the results in Table A.3, several observations can be made regarding the energy released by a collapsing bubble:

- in absence of cloud interactions (low void fraction), energy increases with equilibrium radius R_o,
- the energy released can be substantially increased due to cloud interactions,

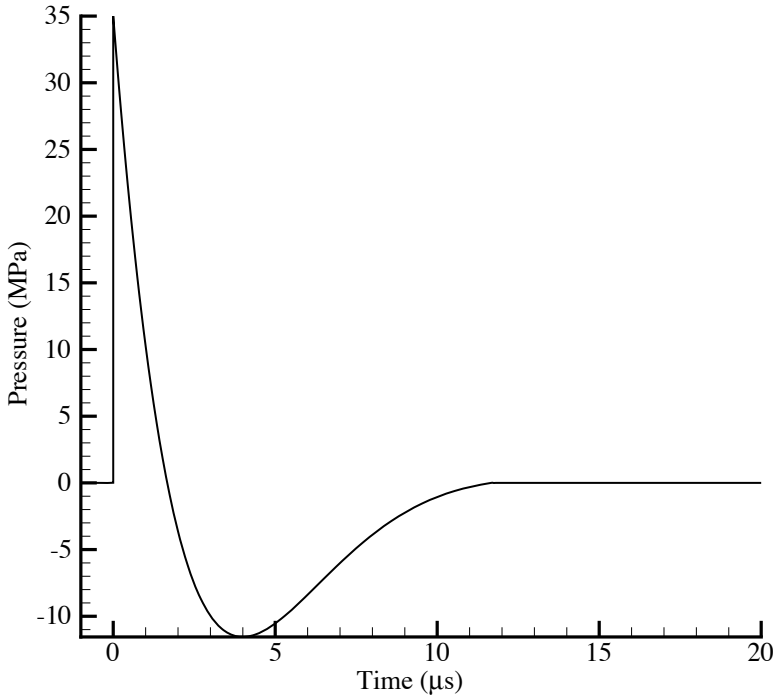

Figure 3.33: Church-based pressure pulse used for single bubble PRF analysis.

- shock wave focusing is hindered (lower peak pressure) by high void fraction mixture,
- lower peak shock wave pressure results in lower maximum bubble radius $R_{\max}$.

From these observations, initial conditions promoting energetic bubble collapse should include high bubble number density and an intermediate bubble equilibrium size. Consequently, given a particular value of the bubble number density there should be an optimal value of equilibrium radius for which a bubble delivers a maximum of energy during its collapse.

The bubble energy for different equilibrium radius and number density is presented in Figure 3.35. The optimal equilibrium radius for a maximal energy release can be clearly identified from these results. For a number density of $N_o = 20$ bubbles/cm^3, the optimal bubble nuclei is approximately $R_o = 20\ \mu m$ while for a number density of $N_o = 10$ bubbles/cm^3, the optimal nuclei size is in the range of $20 - -35\ \mu m$. In order to provide a more insightful comparison, the energy released was renormalized with respect to the limiting case of null number density and very small bubble nuclei (see Figure 3.35).

By calculating the amount of noncondensible gas diffusing into the bubble during its growth and the subsequent degassing, the pulse rate frequency corresponding to a particular case was determined. The computation is similar to that described in Section 3.4.1, but the actual pressure history from simulation is

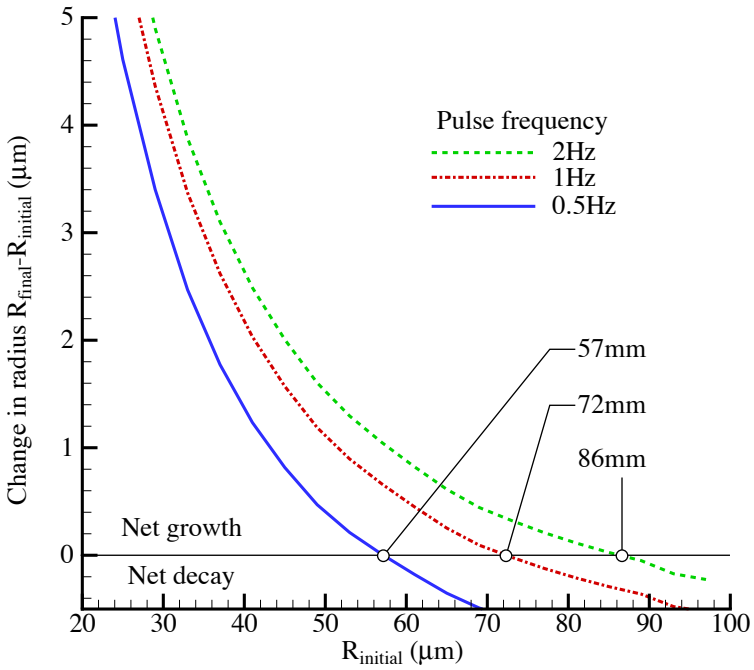

Figure 3.34: Bubble radius increase after one pulse.

used instead. Figure 3.36 presents the normalized energy as a function of the PRF. From this figure, the optimal frequency for $N_o = 20$ bubbles/cm^3 is approximately 1 Hz while the case $N_o = 10$ bubbles/cm^3 has an optimal frequency of approximately 2 to 5 Hz.

After a closer examination of Figure 3.36, several important observations can be made. As discussed in Section 3.2.3, the energy released by the bubble collapse at the center of a cloud can be from 2 to 3.5 times that of a single bubble collapse ($N_o = 0$ bubbles/cm^3) case) depending on the bubble number density. However, as shown in Figure 3.37, an increase in the initial void fraction also results in reduced shock wave intensity at the focal point (shielding). From Figure 3.36, the cross-over point where cloud shielding overtake and beneficial effect of cloud collapse occurs at a PRF of approximately 30 Hz. We note that in Figures 3.35 and 3.36, a measure of the uncertainty of the results is shown in order to indicate that trends in the plots are significant. The error bars are based on an analysis presented in Appendix B.

3.4.3 Impact of lithotripter intensity

To further understand the impact of treatment parameters on the effectiveness of lithotripsy, the amplitude of the initial spherical pulse was varied. The exact impact of changing the intensity level (voltage) of a lithotripter is difficult to ascertain. Figure 3.38 presents the data collected for the peak pressure at the

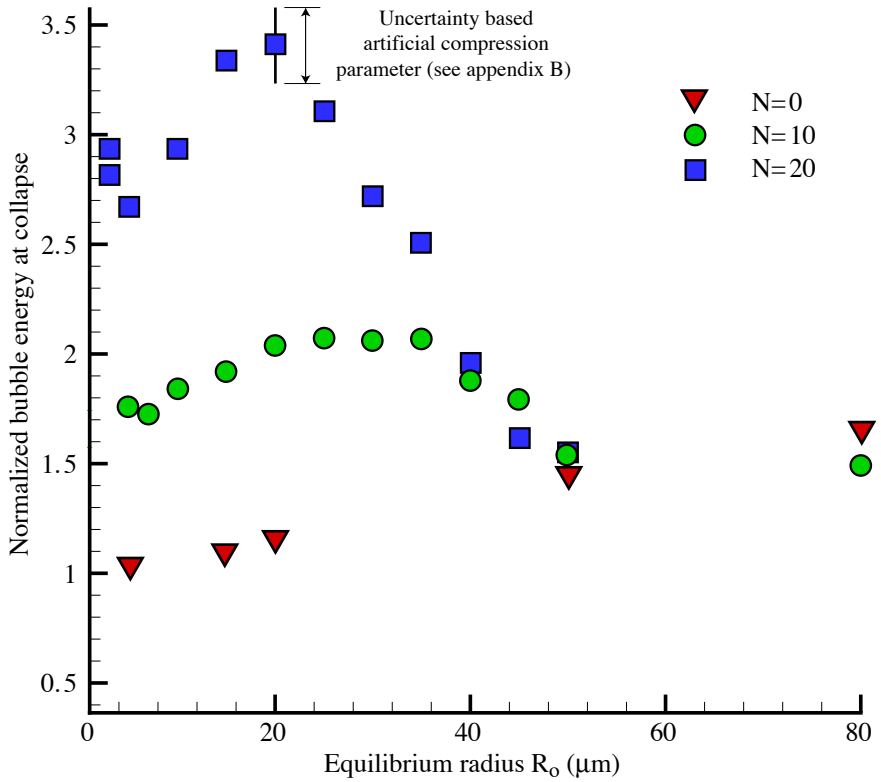

Figure 3.35: Normalized energy released at bubble collapse as a function of equilibrium radius R_o.

focal point from three different Caltech-EHL for their various voltage settings (Cleveland *et al.* 2000). As a comparison, Figure 3.39 presents the values of peak pressure at the same location using our numerical model as a function of the energy of the spherical shock wave in the initial conditions. Because of limitations in the numerical model, the range of input energy that can be accurately computed is limited. Although a precise one-to-one correspondence between the input energy and voltage setting is impossible to establish, one is clearly related to the other.

The selection of the amplitude setting has a clear impact on the conditions at the focal point. As seen in Figure 3.40, the increased amplitude of the shock wave translates into an increase in the collapse energy of a bubble at that location. Based on this result, it would appear that the most efficient lithotripter should be the most powerful one. However, increasing the shock wave amplitude also increases the maximum size and duration of bubbles within the cloud. Consequently, the bubble nuclei in the focal region will increase in size due to the added mass transfer, unless the PRF setting is appropriately reduced.

For the runs shown in Figures 3.39 and 3.40, the PRF value for which the nuclei size is preserved, can be calculated using our post-processing model. As seen in the data labels in Figure 3.40, an increase of 50%

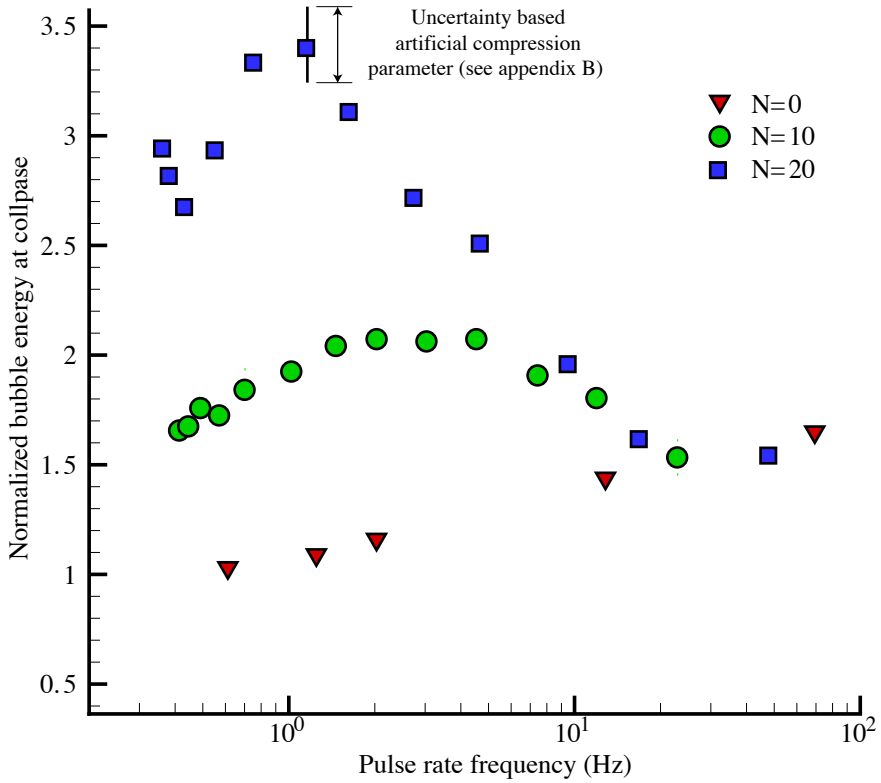

Figure 3.36: Normalized energy released at bubble collapse as a function of pulse rate frequency.

in the initial pulse energy requires a decrease of over 200% in the pulse rate frequency. Otherwise bubble nuclei will grow and result in increased bubble cloud shielding. The rapid decrease in PRF associated with higher amplitude suggests significantly longer treatment. However, if we assume that the energy released in the bubble collapse is a valid surrogate for the damage inflicted on the stone, then a measure of damage per treatment duration can be obtained by multiplying it by the PRF. Figure 3.41 presents this damage rate as a function of the initial pulse energy. It is interesting to note that for given conditions of the bubble field, the damage rate is rather insensitive to the pulse strength. Based on the error bars, we can conclude that within the uncertainty of the model, no significant trend can be established and that given a desired bubble nuclei size and number density (optimal or otherwise), the rate of stone comminution is not likely to improve with increasing lithotripter intensity level. This observation is especially interesting in that it provides for an additional degree of freedom in the selection of treatment parameters. Within this range of pulse intensity and corresponding repetition frequency, an appropriate combination can be selected such as to minimize tissue damage while still preserving an optimal *rate* of stone comminution.

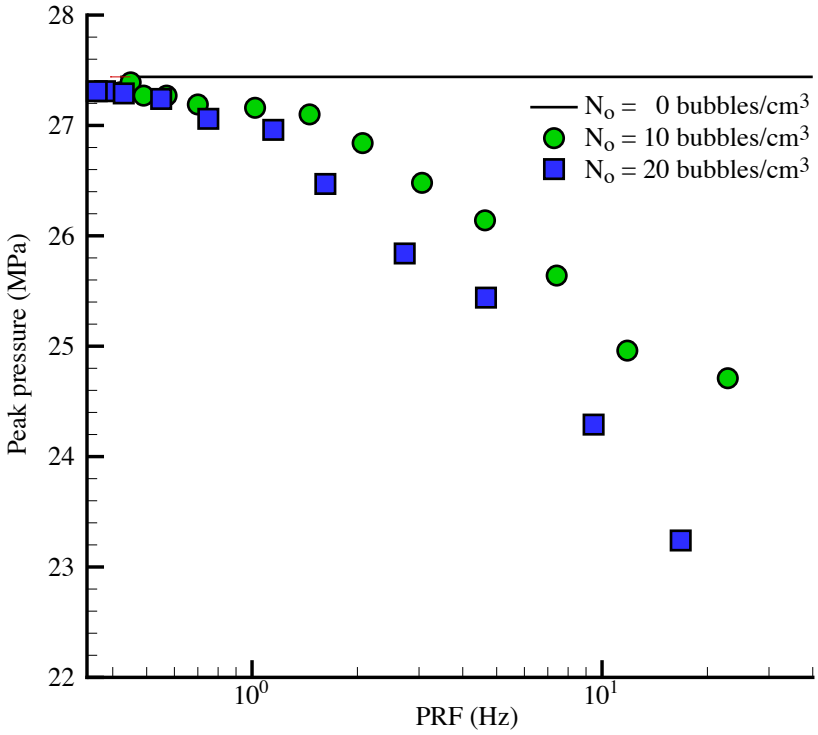

Figure 3.37: Impact of bubble cloud shielding on the peak pressure at the focal point.

3.4.4 PRF and artificial stone in lithotripter field

Because the simulation data was easier to interpret, the analysis in the previous section focused on cases without a stone present in the field. The added reflections due to an artificial stone complicated the analysis of the flow in the focal region. However, we believe that effects such as bubble cloud shielding and cloud interactions during collapse are still present in cases with stone. Even though pressure waves associated with the collapse of the bubble cloud cannot be as readily identified in the results, bubble cloud interactions can increase energy released by a collapsing bubble locate in front of the stone by a factor of up to 5 to 6 times. Figure 3.42 presents the normalized [4] energy release in front of the stone as a function of the PRF. Note that the corresponding PRF for each simulation was calculated following the same post-processing procedure as in the free-field case.

During the collapse of the cloud, bubbles may fission into smaller nuclei, which would increase the bubble number density and nuclei size present for the following shock wave. In addition, bubbles can dissolve into the liquid while new bubbles can be nucleated by the passage of the next shock wave. These effects are partly

[4] As in the free-field case, the energy was normalized by the energy released by a small bubble in the absence of cloud interaction (decoupled case).

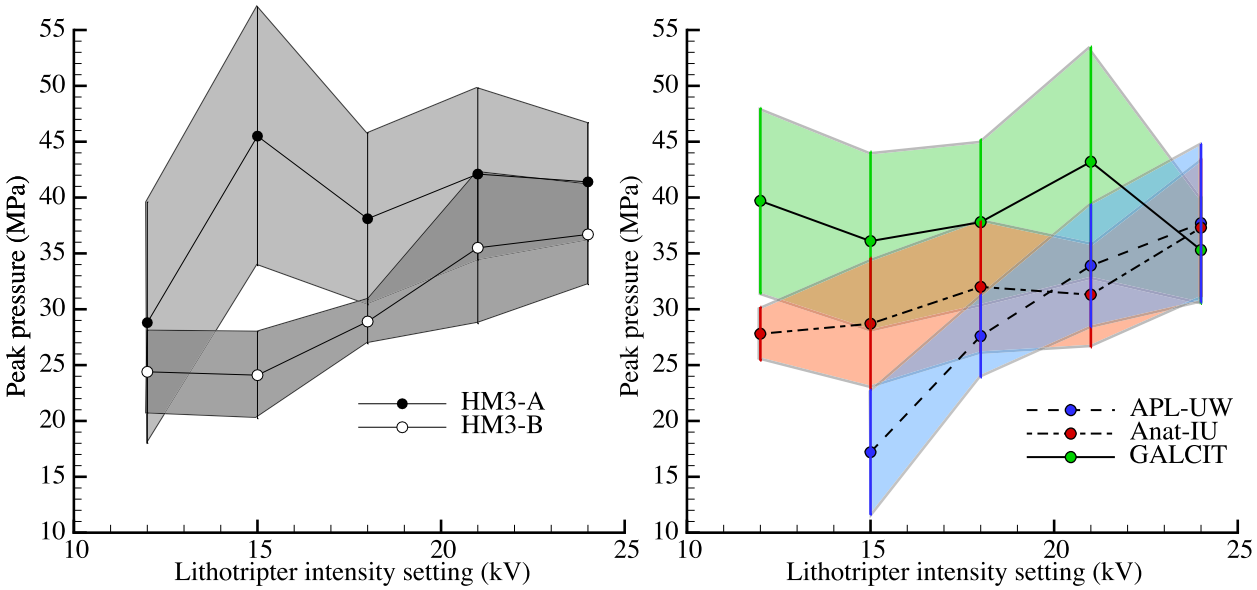

Figure 3.38: Experimental measurements of peak pressure at focus as function of lithotripter voltage for Dornier's HM-3 (two machine: HM3-A and HM3-B) and Caltech-EHL (three machine: APL-UW, Anat-IU and GALCIT). Data from (Cleveland *et al.* 2000).

function of the PRF and can significantly alter the number density in the focal region. Since they occur in the aftermath of the shock wave while bubbles are too small to be observed, these phenomenon cannot be quantified directly but are observed indirectly via the relationship between bubble number density and PRF (Sapozhnikov *et al.* 2002). Currently, there are no numerical models able to predict accurately these processes. Consequently, the relationships between PRF and the bubble size nuclei presented in this work do not reflect the impact of any of these bubble generation/destruction mechanisms.

3.4.5 Concentration of gas in solution

As mentioned in the beginning of this section, the PRF calculations presented above were based on the assumption that the liquid was degassed to 100 Torr which corresponds to a concentration 13.2% of the saturation concentration. Although the concentration of non-condensible gas can be monitored and controlled for *in vitro* experiments, the concentration for *in vivo* applications can vary greatly (for example, the normal partial pressure of arterial blood gases can range from 100 to 150 Torr). Using the numerical results from a typical free-field case, the corresponding equilibrium bubble radius was computed for a range of gas concentration and PRF (see Figure 3.43). Selecting a cross section of this plot corresponding to a PRF of 1 Hz, the bubble equilibrium size can change significantly depending on the partial pressure of non-condensible gas. Following these observations, the *in vitro* testing of the present numerical predictions regarding PRF

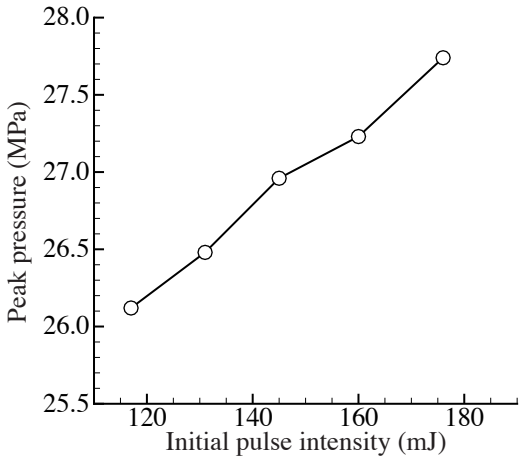

Figure 3.39: Peak pressure at focus as function of initial shock wave energy for the present numerical model for the case $N_o = 20$ bubbles/cm^3, $R_o = 20\mu m$.

should be conducted in a carefully monitored liquid.

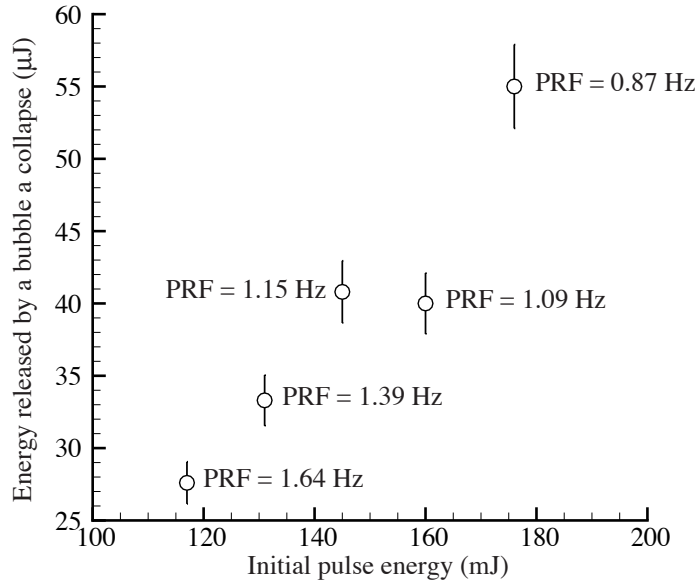

Figure 3.40: Energy released at bubble collapse as a function of initial pulse energy for the case N_o = 20 bubbles/cm^3, $R_o = 20\mu m$.

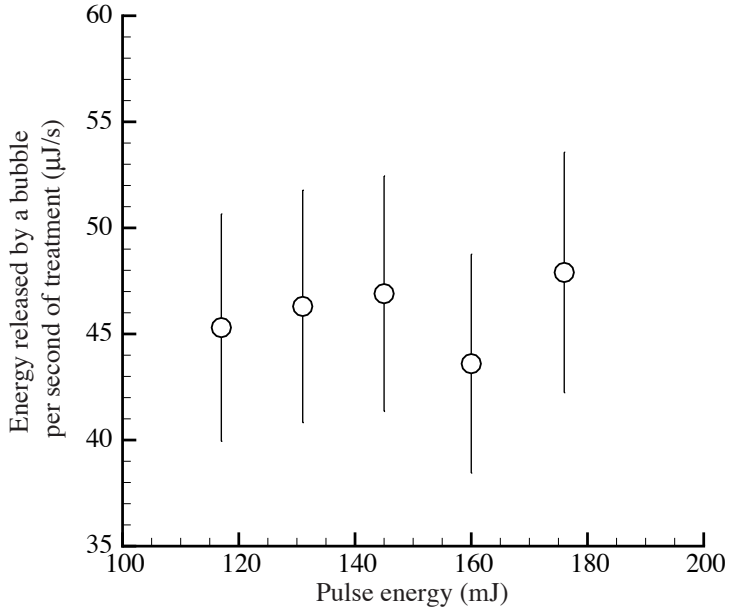

Figure 3.41: Energy released by a collapsing bubble per second of treatment as a function of initial pulse energy for the case $N_o = 20$ bubbles/cm^3, $R_o = 20\mu m$.

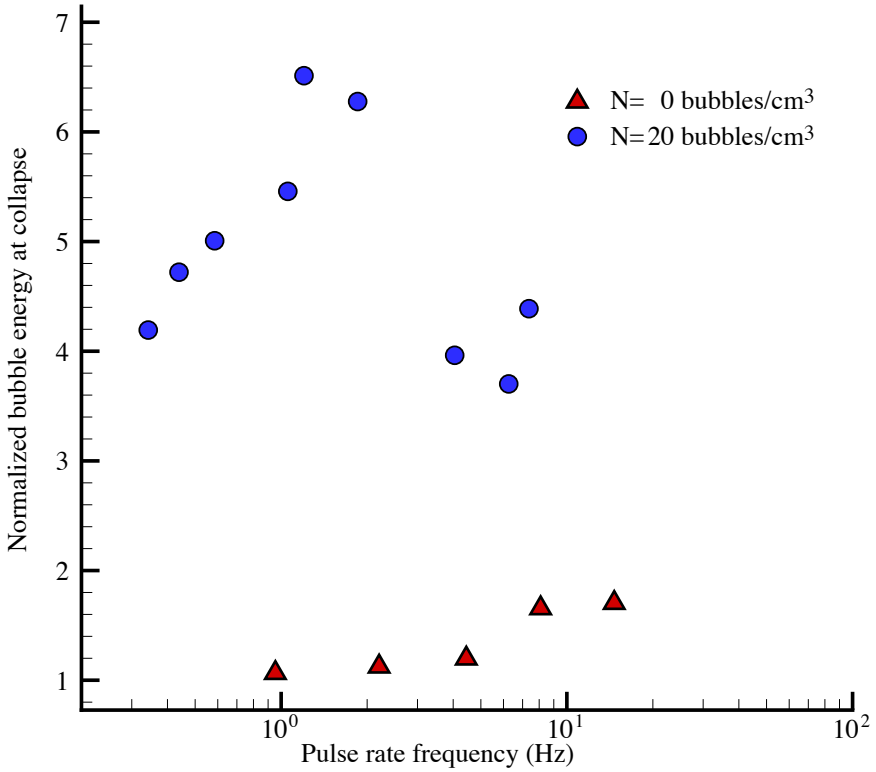

Figure 3.42: Normalized energy released at bubble collapse in front of an artificial stone as a function of pulse rate frequency.

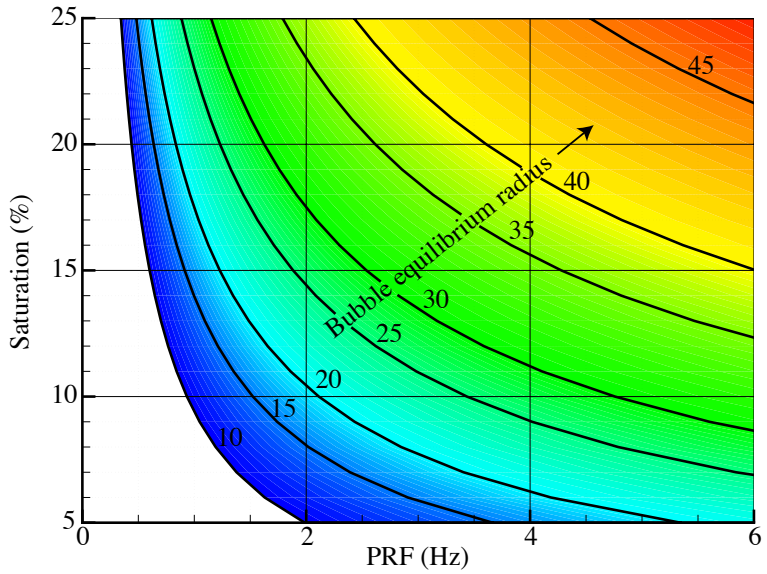

Figure 3.43: Contours of bubble equilibrium radius as a function of concentration of non-condensible gas (in % of saturation) and PRF.

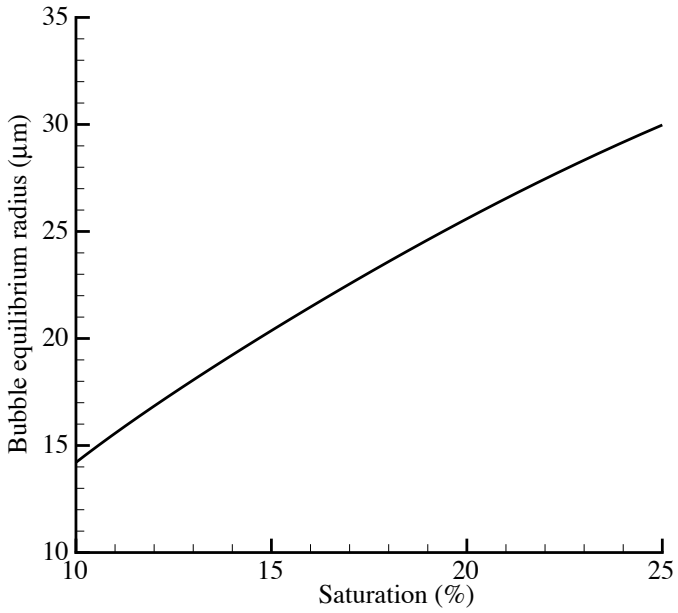

Figure 3.44: Corresponding bubble equilibrium radius for different concentration of non-condensible gas (in % of saturation) for a PRF of 1 Hz.

Chapter 4

Summary

4.1 Final conclusions

In this study, a numerical model of the cavitating flow in an electrohydraulic lithotripter was implemented, tested and used to provide new details on the mechanism of stone comminution. This numerical model is based on an ensemble averaged two-phase flow model, first proposed by Zhang & Prosperetti (1994), modified for a compressible liquid. The differential equations were discretized following the WENO shock capturing scheme in a prolate spheroidal and cylindrical coordinate systems. Details were also presented regarding the derivation and implementation of the non-reflective, reflective and symmetry boundary conditions.

Numerical simulations with a value of the order of 20 bubbles/cm^3 for the bubble number density and bubble nuclei size of approximately 20 μm presented the closest match with empirical observations in terms of the growth, dimensions and lifetime of the bubble cloud in the focal region of a free-field Caltech-EHL. This value of nuclei density is less than values estimated from high-speed pictures (anywhere between 30 and 70 bubbles/cm^3). However, the bubble counting procedure is highly subjective and may account for the discrepancy with the numerical predictions.

The pressure history predicted by the numerical model at the focal point of the lithotripter fell within the range of expected experimental measurements at the same location. However, due to expected limitations in the WENO shock capturing scheme, the numerical representation of the shock front is smeared over several grid points unlike the sharp pressure rise seen from measurements. Moreover, cases with low bubble number density were found to be in a closer agreement with observations than cases with higher void fraction. This conclusion was not surprising since it was noted that such measurements are typically obtained with clean degassed water with a minimal number of shock waves.

Using the present numerical model, we were able to discern a new mechanism for the generation of

tensile stress behind the reflected shock wave. The numerical results showed the growth of a region of negative pressure behind the reflected wave which is attributed to the finite thickness of the wave and the curvature mismatch between the initial spherical wave and the ellipsoidal reflector. To our knowledge, previous analyses were based on acoustic approach (high frequency limit or infinitely thin wave) and thus have not reported this mechanism.

For the purpose of calibration and validation of the simulation parameters, the size, shape and duration of predicted bubble clouds were compared to high-speed images of a free-field lithotripter. The closest comparisons were obtained with the initial bubble field set to 20 bubbles/cm^3 and bubble nuclei radius within the range of 10 to 30 μm. Further validation of the model was obtained by comparing numerical and experimental results for the dual-pulse lithotripter configuration. The banded structure of the bubble cloud initially observed in experiments was evident in the simulations conducted using the present model. Since theoretical and numerical analyses based on a decoupled approach were unable to predict this banded structure, we can infer that the growth of bubbles in the prefocal region is due to the coupling interaction between the bubble and liquid phase. Some discrepancies in the width of the band of reduced cavitation activity were observed and attributed to the limited capability of the numerical model to represent bubble cloud interactions for void fractions as high as those observed in the focal region.

Using the energy balance derived from the Herring bubble model, the energy stored and released by a bubble was computed for the bubble cloud simulations presented in this study. The energy lost by a bubble during its violent collapse was then used as a surrogate for the its potential to inflict damage.

In an additional post-processing step, the amount of non-condensible gas transfer in and out of the bubble was estimated using a one-dimensional model for the gas diffusion in the liquid and an approximate model for the behavior of the gas mixture inside the bubble. From these results, we were able to estimate the growth of a bubble nuclei due to gas trapping as well as the amount of time needed for the nuclei to dissolve back to its initial size. Given this period, the simulation parameter established *a priori* can be related to a value of the pulse rate frequency.

Using the coupled two-phase flow model, interactions within the bubble cloud were studied. During the bubble growth phase, the pressure at the center of the bubble cloud decreased slightly below the ambient pressure for cases with non-zero void fraction. This effect is a result of the flow field generated by the expanding bubbles within the cloud. Because of this interaction between the bubble cloud and the pressure field, bubbles in the center of the cloud can exhibit a much longer time to collapse than predicted given their maximum size and is observed in experiments.

During the collapse of the bubble cloud, the numerical model predicts an reverse interaction where the rapid decrease of void fraction causes fluid to rush towards the center of the bubble cloud and results in a rise in pressure. This increase in pressure, although smaller by two orders of magnitude than the initial shock wave, can results in up to a six fold increase in the bubble collapse energy release over cases where little or no cloud interactions are present.

Based on the values obtained for the energy released by a bubble collapse for cases covering a range of simulation parameters, conditions for optimal damage were identified. The damage potential was found to increase with the maximum void fraction. Although the maximum bubble size tends to grow with nuclei size, a high value of the initial void fraction results in shielding and smaller peak radius.

Using the present numerical model, optimal conditions for the bubble field were identified. As a first step in this process, the optimal initial bubble size given all other parameters fixed (bubble number density and initial shock wave parameters) was found. The same procedure was then carried out for different values of bubble number density. As expected, the optimum nuclei size decreases with increasing number density in order to avoid shielding. Additionally, the energy released by bubbles for the optimal case increased with the number density due to the increase in the interaction within the bubble cloud. When the optimal values of bubble nuclei were translated into equivalent pulse rate frequencies, the range of 1-1.2 Hz was found to be optimal for bubble number densities of 10 and 20 bubbles/cm^3. The values for the PRF were computed using a concentration of non-condensible gas equivalent to that obtained after degassing the liquid to 100 Torr.

4.2 Practical implications for lithotripsy

Based on the conclusions presented above, suggestions for practical improvements of lithotripsy can be stated. Past experimental work had anticipated the importance of the role of cloud cavitation in stone comminution. The present model emphasized this conjecture and suggests that collective interactions are driving force in stone comminution.

We have shown that a larger number of smaller bubbles produce a increase in the energy released during the bubble cloud collapse. This increased is counterbalanced by the shielding effect of higher void fraction mixture. Several practical suggestions to improve the amount of energy delivered by the bubble cloud can be derived from the above conclusions:

- low PRF should be maintained during the bulk of the treatment in order to maintain small bubble

nuclei,

- since for a fixed bubble nuclei there are no real benefits to increased shock level, the lithotripter should be operated at a lower intensity and slightly increased frequency,
- increasing the number of bubble nuclei present in the vicinity of the stone is crucial; this can be achieved by a high initial PRF and/or high intensity in order to promote large bubbles which can then split into a large number of smaller bubbles.

The actual conditions inside a patient undergoing a lithotripsy treatment are far from the simplified model presented in this work. However, the trends captured by our model are of practical importance and appeal for experimental verification.

4.3 Current limitations and future work

The present work opens a new avenue in the analysis of lithotripsy. The coupling between the two phases enabled the understanding of the inner workings of the bubble cloud in the focal region of a lithotripter. However, because of low order expansions in the derivation of the relevant equations, the accuracy of the present model decreases for void fractions greater than 5-10%. The inclusion of higher-order corrections in the averaged equations will improve the accuracy of the model for higher void fraction, but it should be noted that for the derivation shown in this work, a more limiting constraint is the lack of direct bubble–bubble interactions. Additionally, the differential equation representing the evolution of the bubble field assumed an uniform flow field in the neighborhood of the bubble which prohibits any shock wave–bubble interactions. Although appropriate corrections for these interactions have not been implemented in this work, we suspect that the introduction of direct bubble–bubble interactions would provide a greater improvement to the numerical model and should bring the numerical results for stone and dual-pulse cases in closer agreement with experimental observations.

The ability of the present work to provide a practical insight into the optimization of a lithotripsy treatment is limited on two fronts. First, empirical evidence suggests that under otherwise similar conditions, different treatment PRF can result in mark differences in the density of bubble nuclei in the focal region. This is most likely caused by bubbles fissioning during collapse. Since our present results show a strong dependence of the comminution potential to the bubble number density, bubble fission modeling will be needed before final conclusions regarding optimal treatment PRF can be made. A second limitation to the direct application of this work is the absence of an estimate for tissue damage. The introduction of a model

for kidney damage would allow to use of this numerical model to propose treatment parameters with minimal side effects to the patient.

Finally, since the results presented in this work have shown that the very modest pressure increase within the collapsing bubble cloud can significantly increase the damage potential of bubbles, it might be possible to increase it further by the use of an externally generated pressure wave. Although, this approach has been attempted experimentally by firing a second shock waves at the target with limited success, the use of the present model can be used to optimize the parameters of this secondary wave such as the time delay and intensity. Alternatively, the introduction of another wave source such as a piezoelectric device can be modeled using the approach presented in this work.

Appendix A

Compilation of simulation results

In Table A.3, all relevant data for the simulation of the free-field lithotripter based on the Caltech-EHL has been compiled. The following is an itemized descriptions of the type of entries:

Name:	name of simulation trial[1]
R_o:	equilibrium bubble radius
N:	initial bubble number density in bubbles per cm^3
P_{max}:	maximum pressure at focus
P_{min}:	minimum pressure at focus
Max void:	maximum void fraction at focus
R_{max}:	maximum bubble radius at focus[2]
E_{final}:	Energy in the bubble at its collapse (at focus) in μJ
t_c:	time to collapse for bubble at focus
PRF:	frequency in Hz of shock wave delivery such that the bubble nuclei size at the focal point returns has time to return to its original size between pulses
Energy:	energy contained in the initial spherical shock wave in mJ.

[1]The entries which match the closest the experimental evidence have been coded in yellow.
[2]Entries coded in green are within the range of empirical observations

Run name	$\mathbf{R}_o(\mu m)$	$\mathbf{N}_o$(bubbles/cm^3)	$\mathbf{P}_{\max}$ (MPa)	$\mathbf{P}_{\min}$ (MPa)	**Max void** (%)	$\mathbf{R}_{\max}$ (mm)	$\mathbf{E}_{\text{final}}(\mu J)$	$\mathbf{t}_c(\mu s)$	**PRF** (Hz)	**Energy** (mJ)
Run110a	5	0	27.44	-14.00	0.00	0.77	12.3	144	0.61	145
Run102g	15	0	27.44	-14.00	0.00	0.80	13.0	157	1.25	145
Run000v	20	0	27.44	-14.00	0.00	0.79	13.7	149	2.03	145
Run104a	50	0	27.44	-14.00	0.00	0.86	17.2	170	12.84	145
Run106a	80	0	27.44	-14.00	0.00	0.90	19.7	171	69.24	145
Run36a	10	5	27.30	-13.70	1.13	0.81	23.9	246	0.64	148
Run102e	15	5	27.21	-13.20	1.04	0.79	16.3	237	1.05	145
Run104b	50	5	25.74	-12.37	0.96	0.77	17.2	229	14.83	145
Run112a	1	10	27.30	-12.91	1.81	0.76	19.9	249	0.42	145
Run112b	3	10	27.39	-13.34	1.83	0.76	20.0	251	0.45	145
Run110b	5	10	27.27	-13.00	1.89	0.77	21.1	254	0.49	145
Run112c	7	10	27.26	-13.31	1.88	0.77	20.7	256	0.57	145
Run112d	10	10	27.19	-12.98	1.97	0.78	22.1	260	0.70	145
Run112e	15	10	27.16	-13.02	2.03	0.79	23.1	264	1.02	145
Run112f	20	10	27.10	-12.86	2.11	0.80	24.5	267	1.46	145
Run112g	25	10	26.84	-12.86	2.13	0.80	25.0	268	2.07	145
Run112h	30	10	26.48	-12.83	2.05	0.79	24.8	266	3.06	145
Run112i	35	10	26.14	-12.39	1.99	0.78	24.9	261	4.63	145
Run112j	40	10	25.64	-11.82	1.77	0.75	22.7	249	7.42	145
Run112k	45	10	24.96	-11.82	1.66	0.74	21.6	236	11.81	145
Run104c-ext	50	10	24.71	-11.76	1.40	0.69	18.4	220	22.87	146
Run106b	80	10	23.45	-9.04	0.75	0.56	17.9	138	373.28	149
Run102f	15	15	27.10	-12.80	3.46	0.82	29.0	308	0.88	145
Run104d-ext	50	15	23.76	-10.67	1.68	0.64	19.2	213	31.04	146
Run113a	1	20	27.23	-12.66	4.42	0.81	31.3	301	0.37	145
Run113b	3	20	27.31	-12.57	4.61	0.82	33.6	306	0.39	145
Run113c	5	20	27.29	-12.67	4.54	0.82	32.2	307	0.43	145
Run113d	7	20	27.26	-12.43	4.85	0.83	35.2	312	0.47	145
Run113e	9	20	27.28	-12.46	4.83	0.83	35.1	314	0.55	145
Run113f	11	20	27.09	-12.63	4.55	0.82	30.5	313	0.67	145
Run113g	14	20	27.10	-12.29	4.97	0.84	36.2	318	0.78	145
Run113h	17	20	26.99	-12.26	4.99	0.84	36.9	318	0.98	145
Run000a	20	20	26.96	-12.41	5.37	0.86	40.8	321	1.15	145
Run105c	25	20	26.47	-12.39	5.12	0.85	37.3	331	1.62	145
Run105d	30	20	25.84	-12.17	4.34	0.80	32.6	315	2.73	145
Run105e	35	20	25.44	-11.49	3.73	0.76	30.1	294	4.66	146
Run105f	40	20	24.29	-11.07	2.81	0.70	23.5	263	9.46	146
Run105g	45	20	23.24	-10.25	2.37	0.66	19.4	232	16.78	146
Run104e-ext	50	20	22.52	-9.17	1.82	0.60	18.5	200	47.66	147
Run106c	80	20	17.30	-8.45	0.34	0.34	4.6	125	500.85	153
Run102h	15	25	26.93	-12.38	7.65	0.90	44.1	367	0.70	145
Run104f-ext	50	25	21.11	-7.59	2.13	0.59	19.9	190	50.85	147
Run110d	5	30	27.37	-12.21	9.79	0.92	52.7	370	0.34	145
Run106d	80	30	18.63	-8.53	0.28	0.28	3.6	125	494.62	158
Run106e	80	40	17.69	-8.69	0.22	0.24	2.5	125	491.49	162

Table A.3: Compilation of simulation result for free-field lithotripter based on the Caltech-EHL.

Run name	$\mathbf{R}_o(\mu m)$	$\mathbf{N}_o$(bubbles/cm^3)	$\mathbf{P}_{\max}$ (MPa)	$\mathbf{P}_{\min}$ (MPa)	**Max void** (%)	$\mathbf{R}_{\max}$ (mm)	$\mathbf{E}_{\text{final}}(\mu J)$	$\mathbf{t}_c(\mu s)$	**PRF** (Hz)	**Energy** (mJ)
Run100a	5	20	23.81	-18.20	7.89	0.98	41.9	297	0.35	131
Run100b	10	20	23.87	-18.98	8.66	1.01	47.3	306	0.45	131
Run100c	15	20	24.34	-18.14	9.12	1.03	50.4	312	0.60	131
Run100e	25	20	25.33	-17.76	9.74	1.05	54.3	315	1.08	131
Run100f	30	20	25.85	-17.14	11.61	1.12	65.8	323	1.23	131
Run100g	35	20	25.21	-19.42	10.44	1.08	62.7	305	1.89	131
Run100h	40	20	22.67	-19.50	7.39	0.96	39.7	268	4.13	131
Run100i	45	20	19.11	-18.83	6.82	0.93	37.5	247	6.37	131
Run100j	50	20	17.70	-18.08	8.01	0.99	44.8	251	7.49	131
Run110b	10	0	23.77	-19.23	0	0.76	11.3	159	0.98	131
Run110d	20	0	23.77	-19.23	0	0.78	11.7	163	2.25	131
Run110f	30	0	23.77	-19.23	0	0.80	12.2	168	4.54	131
Run110h	40	0	23.77	-19.23	0	0.82	16.6	172	8.26	131
Run110j	50	0	23.77	-19.23	0	0.86	17.6	179	14.86	131

Table A.5: Compilation of simulation result for lithotripter with stone at focus.

Appendix B

Error estimation and model uncertainty

In addition to input parameters for the initial conditions, the implementation of the numerical model requires several parameters which are not based on physical properties. The following list presents some of the most relevant parameters related to the numerical implementation:

- spatial grid resolution,
- overall domain size,
- size of step in time integration,
- order of approximation in model for the ensemble averaged two-phase mixture,
- compressibility in shock capturing scheme.

In order to quantify the relative importance of these parameters, were each varied individually. Tables B.1, B.2 and B.3 present an impact assessment for the WENO compressibility, domain size and modeling accuracy.

As mentioned in Section 2.5, the artificial compression method (ACM) used to compensate for the excessive WENO dissipation requires an arbitrary model parameter. Table B.1 shows the impact of increasing the value of this parameter by a multiplicative factor. Results appeared somewhat better for the nominal value of compression however, increasing it by a factor of up to 2.5 times still generated acceptable results. It should be noted that increasing the value of the nominal compression by 3 times produced substantial spurious oscillations. Since the value of artificial compression is an arbitrary parameter, fluctuations caused by changes in its value thus provide a measure of error/uncertainty in the numerical implementation.

Result	**Run000a**	**Run111a**	**Run111b**	**Run111c**	**Run111d**	Average	Std. Dev. (%)
Compression	x1.0	x2.0	x1.5	x2.5	x3.0		
$P_{\max}(MPa)$	26.96	26.85	27.03	26.89	27.05	26.96	**0.29**
$P_{\min}(MPa)$	-12.41	-12.49	-12.33	-12.89	-13.19	-12.62	**2.72**
Max void (%)	5.37	5.16	5.07	5.14	4.99	5.27	**6.06**
$R_{\max}(mm)$	0.86	0.85	0.85	0.85	0.84	0.86	**1.99**
$E_{\text{collapse}}(\mu J)$	40.8	38.8	38.2	39.3	38.2	39.8	**5.07**
$t_c(\mu s)$	321	320	319	320	319	323	**2.68**
PRF (Hz)	1.15	1.19	1.21	1.20	1.23	1.17	**6.23**

Table B.1: Impact of artificial compression parameter in WENO on selected numerical results.

The presence of non-reflective boundary condition can become a source of error because of approximations in its numerical implementation but also if it truncates important features within the domain of interest. During the course of this work, several preliminary cases involved shorter domain to facilitate computation. It was later found that the domain boundary truncated the bubble cloud and impacted the results. Table B.2 provides a summary of comparison between the long and short domain versions of selected cases. Although the final results presented here were computed strictly with the longer domain, this analysis provides a measure of the potential impact of placement and implementation of the non-reflective boundary.

	Domain size	$P_{\max}(MPa)$	$P_{\min}(MPa)$	Max void (%)	$R_{\max}(mm)$	$E_{\text{collapse}}(\mu J)$	$t_c(\mu s)$	PRF (Hz)
Run000	long	26.96	-12.41	5.37	0.86	40.8	321	1.15
Run105b	short	26.96	-12.41	5.86	0.89	43.4	341	1.03
Std. Dev.(%)		0.00	0.00	9.12	3.49	6.37	6.23	10.40
Run104c-ext	long	24.71	-11.76	1.40	0.69	18.4	220	22.87
Run104c	short	24.71	-11.77	1.46	0.70	16.8	230	20.97
Std. Dev.(%)		0.00	0.09	2.86	1.45	8.70	4.55	8.31
Run104d-ext	long	23.76	-10.67	1.68	0.64	19.2	213	31.04
Run104d	short	23.76	-10.67	1.76	0.65	17.5	222	29.23
Std. Dev.(%)		0.00	0.00	4.76	1.56	8.85	4.23	5.83
Run104e-ext	long	22.52	-9.17	1.82	0.60	18.5	200	47.66
Run104e	short	22.52	-9.17	1.89	0.61	17.8	208	43.48
Std. Dev.(%)		0.00	0.00	3.85	1.67	3.78	4.00	8.77
Run104f-ext	long	22.11	-7.59	2.13	0.59	19.9	190	50.85
Run104f	short	22.11	-7.60	2.20	0.60	18.7	196	46.65
Std. Dev.(%)		0.00	0.13	3.29	1.69	6.03	3.16	8.26
Average (%)		**0.00**	**0.04**	**4.74**	**1.97**	**6.75**	**4.43**	**8.31**

Table B.2: Impact of size of domain on selected numerical results.

As presented in Section 2.2, the mixture momentum equation 2.28 has a contribution of order β_D. To assess the impact of the various contributions to this correction, the following simulations were conducted with their respective correction:

Run100: $\nabla\left[\beta_D p_C\right]$,

Run100b: $\nabla\left[\beta_D(p_C - \dot{\bar{R}}^2)\right]$,

Run100c: $\nabla\left[\beta_D(p_C - p_B(\bar{R}) - \dot{\bar{R}}^2)\right]$.

A comparison of the results is presented in Table B.3. It should be noted that the impact of the correction term is significantly less than the error introduced by the WENO compression or the truncation of the domain.

	$P_{\max}(MPa)$	$P_{\min}(MPa)$	Max void (%)	$R_{\max}(mm)$	$E_{\text{collapse}}(\mu J)$	$t_c(\mu s)$	PRF (Hz)
Run100	27.28	-12.55	3.31	0.93	49.9	335	0.63
Run100b	27.28	-12.56	3.28	0.92	50.0	335	0.64
Run100c	27.25	-12.65	3.25	0.92	48.4	335	0.64
Std. Dev.(%)	**0.06**	**0.44**	**0.96**	**0.33**	**1.81**	**0.00**	**0.91**

Table B.3: Impact of β_D modeling correction on selected numerical results.

Since an appropriate domain size and modeling corrections were used in the cases presented here, the errors presented in Table B.2 and B.3 represent measures of sensitivity of the results to a potentially poor numerical implementation and should not be considered as error estimates.

For the present work, the choice of the compression parameter is arbitrary, hence the data shown in Table B.1 provide a measure of the range of *a priori* equally valid results. Since the appropriate value for this parameter cannot be determined from first principle, the simulation results are obtained with a measure of uncertainty.

Appendix C

Derivation of the ensemble averaged equations

C.1 Ensemble phase averaging

In this work the liquid phase is assumed to be inviscid and compressible and its behavior can be described by the compressible Euler equations:

$$\frac{\partial \rho}{\partial t} + \nabla \cdot (\rho \mathbf{u}) = 0, \tag{C.1}$$

$$\frac{\partial \rho \mathbf{u}}{\partial t} + \nabla \cdot (\rho \mathbf{u}\mathbf{u}) + \nabla p = 0, \tag{C.2}$$

where

ρ is the liquid density

$\mathbf{u}$ is the liquid velocity

p is the liquid pressure

The Tait equation of state for water is used to close the above set of equations:

$$\frac{p + B}{p_o + B} = \left(\frac{\rho}{\rho_o}\right)^{\alpha}, \tag{C.3}$$

where

$$\alpha = 7.15,$$

$$B = p_o + \frac{\rho_o C^2}{\alpha},$$

and C is the speed of sound in pure liquid and is taken to be 1500 m/s.

The procedure for deriving the relevant dynamical equations is identical to the one presented in the work of Zhang & Prosperetti (1994). In this case however, the liquid phase is taken to be compressible. The final equations therefore differ slightly from the ones found in Zhang & Prosperetti (1994).

C.1.1 Preliminaries

In what follows the subscript $_C$ stands for the continuum phase. The ensemble average of an arbitrary quantity f is defined in the continuous phase by

$$\langle f_C \rangle (\mathbf{x}) = \frac{1}{\beta_C N!} \int d\mathcal{C}^N \mathcal{P}(N,t) \chi_C(\mathbf{x};N) f(\mathbf{x},t|N), \tag{C.4}$$

where

$$\begin{aligned} \int d\mathcal{C}^N &\equiv \int d\mathbf{y}^N dR^N dR_o^N d\mathbf{w}^N d\dot{R}^N \\ &\equiv \int d\mathbf{y}_1 dR_1 dR_{o1} d\mathbf{w}_1 d\dot{R}_1 \int d\mathbf{y}_2 dR_2 dR_{o2} d\mathbf{w}_2 d\dot{R}_2 \\ &\quad \ldots \int d\mathbf{y}_N dR_N dR_{oN} d\mathbf{w}_N d\dot{R}_N, \end{aligned}$$

$f_C(\mathbf{x},t\|N)$	is the value of function f_C at location $\mathbf{x}$ and time t given the configuration of N bubbles
$f_C(\mathbf{x},t\|\mathbf{y},R,R_o,\mathbf{w},\dot{R})$	is the value of function f_C at location $\mathbf{x}$ and time t given the presence of a bubble of state $(R,R_o,\mathbf{w},\dot{R})$ located at $\mathbf{y}$
$\mathbf{y}_i$	is the location of the ith bubble
R_i	is the radius of the ith bubble
R_{oi}	is the equilibrium radius of the ith bubble
$\mathbf{w}_i$	is the translational velocity of the ith bubble
$\dot{R}_i$	is the radial velocity of the ith bubble

Additionally, we define an indicator function:

$$\chi_C(\mathbf{x};N) = \begin{cases} 1 & \text{if } |\mathbf{x}-\mathbf{y}| > R_i \text{ for all } i, \\ 0 & \text{otherwise,} \end{cases}$$

such that the following

$$\beta_C = \frac{1}{N!}\int d\mathcal{C}^N \mathcal{P}(N,t)\chi_C(\mathbf{x};N).$$

is the fraction of volume occupied by liquid in the continuum phase.

The function $\mathcal{P}(N,t)$ is the probability of finding N bubbles in a given state. The number of bubbles present in the mixture is assumed to remain constant, which is consistent with the assumption that bubbles remain spherical. Given the additional assumptions detailed in Section C.1.4, the bubble model can be reduced to three state variables R,R_o and $\dot{R}$.

Since bubbles are neither created nor destroyed, the probability is conserved.

$$\frac{\partial \mathcal{P}}{\partial t} + \sum_{i=1}^{N} \frac{\partial}{\partial \mathbf{x}_i}(\mathbf{w}_i\mathcal{P}) + \frac{\partial}{\partial \mathbf{w}_i}(\dot{\mathbf{w}}_i\mathcal{P}) + \frac{\partial}{\partial R_i}(\dot{R}_i\mathcal{P}) + \frac{\partial}{\partial \dot{R}_i}(\ddot{R}_i\mathcal{P}) + \frac{\partial}{\partial R_{oi}}(\dot{R}_{oi}\mathcal{P}) = 0 \tag{C.5}$$

For negligible gas diffusion into the bubble (see Section C.1.4), the last term in the above equation can be neglected.

$$\frac{\partial \mathcal{P}}{\partial t} + \sum_{i=1}^{N} \frac{\partial}{\partial \mathbf{x}_i}(\mathbf{w}_i\mathcal{P}) + \frac{\partial}{\partial \mathbf{w}_i}(\dot{\mathbf{w}}_i\mathcal{P}) + \frac{\partial}{\partial R_i}(\dot{R}_i\mathcal{P}) + \frac{\partial}{\partial \dot{R}_i}(\ddot{R}_i\mathcal{P}) = 0 \tag{C.6}$$

The probability of finding a bubble at location $\mathbf{x}$ and in state $(R, R_o, \mathbf{w}, \dot{R}, t)$ is found by integrating over all the possible states of the other $N-1$ bubbles:

$$\mathcal{P}(\mathbf{x}, R, R_o, \mathbf{w}, \dot{R}, t) = \int d\mathcal{C}^{N-1}\mathcal{P}(N,t), \tag{C.7}$$

and consequently, we can write

$$\frac{\partial \mathcal{P}}{\partial t}(\mathbf{x}, R, R_o, \mathbf{w}, \dot{R}, t) = \int d\mathcal{C}^{N-1}\frac{\partial \mathcal{P}}{\partial t}(N,t). \tag{C.8}$$

Replacing the time derivative at the probability field by equation C.6, we can write

$$\frac{\partial \mathcal{P}}{\partial t}(\mathbf{x}, R, R_o, \mathbf{w}, \dot{R}, t) = -\sum_{i=1}^{N}\int d\mathcal{C}^{N-1}\frac{\partial}{\partial \mathbf{x}_i}(\mathbf{w}_i\mathcal{P}) + \frac{\partial}{\partial \mathbf{w}_i}(\dot{\mathbf{w}}_i\mathcal{P}) + \frac{\partial}{\partial R_i}(\dot{R}_i\mathcal{P}) + \frac{\partial}{\partial \dot{R}_i}(\ddot{R}_i\mathcal{P}). \tag{C.9}$$

Integrating by parts and using expression C.7 for the probability of finding a bubble, we can simplify the

above expression to:

$$\frac{\partial \mathcal{P}}{\partial t}(\mathbf{x}, R, \mathbf{w}, \dot{R}, t) = -\left[\frac{\partial}{\partial \mathbf{x}}\mathbf{w} + \frac{\partial}{\partial \mathbf{w}}\dot{\mathbf{w}} + \frac{\partial}{\partial R}\dot{R} + \frac{\partial}{\partial \dot{R}}\ddot{R}\right] \int d\mathcal{C}^{N-1}\mathcal{P}(N,t),$$
$$= -\left[\frac{\partial}{\partial \mathbf{x}}\mathbf{w} + \frac{\partial}{\partial \mathbf{w}}\dot{\mathbf{w}} + \frac{\partial}{\partial R}\dot{R} + \frac{\partial}{\partial \dot{R}}\ddot{R}\right] \mathcal{P}(\mathbf{x}, R, R_o, \mathbf{w}, \dot{R}, t). \tag{C.10}$$

The bubble number density is defined as

$$N(\mathbf{x}, t) = \int dR dR_o d\dot{R} d\mathbf{w} \mathcal{P}(\mathbf{x}, R, R_o, \mathbf{w}, \dot{R}, t). \tag{C.11}$$

Using the above definition and the equation C.6, we can write a bubble number density conservation equation:

$$\frac{\partial N}{\partial t}(\mathbf{x}, t) = \int dR dR_o d\dot{R} d\mathbf{w} \frac{\partial \mathcal{P}}{\partial t}(\mathbf{x}, R, R_o, \mathbf{w}, \dot{R}, t),$$
$$= -\frac{\partial}{\partial \mathbf{x}}(\mathbf{w}N) \tag{C.12}$$

The time derivatives of an averaged quantity is essential in the formulation of averaged governing equations. Starting from the definition of the ensemble phase average, we can write

$$\frac{\partial}{\partial t}\left(\beta_C \left\langle f_C \right\rangle (\mathbf{x}, t)\right) = \frac{1}{N!}\int d\mathbf{y}^N dR^N dR_o^N d\mathbf{w}^N d\dot{R}^N \frac{\partial}{\partial t}\left[\mathcal{P}(N,t)\chi_C(\mathbf{x}; N) f_C(\mathbf{x}, t|N)\right]. \tag{C.13}$$

Using the chain rule and the probability conservation equation C.6, we can expand equation C.13:

$$\begin{aligned}
\frac{\partial}{\partial t}\left(\beta_C \left\langle f_C \right\rangle (\mathbf{x}, t)\right) = & \\
& \frac{1}{N!}\int d\mathbf{y}^N dR^N dR_o^N d\mathbf{w}^N d\dot{R}^N \frac{\partial}{\partial t}(\mathcal{P}(N,t))\chi_C(\mathbf{x}; N) f_C(\mathbf{x}, t|N) \\
& + \frac{1}{N!}\int d\mathbf{y}^N dR^N dR_o^N d\mathbf{w}^N d\dot{R}^N \chi_C(\mathbf{x}; N)\frac{\partial}{\partial t}\left(f_C(\mathbf{x}, t|N)\right), \\
= & -\frac{1}{N!}\int d\mathbf{y}^N dR^N dR_o^N d\mathbf{w}^N d\dot{R}^N \chi_C(\mathbf{x}; N) f_C(\mathbf{x}, t|N) \\
& \sum_{i=1}^{N}\left[\frac{\partial}{\partial \mathbf{y}_i}(\mathbf{w}_i\mathcal{P}) + \frac{\partial}{\partial \mathbf{w}_i}(\dot{\mathbf{w}}_i\mathcal{P}) + \frac{\partial}{\partial R_i}(\dot{R}_i\mathcal{P}) + \frac{\partial}{\partial \dot{R}_i}(\ddot{R}_i\mathcal{P})\right] \\
& + \frac{1}{N!}\int d\mathbf{y}^N dR^N dR_o^N d\mathbf{w}^N d\dot{R}^N \chi_C(\mathbf{x}; N)\frac{\partial}{\partial t}\left(f_C(\mathbf{x}, t|N)\right).
\end{aligned} \tag{C.14}$$

Using integration by parts on the first integral, we obtain

$$\begin{aligned}\frac{\partial}{\partial t}\left(\beta_C\left\langle f_C\right\rangle(\mathbf{x},t)\right) = \\ &\frac{1}{N!}\int d\mathbf{y}^N dR^N dR_o^N d\mathbf{w}^N d\dot{R}^N \mathcal{P}\sum_{i=1}^{N}\Big[\mathbf{w}_i\frac{\partial}{\partial \mathbf{y}_i}(\chi_C f_C)+\dot{\mathbf{w}}_i\frac{\partial}{\partial \mathbf{w}_i}(\chi_C f_C) \\ &+\dot{R}\frac{\partial}{\partial R}(\chi_C f_C)+\ddot{R}\frac{\partial}{\partial \dot{R}}(\chi_C f_C)\Big] \\ &+\frac{1}{N!}\int d\mathbf{y}^N dR^N dR_o^N d\mathbf{w}^N d\dot{R}^N \chi_C(\mathbf{x};N)\frac{\partial}{\partial t}\left(f_C(\mathbf{x},t|N)\right).\end{aligned} \tag{C.15}$$

Expanding and combining the f_C derivatives in C.15, we obtain

$$\begin{aligned}\frac{\partial}{\partial t}\left(\beta_C\left\langle f_C\right\rangle(\mathbf{x},t)\right) = \frac{1}{N!}\int d\mathbf{y}^N dR^N dR_o^N d\mathbf{w}^N d\dot{R}^N \mathcal{P}\sum_{i=1}^{N}\Big[\mathbf{w}_i\frac{\partial}{\partial \mathbf{y}_i}(\chi_C f_C)+\dot{\mathbf{w}}_i\frac{\partial}{\partial \mathbf{w}_i}(\chi_C f_C) \\ +\dot{R}_i\frac{\partial}{\partial R_i}(\chi_C f_C)+\ddot{R}_i\frac{\partial}{\partial \dot{R}_i}(\chi_C f_C)\Big]+\frac{1}{N!}\int d\mathbf{y}^N dR^N d\mathbf{w}^N d\dot{R}^N \chi_C(\mathbf{x};N)\frac{\partial}{\partial t}\left(f_C(\mathbf{x},t|N)\right),\end{aligned} \tag{C.16}$$

which can be expressed in terms of the ensemble average operator as

$$\begin{aligned}\frac{\partial}{\partial t}\left(\beta_C\left\langle f_C\right\rangle(\mathbf{x},t)\right) = \\ &\left\langle\frac{\partial f_C}{\partial t}+\sum_{i=1}^{N}\mathbf{w}_i\frac{\partial f_C}{\partial \mathbf{y}_i}+\dot{\mathbf{w}}_i\frac{\partial f_C}{\partial \mathbf{w}_i}+\dot{R}_i\frac{\partial f_C}{\partial R_i}+\ddot{R}_i\frac{\partial f_C}{\partial \dot{R}_i}\right\rangle \\ &+\frac{1}{N!}\int d\mathbf{y}^N dR^N dR_o^N d\mathbf{w}^N d\dot{R}^N \mathcal{P} f_C\sum_{i=1}^{N}\left[\mathbf{w}_i\frac{\partial \chi_C}{\partial \mathbf{y}_i}+\dot{R}_i\frac{\partial \chi_C}{\partial R_i}\right].\end{aligned} \tag{C.17}$$

Using the definition of the indicator function χ_C, the last integral in the above expression can be simplified to a surface integral:

$$\begin{aligned}\frac{\partial}{\partial t}\left(\beta_C\left\langle f_C\right\rangle(\mathbf{x},t)\right) = \left\langle\frac{\partial f_C}{\partial t}+\sum_{i=1}^{N}\mathbf{w}_i\frac{\partial f_C}{\partial \mathbf{y}_i}+\dot{\mathbf{w}}_i\frac{\partial f_C}{\partial \mathbf{w}_i}+\dot{R}_i\frac{\partial f_C}{\partial R_i}+\ddot{R}_i\frac{\partial f_C}{\partial \dot{R}_i}\right\rangle \\ -\int dR dR_o d\mathbf{w} d\dot{R}\int_{|\mathbf{y}-\mathbf{x}|=R} dS_y \mathcal{P}(\mathbf{y},R,R_o,\mathbf{w},\dot{R},t) f_C(\mathbf{x},t|\mathbf{y},R,R_o,\mathbf{w},\dot{R})(\mathbf{n}\cdot\mathbf{w}+\dot{R}).\end{aligned} \tag{C.18}$$

The first term on the right hand side of equation C.18 is the averaged time derivative. This term includes contributions from both the explicit time derivative of f_C and the fluctuations caused by the changing bubble field. The time derivative of the solution for a particular bubble configuration normally accounts for both

direct and indirect effects. Therefore, we can rewrite equation C.18 as

$$\begin{aligned}\frac{\partial}{\partial t}\left(\beta_C \left\langle f_C \right\rangle (\mathbf{x},t)\right) &= \left\langle \frac{\partial f_C}{\partial t} \right\rangle \\ &- \int dR dR_o d\mathbf{w} d\dot{R} \int_{|\mathbf{y}-\mathbf{x}|=R} dS_y \mathcal{P}(\mathbf{y}, R, R_o, \mathbf{w}, \dot{R}, t) f_C(\mathbf{x}, t|\mathbf{y}, R, R_o, \mathbf{w}, \dot{R})(\mathbf{n}\cdot\mathbf{w} + \dot{R}).\end{aligned} \tag{C.19}$$

The spatial derivatives are derived in a similar fashion starting from the definition of the average:

$$\nabla(\beta_C \left\langle f_C \right\rangle)(\mathbf{x},t) = \frac{1}{N!}\int d\mathbf{y}^N dR^N dR_o^N d\mathbf{w}^N d\dot{R}^N \mathcal{P}(N,t) \nabla\left[\chi_C(\mathbf{x};N) f_C(\mathbf{x},t|N)\right]. \tag{C.20}$$

Applying the chain rule on the above expression, we obtain

$$\begin{aligned}\nabla(\beta_C \left\langle f_C \right\rangle)(\mathbf{x},t) = \frac{1}{N!}\int d\mathbf{y}^N dR^N dR_o^N d\mathbf{w}^N d\dot{R}^N \mathcal{P}(N,t) \chi_C(\mathbf{x};N) \nabla f_C(\mathbf{x},t|N) \\ + \frac{1}{N!}\int d\mathbf{y}^N dR^N dR_o^N d\mathbf{w}^N d\dot{R}^N \mathcal{P}(N,t) f_C(\mathbf{x};N) \nabla \chi_C(\mathbf{x},t|N).\end{aligned} \tag{C.21}$$

Using the definition of the indicator function χ_C, the gradient of the ensemble average of a quantity is

$$\begin{aligned}\nabla(\beta_C \left\langle f_C \right\rangle)(\mathbf{x},t) &= \beta_C \left\langle \nabla f_C \right\rangle \\ &- \int dR dR_o d\mathbf{w} d\dot{R} \int_{|\mathbf{y}-\mathbf{x}|=R} dS_y \mathcal{P}(\mathbf{y}, R, R_o, \mathbf{w}, \dot{R}, t) f_C(\mathbf{x}, t|\mathbf{y}, R, R_o, \mathbf{w}, \dot{R})\mathbf{n}.\end{aligned} \tag{C.22}$$

Combining expression C.19 and C.22, we can write the following result:

$$\begin{aligned}\frac{\partial}{\partial t}\left(\beta_C \left\langle f_C \right\rangle\right) + \nabla\cdot\left(\beta_C \left\langle f_C \mathbf{u} \right\rangle\right) &= \beta_C \left\langle \frac{\partial f_C}{\partial t} + \nabla\cdot(f_C\mathbf{u}) \right\rangle \\ + \int dR dR_o d\mathbf{w} d\dot{R} \int_{|\mathbf{y}-\mathbf{x}|=R} dS_y \mathcal{P}(\mathbf{y}, R, R_o, \mathbf{w}, \dot{R}, t) f_C(\mathbf{x}, t|\mathbf{y}, R, R_o, \mathbf{w}, \dot{R})(\mathbf{w}\cdot\mathbf{n} + \dot{R} - \mathbf{u}\cdot\mathbf{n}).\end{aligned} \tag{C.23}$$

Based on the assumption that bubbles are assumed to remain spherical at all times, the boundary condition for the flow field at the surface of a bubble is

$$\mathbf{u}\cdot\mathbf{n} = \mathbf{w}\cdot\mathbf{n} + \dot{R}. \tag{C.24}$$

Therefore, equation C.23 can be simplified to

$$\frac{\partial}{\partial t}\left(\beta_C \left\langle f_C \right\rangle\right) + \nabla\cdot\left(\beta_C \left\langle f_C \mathbf{u} \right\rangle\right) = \beta_C \left\langle \frac{\partial f_C}{\partial t} + \nabla\cdot(f_C\mathbf{u}) \right\rangle. \tag{C.25}$$

Another important relation regarding the ensemble averaging is based on the assumption that the probability density and average properties vary slowly in space so that the probability $\mathcal{P}(\mathbf{y},...)$ can be expanded in a power series about the point $\mathbf{x}$.

$$\mathcal{P}(\mathbf{y},R,R_o,\mathbf{w},\dot{R},t) \approx \mathcal{P}(\mathbf{x},R,R_o,\mathbf{w},\dot{R},t) + (\mathbf{y}-\mathbf{x})\cdot\nabla_{\mathbf{x}}\mathcal{P}(\mathbf{x},R,R_o,\mathbf{w},\dot{R},t). \tag{C.26}$$

Defining the relative position $\mathbf{s} = \mathbf{x} - \mathbf{y}$, we can write

$$\begin{aligned}&\int_{|\mathbf{y}-\mathbf{x}|=R} dS_y \mathcal{P}(\mathbf{y},R,R_o,\mathbf{w},\dot{R},t) f_C(\mathbf{x},t|\mathbf{y},R,R_o,\mathbf{w},\dot{R}) \\ &\quad = \int_{|\mathbf{s}|=R} dS_s \mathcal{P}(\mathbf{x}-\mathbf{s},R,R_o,\mathbf{w},\dot{R},t) f_C(\mathbf{y}+\mathbf{s},t|\mathbf{y},R,R_o,\mathbf{w},\dot{R}). \qquad \text{(C.27)}\\ &\qquad\qquad\qquad\qquad\qquad\qquad\qquad\qquad\qquad\qquad\qquad\qquad\qquad\qquad\qquad\qquad\qquad\qquad \text{(C.28)}\end{aligned}$$

For bubble related fluctuations, the function f_C depends only on the relative position:

$$f_C(\mathbf{y}+\mathbf{s},t|\mathbf{y},R,R_o,\mathbf{w},\dot{R}) = f_C(\mathbf{s},t|R,R_o,\mathbf{w},\dot{R}). \tag{C.29}$$

The above integral can therefore be approximated by

$$\begin{aligned}&\int_{|\mathbf{y}-\mathbf{x}|=R} dS_y \mathcal{P}(\mathbf{y},R,R_o,\mathbf{w},\dot{R},t) f_C(\mathbf{x},t|\mathbf{y},R,R_o,\mathbf{w},\dot{R}) \\ &\quad \approx \int_{|\mathbf{s}|=R} dS_s \mathcal{P}(\mathbf{x},R,R_o,\mathbf{w},\dot{R},t) f_C(\mathbf{s},t|R,R_o,\mathbf{w},\dot{R}) \\ &\quad - \int_{|\mathbf{s}|=R} dS_s \mathbf{s}\cdot\nabla_{\mathbf{x}}\mathcal{P}(\mathbf{x},R,R_o,\mathbf{w},\dot{R},t) f_C(\mathbf{s},t|R,R_o,\mathbf{w},\dot{R}), \qquad \text{(C.30)}\end{aligned}$$

Another relevant relation is the second order approximation of the gradient operator:

$$\beta_D \nabla\langle f_C\rangle \approx \int dR dR_o d\dot{R} d\mathbf{w} \int_{|\mathbf{y}-\mathbf{x}|=R} dS_y \mathcal{P}(\mathbf{x},R,R_o,\mathbf{w},\dot{R},t)\mathbf{n} f_C(\mathbf{y},t). \tag{C.31}$$

C.1.2 Ensemble averaged Euler equations

The conservative variables for the average mixture are

$$\rho_M = \beta_C \rho_C + \beta_D \rho_D,$$
$$\rho_M \mathbf{u}_M = \beta_C \rho_C \mathbf{u}_C + \beta_D \rho_D \mathbf{u}_D.$$

However, since the disperse (vapor) phase is three orders of magnitude less dense than the continuous (liquid) phase, the mixture variables are well-approximated by

$$\rho_M \approx \beta_C \rho_C, \tag{C.32}$$
$$\rho_M \mathbf{u}_M \approx \beta_C \rho_C \mathbf{u}_C. \tag{C.33}$$

The conservation of mass for the average mixture is

$$\begin{aligned} \frac{\partial}{\partial t}\left(\beta_C \left\langle \rho_C \right\rangle\right) + \nabla \cdot \left(\beta_C \left\langle \rho_C \mathbf{u}_C \right\rangle\right) &= \beta_C \left\langle \frac{\partial \rho_C}{\partial t} + \nabla \cdot \left(\rho_C \mathbf{u}_C\right) \right\rangle, \\ &= 0. \end{aligned} \tag{C.34}$$

The momentum conservation for the average mixture is

$$\begin{aligned} \frac{\partial}{\partial t}\left(\beta_C \left\langle \rho_C \mathbf{u}_C \right\rangle\right) + \nabla \cdot \left(\beta_C \left\langle \rho_C \mathbf{u}_C \mathbf{u}_C \right\rangle\right) &= \beta_C \left\langle \frac{\partial \rho_C \mathbf{u}_C}{\partial t} + \nabla \cdot \left(\rho_C \mathbf{u}_C \mathbf{u}_C\right) \right\rangle, \\ &= -\beta_C \left\langle \nabla p_C \right\rangle. \end{aligned} \tag{C.35}$$

These equations need to be closed by expressing quantities such as $\langle \rho_C \mathbf{u}_C \rangle$, $\langle \rho_C \mathbf{u}_C \mathbf{u}_C \rangle$ and $\langle \nabla p_C \rangle$ in terms of $\langle \rho_C \rangle$, $\langle \mathbf{u}_C \rangle$ and average bubble properties. We first consider the average pressure gradient term. Since bubbles are effectively massless, the total force exerted on the bubble interface must be equal to zero.

$$\int dR dR_o d\dot{R} d\mathbf{w} \int_{|\mathbf{y}-\mathbf{x}|=R} dS_y \mathcal{P}(\mathbf{x}, R, R_o, \mathbf{w}, \dot{R}, t) \mathbf{n} p_C(\mathbf{y}, t|\mathbf{x}) = 0 \tag{C.36}$$

Furthermore, bubbles are assumed spherical and the pressure at the bubble interface is uniform and only a

function of the bubble radius.

$$\int dRdR_o d\dot{R}d\mathbf{w}\int_{|\mathbf{y}-\mathbf{x}|=R} dS_y\mathcal{P}(\mathbf{x},R,R_o,\mathbf{w},\dot{R},t)\mathbf{n}\mathbf{n}p_C(\mathbf{y},t|\mathbf{x}) = \int dRdR_o d\dot{R}d\mathbf{w}\int_{|\mathbf{y}-\mathbf{x}|=R} dS_y\mathcal{P}(\mathbf{x},R,R_o,\mathbf{w},\dot{R},t)\mathbf{n}\mathbf{n}p_B(R) = \beta_D\frac{\overline{R^3p_B(R)}}{\overline{R^3}}\mathbf{I}. \tag{C.37}$$

Using the above relations, we can write

$$\begin{aligned}
&\int dRdR_o d\dot{R}d\mathbf{w}\int_{|\mathbf{y}-\mathbf{x}|=R} dS_y\mathcal{P}(\mathbf{y},R,R_o,\mathbf{w},\dot{R},t)\mathbf{n}p_C(\mathbf{y},t|\mathbf{x})\\
&= \int dRdR_o d\dot{R}d\mathbf{w}\int_{|\mathbf{y}-\mathbf{x}|=R} dS_y\mathcal{P}(\mathbf{y},R,R_o,\mathbf{w},\dot{R},t)\mathbf{n}p_B(R,R_o),\\
&\approx \int dRdR_o d\dot{R}d\mathbf{w}\int_{|\mathbf{y}-\mathbf{x}|=R} dS_y\mathcal{P}(\mathbf{x},R,R_o,\mathbf{w},\dot{R},t)\mathbf{n}p_B(R,R_o) \quad (\to 0)\\
&-\nabla_{\mathbf{x}}\cdot\int dRdR_o d\dot{R}d\mathbf{w}\int_{|\mathbf{y}-\mathbf{x}|=R} dS_y\mathcal{P}(\mathbf{x},R,R_o,\mathbf{w},\dot{R},t)\mathbf{n}\mathbf{n}p_B(R,R_o),\\
&\approx -\nabla\left(\beta_D\frac{\overline{R^3p_B(R)}}{\overline{R^3}}\right),
\end{aligned} \tag{C.38}$$

consequently, using relations C.36 and C.37, we can simplify the above result to

$$\begin{aligned}
\beta_C\langle\nabla p_C\rangle &= \nabla(\beta_C\langle p_C\rangle) - \int dRdR_o d\dot{R}d\mathbf{w}\int_{|\mathbf{y}-\mathbf{x}|=R} dS_y\mathcal{P}(\mathbf{y},R,R_o,\mathbf{w},\dot{R},t)\mathbf{n}p_C(\mathbf{x},t|\mathbf{y}),\\
&\approx \nabla(\beta_C\langle p_C\rangle) - \int dRdR_o d\dot{R}d\mathbf{w}\int_{|\mathbf{y}-\mathbf{x}|=R} dS_y\mathcal{P}(\mathbf{x},R,R_o,\mathbf{w},\dot{R},t)\mathbf{n}p_B(R,R_o) \quad (\to 0)\\
&\qquad +\nabla\cdot\int dRdR_o d\dot{R}d\mathbf{w}\int_{|\mathbf{y}-\mathbf{x}|=R} dS_y\mathcal{P}(\mathbf{x},R,R_o,\mathbf{w},\dot{R},t)\mathbf{n}\mathbf{n}p_B(R,R_o),\\
&\approx \nabla\left(\beta_C\langle p_C\rangle + \beta_D\frac{\langle R^3p_B(R,R_o)\rangle}{\langle R^3\rangle}\right),
\end{aligned} \tag{C.39}$$

where $p_B(R)$ is the pressure in the liquid at the surface of a bubble located at $\mathbf{x}$ at time t. The momentum conservation equation for the mixture can thus be written as

$$\frac{\partial}{\partial t}\left(\langle\rho_M\mathbf{u}_M\rangle\right) + \nabla\cdot\left(\langle\rho_M\mathbf{u}_M\mathbf{u}_M\rangle\right) + \nabla\left(\beta_C\langle p_C\rangle + \beta_D\frac{\langle R^3p_B(R)\rangle}{\langle R^3\rangle}\right) = 0. \tag{C.40}$$

By rearranging terms, we obtain

$$\frac{\partial}{\partial t}\left(\langle\rho_M\mathbf{u}_M\rangle\right) + \nabla\cdot\left(\langle\rho_M\mathbf{u}_M\mathbf{u}_M\rangle\right) + \nabla\langle p_C\rangle = \nabla\left[\beta_D\left(\langle p_C\rangle - \frac{\langle R^3p_B(R)\rangle}{\langle R^3\rangle}\right)\right]. \tag{C.41}$$

Correlations such as $\langle \rho_M \mathbf{u}_M \rangle$ and $\langle \rho_M \mathbf{u}_M \mathbf{u}_M \rangle$ require a model for the flow field surrounding bubbles. For the purpose of this work, the flow field in the vicinity of the bubble was assumed to be incompressible and irrotational (see Section C.1.3 for more details). As a direct consequence, the density and velocity fluctuations are uncorrelated.

$$\langle \rho_M \mathbf{u}_M \rangle = \langle \rho_M \rangle \langle \mathbf{u}_M \rangle, \tag{C.42}$$

$$\langle \rho_M \mathbf{u}_M \mathbf{u}_M \rangle = \langle \rho_M \rangle \langle \mathbf{u}_M \mathbf{u}_M \rangle. \tag{C.43}$$

The velocity correlation can be expressed as a Reynolds stress term:

$$\begin{aligned} &\langle \mathbf{u}_M \mathbf{u}_M \rangle = \langle \mathbf{u}_M \rangle \langle \mathbf{u}_M \rangle \\ &- \int dR dR_o d\dot{R} d\mathbf{w} \int_{|\mathbf{y}-\mathbf{x}|>R} dS_y \mathcal{P}(\mathbf{y}, R, R_o, \mathbf{w}, \dot{R}, t)(\mathbf{u}_C(\mathbf{x}, t|\mathbf{y}) - \mathbf{u}_C(\mathbf{x}, t))(\mathbf{u}_C(\mathbf{x}, t|\mathbf{y}) - \mathbf{u}_C(\mathbf{x}, t)). \end{aligned} \tag{C.44}$$

Using an expansion of the above result about the point $\mathbf{x}$, we can write

$$\begin{aligned} &\langle \mathbf{u}_M \mathbf{u}_M \rangle - \langle \mathbf{u}_M \rangle \langle \mathbf{u}_M \rangle \\ &\quad \approx - \int dR dR_o d\dot{R} d\mathbf{w} \int_{|\mathbf{y}-\mathbf{x}|>R} dS_y \mathcal{P}(\mathbf{x}, R, R_o, \mathbf{w}, \dot{R}, t)(\mathbf{u}_C(\mathbf{y}, t|\mathbf{x}) - \mathbf{u}_C(\mathbf{y}, t))(\mathbf{u}_C(\mathbf{y}, t|\mathbf{x}) - \mathbf{u}_C(\mathbf{y}, t)) \\ &\quad + \nabla_{\mathbf{x}} \cdot \int dR dR_o d\dot{R} d\mathbf{w} \int_{|\mathbf{y}-\mathbf{x}|>R} dS_y (\mathbf{y}-\mathbf{x}) \mathcal{P}(\mathbf{x}, R, R_o, \mathbf{w}, \dot{R}, t) \\ &\qquad (\mathbf{u}_C(\mathbf{y}, t|\mathbf{x}) - \mathbf{u}_C(\mathbf{y}, t))(\mathbf{u}_C(\mathbf{y}, t|\mathbf{x}) - \mathbf{u}_C(\mathbf{y}, t)). \end{aligned} \tag{C.45}$$

Given that the flow field is incompressible and irrotational in the vicinity of the bubble, we can write the potential as (note that the subscript $_C$ for the continuous phase is dropped for simplicity)

$$\phi = -\frac{R^2 \dot{R}}{r} + \mathbf{u} \cdot \mathbf{s} + \frac{(\mathbf{u} - \mathbf{w}) \cdot \mathbf{s}}{2} \left(\frac{R}{r} \right)^3, \tag{C.46}$$

where $\mathbf{u}$ and $\mathbf{w}$ are the velocity of the liquid and bubble respectively. The relative position vector and magnitude are defined as $\mathbf{s} = \mathbf{y} - \mathbf{y}$ and $r = |\mathbf{s}|$. The velocity fluctuation due to the presence of a bubble at $\mathbf{x}$ is

$$\nabla \phi - \mathbf{u} = \frac{R^2 \dot{R}}{r^3} \mathbf{s} - \frac{3}{2} \mathbf{s} (\mathbf{u} - \mathbf{w}) \cdot \mathbf{s} \left(\frac{R^3}{r^5} \right) + \frac{1}{2} (\mathbf{u} - \mathbf{w}) \left(\frac{R^3}{r^3} \right). \tag{C.47}$$

Hence,

$$
\begin{aligned}
&\int_{|\mathbf{s}|>R} dV_s \left(\mathbf{u}(\mathbf{y}|\mathbf{x},R,R_o,\dot{R},\mathbf{w})-\mathbf{u}(\mathbf{y})\right)\left(\mathbf{u}(\mathbf{y}|\mathbf{x},R,R_o,\dot{R},\mathbf{w})-\mathbf{u}(\mathbf{y})\right)\\
&\qquad=\int_{|\mathbf{s}|>R} dV_s\left[\frac{R^2\dot{R}}{r^2}\mathbf{n}-\frac{3}{2}\mathbf{n}(\mathbf{u}-\mathbf{w})\cdot\mathbf{n}\left(\frac{R^3}{r^3}\right)+\frac{1}{2}(\mathbf{u}-\mathbf{w})\left(\frac{R^3}{r^3}\right)\right]\\
&\qquad\qquad\left[\frac{R^2\dot{R}}{r^2}\mathbf{n}-\frac{3}{2}\mathbf{n}(\mathbf{u}-\mathbf{w})\cdot\mathbf{n}\left(\frac{R^3}{r^3}\right)+\frac{1}{2}(\mathbf{u}-\mathbf{w})\left(\frac{R^3}{r^3}\right)\right],\\
&=\int_{|\mathbf{s}|>R} dV_s\frac{R^4\dot{R}^2}{r^4}\mathbf{nn}-3\frac{R^5\dot{R}}{r^5}\mathbf{nn}(\mathbf{u}-\mathbf{w})\cdot\mathbf{n}+\frac{R^5\dot{R}}{r^5}\mathbf{n}(\mathbf{u}-\mathbf{w})\\
&\quad+\frac{9}{4}\mathbf{nn}\left((\mathbf{u}-\mathbf{w})\cdot\mathbf{n}\right)^2\left(\frac{R^6}{r^6}\right)-\frac{3}{2}\mathbf{n}(\mathbf{u}-\mathbf{w})(\mathbf{u}-\mathbf{w})\cdot\mathbf{n}\left(\frac{R^6}{r^6}\right)+\frac{1}{4}(\mathbf{u}-\mathbf{w})(\mathbf{u}-\mathbf{w})\left(\frac{R^6}{r^6}\right),\\
&=\int_{|\mathbf{s}|=R} dS_s R^3\dot{R}^2\mathbf{nn}-\frac{3}{2}R^3\dot{R}\mathbf{nn}(\mathbf{u}-\mathbf{w})\cdot\mathbf{n}+\frac{1}{2}R^3\dot{R}\mathbf{n}(\mathbf{u}-\mathbf{w})\\
&\quad+\frac{3}{4}R^3\mathbf{nn}\left((\mathbf{u}-\mathbf{w})\cdot\mathbf{n}\right)^2-\frac{1}{2}R^3\mathbf{n}(\mathbf{u}-\mathbf{w})(\mathbf{u}-\mathbf{w})\cdot\mathbf{n}+\frac{1}{12}R^3(\mathbf{u}-\mathbf{w})(\mathbf{u}-\mathbf{w}),\\
&=\frac{4}{3}\pi R^3\dot{R}^2+\frac{3}{15}\pi R^3\left[\mathbf{I}(\mathbf{u}-\mathbf{w})\cdot(\mathbf{u}-\mathbf{w})+2(\mathbf{u}-\mathbf{w})(\mathbf{u}-\mathbf{w})\right]\\
&\qquad\qquad-\frac{2}{3}\pi R^3(\mathbf{u}-\mathbf{w})(\mathbf{u}-\mathbf{w})+\frac{1}{3}\pi R^3(\mathbf{u}-\mathbf{w})(\mathbf{u}-\mathbf{w}),\\
&=\frac{4}{3}\pi R^3\left[\dot{R}^2\mathbf{I}+\frac{3}{20}\mathbf{I}(\mathbf{u}-\mathbf{w})\cdot(\mathbf{u}-\mathbf{w})+\frac{1}{20}(\mathbf{u}-\mathbf{w})(\mathbf{u}-\mathbf{w})\right].
\end{aligned}
\tag{C.48}
$$

Similarly,

$$
\begin{aligned}
&\int_{|\mathbf{s}|>R} dV_s\mathbf{s}\left(\mathbf{u}(\mathbf{y}|\mathbf{x},R,R_o,\dot{R},\mathbf{w})-\mathbf{u}(\mathbf{y})\right)\left(\mathbf{u}(\mathbf{y}|\mathbf{x},R,R_o,\dot{R},\mathbf{w})-\mathbf{u}(\mathbf{y})\right)\\
&\qquad=\int_{|\mathbf{s}|>R} dV_s r\mathbf{n}\left[\frac{R^2\dot{R}}{r^2}\mathbf{n}-\frac{3}{2}\mathbf{n}(\mathbf{u}-\mathbf{w})\cdot\mathbf{n}\left(\frac{R^3}{r^3}\right)+\frac{1}{2}(\mathbf{u}-\mathbf{w})\left(\frac{R^3}{r^3}\right)\right]\\
&\qquad\qquad\left[\frac{R^2\dot{R}}{r^2}\mathbf{n}-\frac{3}{2}\mathbf{n}(\mathbf{u}-\mathbf{w})\cdot\mathbf{n}\left(\frac{R^3}{r^3}\right)+\frac{1}{2}(\mathbf{u}-\mathbf{w})\left(\frac{R^3}{r^3}\right)\right],\\
&=\int_{|\mathbf{s}|>R} dV_s\frac{R^4\dot{R}^2}{r^3}\mathbf{nnn}-3\frac{R^5\dot{R}}{r^4}\mathbf{nnn}(\mathbf{u}-\mathbf{w})\cdot\mathbf{n}+\frac{R^5\dot{R}}{r^4}\mathbf{nn}(\mathbf{u}-\mathbf{w})+\frac{9}{4}\mathbf{nnn}\left((\mathbf{u}-\mathbf{w})\cdot\mathbf{n}\right)^2\left(\frac{R^6}{r^5}\right)\\
&\quad-\frac{3}{2}\mathbf{nn}(\mathbf{u}-\mathbf{w})(\mathbf{u}-\mathbf{w})\cdot\mathbf{n}\left(\frac{R^6}{r^5}\right)+\frac{1}{4}\mathbf{n}(\mathbf{u}-\mathbf{w})(\mathbf{u}-\mathbf{w})\left(\frac{R^6}{r^5}\right),\\
&=\int_{|\mathbf{s}|=R} dS_s\Big\{-R^4\dot{R}^2\log(R)\mathbf{nnn}-3R^4\dot{R}\mathbf{nnn}(\mathbf{u}-\mathbf{w})\cdot\mathbf{n}+R^4\dot{R}\mathbf{nn}(\mathbf{u}-\mathbf{w})\\
&\quad+\frac{9}{8}R^4\mathbf{nnn}\left((\mathbf{u}-\mathbf{w})\cdot\mathbf{n}\right)^2-\frac{3}{4}R^4\mathbf{nn}(\mathbf{u}-\mathbf{w})(\mathbf{u}-\mathbf{w})\cdot\mathbf{n}+\frac{1}{8}R^4\mathbf{n}(\mathbf{u}-\mathbf{w})(\mathbf{u}-\mathbf{w})\Big\}.
\end{aligned}
\tag{C.49}
$$

Combining the above two results, we can write the Reynolds stress tensor as:

$$
\begin{aligned}
Mc &= \langle \mathbf{uu} \rangle - \langle \mathbf{u} \rangle \langle \mathbf{u} \rangle, \\
&\approx \beta_D \left[\frac{\overline{R^3 \dot{R}^2}}{\overline{R^3}} \mathbf{I} + \frac{3}{20} \frac{\overline{R^3 (\mathbf{u}-\mathbf{w}) \cdot (\mathbf{u}-\mathbf{w})}}{\overline{R^3}} \mathbf{I} + \frac{1}{20} \frac{\overline{R^3 (\mathbf{u}-\mathbf{w})(\mathbf{u}-\mathbf{w})}}{\overline{R^3}} \right] \\
&+ \frac{6}{10} \mathbf{I} \nabla \cdot \left(\frac{\beta_D \overline{R^4 \dot{R} (\mathbf{u}-\mathbf{w})}}{\overline{R^3}} \right) + \frac{1}{10} \nabla \left(\frac{\beta_D \overline{R^4 \dot{R} (\mathbf{u}-\mathbf{w})}}{\overline{R^3}} \right) + \frac{1}{10} \left[\nabla \left(\frac{\beta_D \overline{R^4 \dot{R} (\mathbf{u}-\mathbf{w})}}{\overline{R^3}} \right) \right]^T .
\end{aligned}
\tag{C.50}
$$

To summarize the development, we find that the governing equations are:

$$
\frac{\partial}{\partial t} \langle \rho_M \rangle + \nabla \cdot \left(\langle \rho_M \rangle \langle \mathbf{u}_M \rangle \right) = 0, \tag{C.51}
$$

$$
\begin{aligned}
&\frac{\partial}{\partial t} \left(\langle \rho_M \rangle \langle \mathbf{u}_M \rangle \right) + \nabla \cdot \left(\langle \rho_M \rangle \langle \mathbf{u}_M \rangle \langle \mathbf{u}_M \rangle \right) + \nabla \langle p_C \rangle \\
&\quad = \nabla \left[\beta_D \left(\langle p_C \rangle - \frac{\langle R^3 p_B(R) \rangle}{\langle R^3 \rangle} \right) \right] - \nabla \cdot \left(\rho_M Mc \right),
\end{aligned}
\tag{C.52}
$$

where Mc is given by equation C.50.

The derivation of the momentum equation C.52 is rooted in the first order expansion of the local probability density function $\mathcal{P}(\mathbf{y}, R, R_o, \mathbf{w}, \dot{R}, t)$ in the neighborhood of one bubble diameter ($|\mathbf{y}-\mathbf{x}| \leq R$). Therefore, rapid changes in the properties of the cavitation field, such as a band of decreased cavitation in the case of the dual-pulse lithotripter, are represented with decreased accuracy. The introduction of higher-order expansions in the derivation should remedy this limitation.

The closure of the above equations requires the introduction of modeling for averages of bubble states and velocities. These issues are addressed in Section C.1.3.

C.1.3 Equations for the disperse phase

The derivation of the equations for the average mixture and disperse phase requires a model for the behavior of a discrete bubble. If we assume that the lengthscales associated with the flow gradients are significantly larger than R, then the bubble will behave as if it was in a uniform flow field extending to infinity. Although this assumption is usually made in numerical modeling of cavitation, it must be invoked carefully in the case of lithotripsy since the shock wave is thin compared to R. However, the derivation and implementation of a numerical model capable of representing the interaction between shock waves and bubbles is beyond the scope of this work. Therefore, the flow field in the vicinity of a bubble was taken as uniform in spite of the presence of large gradients in the average mixture during the passage of the shock wave.

Another important assumption in the derivation of the disperse phase equations is the absence of direct bubble–bubble interactions. As discussed before, the model only accounts for indirect coupling between bubbles via changes in the average mixture pressure. This assumption is appropriate for simulations with void fractions of the order of a few percent since direct bubble–bubble interactions are only effective when bubbles are within a few bubble diameter from each other. However, it should be noted that for larger void fractions, the numerical model may yield overlapping bubbles since the growth of a bubble is not restricted by the presence of neighboring bubbles.

We first consider relatively slow bubble motion for which the flow field near a bubble is nearly incompressible. If in addition it is irrotational, the flow field can be derived from a potential. For simplicity, this potential is formulated in a frame of reference traveling at the bubble translational speed $\mathbf{w}$:

$$\phi = -\frac{R^2\dot{R}}{r} + (\mathbf{u}-\mathbf{w})\cdot\mathbf{s} + \frac{(\mathbf{u}-\mathbf{w})\cdot\mathbf{s}}{2}\left(\frac{R}{r}\right)^3. \tag{C.46'}$$

It should be noted that in this frame of reference the Bernoulli equation is

$$\frac{\partial\phi}{\partial t} + \frac{1}{2}\nabla\phi\cdot\nabla\phi - \frac{1}{2}\mathbf{w}\cdot\mathbf{w} + \dot{\mathbf{w}}\cdot\mathbf{s} + \frac{p}{\rho} = C(t). \tag{C.53}$$

Since $C(t)$ is only a function of time, we can write

$$C(t) = \left[\frac{\partial\phi}{\partial t} + \frac{1}{2}\nabla\phi\cdot\nabla\phi - \frac{1}{2}\mathbf{w}\cdot\mathbf{w} + \dot{\mathbf{w}}\cdot\mathbf{s} + \frac{p}{\rho}\right]_{r\to\infty}, \tag{C.54}$$

$$\begin{aligned}\frac{\partial\phi}{\partial t} + \frac{1}{2}\nabla\phi\cdot\nabla\phi - \cancel{\frac{1}{2}\mathbf{w}\cdot\mathbf{w}} + \cancel{\dot{\mathbf{w}}\cdot\mathbf{s}} + \frac{p}{\rho} \\ = (\dot{\mathbf{u}}-\dot{\mathbf{w}})\cdot\mathbf{s} + \frac{1}{2}(\mathbf{u}-\mathbf{w})\cdot(\mathbf{u}-\mathbf{w}) - \cancel{\frac{1}{2}\mathbf{w}\cdot\mathbf{w}} + \cancel{\dot{\mathbf{w}}\cdot\mathbf{s}} + \frac{p_\infty}{\rho},\end{aligned} \tag{C.55}$$

or,

$$\frac{\partial\phi}{\partial t} + \frac{1}{2}\nabla\phi\cdot\nabla\phi + \frac{p}{\rho} = (\dot{\mathbf{u}}-\dot{\mathbf{w}})\cdot\mathbf{s} + \frac{1}{2}(\mathbf{u}-\mathbf{w})\cdot(\mathbf{u}-\mathbf{w}) + \frac{p_\infty}{\rho}. \tag{C.56}$$

Since the liquid velocity $\mathbf{u}$ is assumed to be locally uniform $\mathbf{u} = \mathbf{u}(t)$, the pressure field is therefore linear in space $p_\infty = A(t) + \mathbf{B}(t)\cdot\mathbf{s}$.

The velocity at the bubble surface is

$$\nabla\phi = \dot{R}\mathbf{n} - \frac{3}{2}\mathbf{n}(\mathbf{u}-\mathbf{w})\cdot\mathbf{n} + \frac{3}{2}(\mathbf{u}-\mathbf{w}), \tag{C.57}$$

and

$$\begin{aligned}\nabla\phi\cdot\nabla\phi &= \dot{R}^2 + 3\dot{R}(\mathbf{u}-\mathbf{w})\cdot\mathbf{n} - 3\dot{R}(\mathbf{u}-\mathbf{w})\cdot\mathbf{n} + \frac{9}{4}(\mathbf{u}-\mathbf{w})\cdot(\mathbf{u}-\mathbf{w}) \\ &\quad -\frac{9}{2}(\mathbf{u}-\mathbf{w})\cdot\mathbf{n}(\mathbf{u}-\mathbf{w})\cdot\mathbf{n} + \frac{9}{4}(\mathbf{u}-\mathbf{w})\cdot\mathbf{n}(\mathbf{u}-\mathbf{w})\cdot\mathbf{n}, \\ &= \dot{R}^2 + \frac{9}{4}(\mathbf{u}-\mathbf{w})\cdot(\mathbf{u}-\mathbf{w}) - \frac{9}{4}(\mathbf{u}-\mathbf{w})\cdot\mathbf{n}(\mathbf{u}-\mathbf{w})\cdot\mathbf{n}. \end{aligned} \tag{C.58}$$

Theraefore, the pressure at the bubble surface can be written as

$$\begin{aligned}\frac{p-p_\infty}{\rho} &= R\ddot{R} + 2\dot{R}^2 - \frac{3}{2}R(\dot{\mathbf{u}}-\dot{\mathbf{w}})\cdot\mathbf{n} - \frac{3}{2}\dot{R}(\mathbf{u}-\mathbf{w})\cdot\mathbf{n} + R(\dot{\mathbf{u}}-\dot{\mathbf{w}})\cdot\mathbf{n} + \frac{1}{2}(\mathbf{u}-\mathbf{w})\cdot(\mathbf{u}-\mathbf{w}) \\ &\quad -\frac{1}{2}\left[\dot{R}^2 + \frac{9}{4}(\mathbf{u}-\mathbf{w})\cdot(\mathbf{u}-\mathbf{w}) - \frac{9}{4}(\mathbf{u}-\mathbf{w})\cdot\mathbf{n}(\mathbf{u}-\mathbf{w})\cdot\mathbf{n}\right], \\ &= R\ddot{R} + \frac{3}{2}\dot{R}^2 - \frac{1}{2}R(\dot{\mathbf{u}}-\dot{\mathbf{w}})\cdot\mathbf{n} - \frac{3}{2}\dot{R}(\mathbf{u}-\mathbf{w})\cdot\mathbf{n} - \frac{5}{8}(\mathbf{u}-\mathbf{w})\cdot(\mathbf{u}-\mathbf{w}) \\ &\qquad\qquad +\frac{9}{8}(\mathbf{u}-\mathbf{w})\cdot\mathbf{n}(\mathbf{u}-\mathbf{w})\cdot\mathbf{n}. \end{aligned} \tag{C.59}$$

The total radial force on the bubble wall must be zero:

$$\int dS\ \ p - p_B = 0, \tag{C.60}$$

$$\begin{aligned}\frac{p_B-p_\infty}{\rho} &= \frac{1}{4\pi R^2}\int dS\Big\{R\ddot{R} + \frac{3}{2}\dot{R} - \frac{1}{2}R(\dot{\mathbf{u}}-\dot{\mathbf{w}})\cdot\mathbf{n} - \frac{3}{2}\dot{R}(\mathbf{u}-\mathbf{w})\cdot\mathbf{n} \\ &\quad -\frac{5}{8}(\mathbf{u}-\mathbf{w})\cdot(\mathbf{u}-\mathbf{w}) + \frac{9}{8}(\mathbf{u}-\mathbf{w})\cdot\mathbf{n}(\mathbf{u}-\mathbf{w})\cdot\mathbf{n}\Big\}, \\ &= R\ddot{R} + \frac{3}{2}\dot{R} - \frac{5}{8}(\mathbf{u}-\mathbf{w})\cdot(\mathbf{u}-\mathbf{w}) + \frac{3}{8}(\mathbf{u}-\mathbf{w})\cdot(\mathbf{u}-\mathbf{w}), \\ &= R\ddot{R} + \frac{3}{2}\dot{R} - \frac{1}{4}(\mathbf{u}-\mathbf{w})\cdot(\mathbf{u}-\mathbf{w}), \end{aligned} \tag{C.61}$$

where p_B is the pressure in the liquid at the surface of the bubble. The above result is the well known Rayleigh-Plesset equation:

$$R\ddot{R} + \frac{3}{2}\dot{R}^2 - \frac{1}{4}U_{\rm rel}\cdot U_{\rm rel} = \frac{p_\infty - p_B(t)}{\rho}. \tag{C.62}$$

Similarly, if we assume that the bubble is massless then the net force applied to it must be zero:

$$\int dS \;\; p\mathbf{n} = 0, \tag{C.63}$$

$$\begin{aligned}\int dS\Big\{ \frac{p_\infty}{\rho} R\mathbf{n}(R\ddot{R} + \frac{3}{2}\dot{R})\mathbf{n} - \frac{1}{2}R\mathbf{n}(\dot{\mathbf{u}} - \dot{\mathbf{w}})\cdot\mathbf{n} - \frac{3}{2}\dot{R}\mathbf{n}(\mathbf{u}-\mathbf{w})\cdot\mathbf{n} \\ -\frac{5}{8}\mathbf{n}(\mathbf{u}-\mathbf{w})\cdot(\mathbf{u}-\mathbf{w}) + \frac{9}{8}\mathbf{n}(\mathbf{u}-\mathbf{w})\cdot\mathbf{n}(\mathbf{u}-\mathbf{w})\cdot\mathbf{n}\Big\} = 0,\end{aligned}$$

$$\frac{\nabla p_\infty}{\rho} R - \frac{1}{2}R(\dot{\mathbf{u}} - \dot{\mathbf{w}}) - \frac{3}{2}\dot{R}(\mathbf{u}-\mathbf{w}) = 0, \tag{C.64}$$

so

$$(\dot{\mathbf{u}} - \dot{\mathbf{w}}) = 2\frac{\nabla p_\infty}{\rho} - 3\frac{\dot{R}}{R}(\mathbf{u}-\mathbf{w}). \tag{C.65}$$

The above results are the classical solutions for a bubble in an incompressible flow field. The potential used in this model was also used in the derivation for the Reynolds stress and pressure gradient term in the ensemble phase average of the mixture. However, this approach is limited to slow bubble expansion and collapse. For more violent bubble behavior, compressible effects can no longer be ignored.

Several extensions have been proposed to provide a first or second order correction for compressibility effects. A general analysis was presented by Prosperetti & Lezzi (1986), which covers many of the different compressible models developed previously. In this approach, the authors considered two regions of fluid: an inner region where the liquid is approximately incompressible and a compressible outer region where the fluid kinetic energy is negligible. A singular-perturbation analysis was then performed to match these two layers and obtain an ODE for the rate of change of the bubble radius as a function of the difference between the bubble wall pressure and the forcing pressure. The final result, called the general Keller-Herring equation, is

$$\begin{aligned}&\left[1 - (\lambda+1)\frac{\dot{R}}{C}\right] R\ddot{R} + \frac{3}{2}\left[1 - \frac{(3\lambda+1)}{3}\frac{\dot{R}}{C}\right]\dot{R}^2 = \\ &\left[1 + (1-\lambda)\frac{\dot{R}}{C}\right]\left(H - \frac{p_\infty}{\rho}\right) + \frac{R}{C}\frac{\partial}{\partial t}\left(H - \frac{p_\infty}{\rho}\right).\end{aligned} \tag{C.66}$$

where p_∞ is the pressure at that location in the absence of a bubble, p_o is a reference pressure and enthalpy H is defined as

$$H = \int_{p_o}^{p_\infty} \frac{dp}{\rho}. \tag{C.67}$$

The above bubble model is valid for arbitrary values of λ. For the purpose of this work, the free parameter λ was chosen to be zero which corresponds to the well known Gilmore equation (Gilmore 1952):

$$\left[1-\frac{\dot{R}}{c}\right]R\ddot{R}+\frac{3}{2}\left[1-\frac{1}{3}\frac{\dot{R}}{c}\right]\dot{R}^2=\left[1+\frac{\dot{R}}{c}\right]H+\frac{R}{c}\frac{dH}{dt}\qquad H=\int_{p_\infty(t)}^{p_B(R,t)}\frac{dp}{\rho}, \tag{C.68}$$

where p_B is again the pressure in the liquid at the surface of the bubble.

Both compressible and incompressible bubble models were used in this work to compute the evolution of the bubble field. However, because of limitations in the derivation of the compressible bubble model, only the incompressible model was used to compute Reynolds stress term for the ensemble averaged Euler equations.

So far in this analysis, the conditions prevailing inside the bubble have not yet been modeled. All equations have been expressed as a function of the liquid pressure at the bubble wall p_B. In the next section, modeling of the bubble interior is used to express p_B as a function of the bubble radius and other parameters.

C.1.4 Bubble interior

The bubble interior can be modeled as a mixture of vapor and non-condensible gas. In the work of Matsumoto & Takemura (1994), the governing equations (unsteady, radial diffusion equations) for both vapor and gas as well as the behavior of the liquid were solved numerically for the single bubble case. However, for the purpose of this work, such calculations would be prohibitively expensive to perform at each point in space. Instead, the behavior of a single bubble must be reduced to a simpler model.

The most commonly used simplification for the modeling the bubble interior is the assumption that the gas mixture is uniform in composition, pressure and temperature for all times. This effectively eliminates all dynamics related to mass, momentum and heat transfer within the bubble. The following lists the complete set of assumptions regarding the state of the bubble interior used in this work:

- The gas core of the bubble is composed of a uniform mixture of vapor and an adiabatic non-condensible gas.

$$\frac{p_{air}}{\rho_{air}^{\gamma}}=\text{constant}\qquad \gamma=\text{ ratio of specific heats}$$

- The gas mixture is assumed to be at a spatially uniform temperature and pressure.

$$p = p(t) = p_{air}(t) + p_{vap}(t)$$

- The mass flux of non-condensible gas across the bubble interface is assumed to be negligible.

$$\frac{4}{3}\pi R^3 \rho_{air} = \text{constant}$$

- The vaporization/condensation of the vapor is presumed sufficiently rapid to ensure equilibrium condition across the bubble interface.

$$p_{vap} = p_{\text{saturated vapor}}(T_{\text{wall}}) \qquad T_{\text{wall}} = \text{ temperature at the bubble interface}$$

- Mass and heat transfer in the surrounding liquid is neglected.

$$T_{\text{wall}} = T_\infty \rightarrow p_{vap} = \text{constant}$$

Given the above simplifications, the following can be stated:

$$p_B(R) = -\frac{2S}{R(t)} + p_{vap} + p_o \left(\frac{R_o}{R(t)}\right)^{3\gamma}, \tag{C.69}$$

$S =$ surface tension coefficient,

$p_o, R_o =$ pressure and radius at some reference time,

$p_B(R) =$ pressure in the liquid at the bubble surface.

Taking the rest (initial) condition as the reference:

$$p_B = p_o - \frac{2S}{R_o}\left[\left(\frac{R_o}{R}\right) - \left(\frac{R_o}{R}\right)^{3\gamma}\right] - (p_o - p_{\text{sat vap}})\left[1 - \left(\frac{R_o}{R}\right)^{3\gamma}\right]. \tag{C.70}$$

C.1.5 Modeling the probability distribution

The average mixture equations of Section C.1.2 are function of correlations of bubble properties such as $\langle R^3 \rangle$ and $\langle R^3 p_B(R) \rangle$. These correlations can be obtained by averaging the bubble states governed by equations

presented in Section C.1.3. The integrals can be approximated by averaging over a population of bubbles of discrete states, which are evolved independently (Wang 1999). However, this requires the computation of a large number of different bubble states for each location, which is impractical in large simulations. For a more practical model, two alternatives were investigated. Following the work of Zhang & Prosperetti (1994), a narrow distribution of states can be considered. Given a sufficiently compact distribution, the probability field can be approximated by a single state. An alternative approach for wide distributions involves representing the probability field in terms of shape functions that can be evolved in time using approximate governing equations. Although this later approach does offer some benefits over the former, it was not used in this work because of unresolved issues in the modeling. For the interested reader, notes and comments on this novel approach can be found in Appendix H.

Following the work of Zhang & Prosperetti (1994), given a probability field assumed to be narrowly distributed about the averages, the following simplification can be made:

$$\mathcal{P}(\mathbf{x}, R, R_o, \mathbf{w}, \dot{R}, t) \approx \delta(R - \bar{R}(\mathbf{x}, t))\delta(\dot{R} - \bar{\dot{R}}(\mathbf{x}, t)\delta(\mathbf{w} - \bar{\mathbf{w}}(\mathbf{x}, t))N(\mathbf{x}, t). \tag{C.71}$$

where $N(\mathbf{x}, t)$ is the bubble number density. Consequently

$$\begin{aligned} Mc \approx \beta_D &\left[-\dot{\bar{R}}^2\mathbf{I} - \frac{3}{20}(\mathbf{u} - \bar{\mathbf{w}}) \cdot (\mathbf{u} - \bar{\mathbf{w}})\mathbf{I} - \frac{1}{20}(\mathbf{u} - \bar{\mathbf{w}})(\mathbf{u} - \bar{\mathbf{w}})\right] \\ &- \frac{6}{10}\mathbf{I}\nabla \cdot \left(\beta_D \bar{R}\dot{\bar{R}}(\mathbf{u} - \bar{\mathbf{w}})\right) - \frac{1}{10}\nabla\left(\beta_D \bar{R}\dot{\bar{R}}(\mathbf{u} - \bar{\mathbf{w}})\right) - \frac{1}{10}\left[\nabla\left(\beta_D \bar{R}\dot{\bar{R}}(\mathbf{u} - \bar{\mathbf{w}})\right)\right]^T, \end{aligned} \tag{C.72}$$

C.1.6 Relative motion of bubbles

So far, the only modeling that has been introduced to account for the motion of bubbles relative to the average liquid is equation C.65. Since the forces involved are small, translational forces over the bubble were neglected in this work. Consequently, the bubbles are assumed to move with the same velocity as the fluid. This is consistent with the observation made by Sokolov *et al.* (2001).

$$\bar{\mathbf{w}} \approx \mathbf{u} \tag{C.73}$$

As a result of this approximation, the Reynolds stress term can be simplified to

$$Mc = \beta_D \dot{\bar{R}}^2 \mathbf{I}. \tag{C.74}$$

and the number density transport equation becomes

$$\frac{\partial N}{\partial t} + \frac{\partial}{\partial \mathbf{x}}(\mathbf{u}N) = 0. \tag{C.75}$$

C.2 Final equations

The final form of the governing equations for the mixture (the averaging brackets $\langle\rangle$ and mixture subscript $_M$ have been omitted in order to simplify the notation)

$$\frac{\partial \rho}{\partial t} + \nabla \cdot (\rho \mathbf{u}) = 0, \tag{C.76}$$

$$\frac{\partial \rho \mathbf{u}}{\partial t} + \nabla \cdot (\rho \mathbf{u}\mathbf{u}) + \nabla p_C = \nabla \left[\beta_D (p_C - p_B(R) - \rho \dot{R}^2) \right], \tag{C.77}$$

$$p_C - p_o = \frac{\rho_o C^2}{\alpha} \left[\left(\frac{\rho_C}{\rho_o} \right)^{\alpha} - 1 \right], \tag{C.78}$$

$$p_B = -\frac{2S}{R_o} \left[\left(\frac{R_o}{R} \right) - \left(\frac{R_o}{R} \right)^{3\gamma} \right] - (p_o - p_{\text{sat vap}}) \left[1 - \left(\frac{R_o}{R} \right)^{3\gamma} \right] + p_o, \tag{C.79}$$

$$\rho_C = \frac{\rho}{(1 - \beta_D)}, \tag{C.80}$$

$$\beta_D = \frac{4}{3} \pi N \bar{R}^3, \tag{C.81}$$

$$\frac{\partial N}{\partial t} + \nabla \cdot N\mathbf{u} = 0. \tag{C.82}$$

The governing equations for the bubble phase are

$$R\ddot{R} + \frac{3}{2}\dot{R}^2 = \frac{p_B - p_C}{\rho}, \tag{C.83}$$

or

$$\left[1 - \frac{\dot{R}}{c} \right] R\ddot{R} + \frac{3}{2} \left[1 - \frac{1}{3}\frac{\dot{R}}{c} \right] \dot{R}^2 = \left[1 + \frac{\dot{R}}{c} \right] H + \frac{R}{c}\frac{dH}{dt} \qquad H = \int_{p_C}^{p_B} \frac{dp_C}{\rho_C}, \tag{C.84}$$

for the Rayleigh-Plesset and Gilmore cases, respectively.

Appendix D

Linear acoustics inside reflector

As a first order approximation of the propagation of waves inside the reflector bowl, geometrical acoustics is often used in the past. Although this approach cannot represent diffraction effects, it can accurately model wave reflection off solid surface in cases where the wavelengths associated with the incident wave are much smaller than the curvature of the reflector. This section present the basic calculations for the linear geometrical acoustic model of a spherical wave propagating inside an ellipsoidal bowl. Figure D.1 and D.2 present the relevant variables for this particular case.

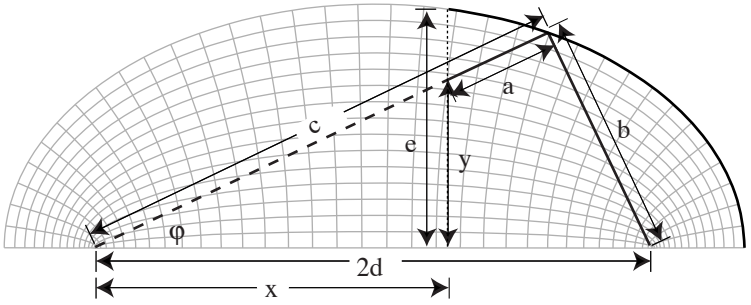

Figure D.1: Geometry of ellipsoidal reflector.

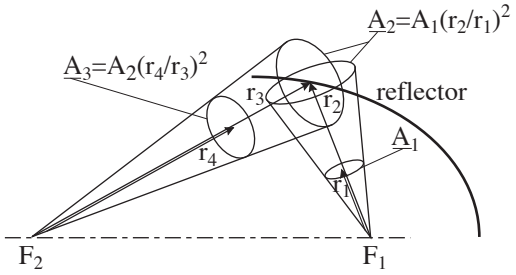

Figure D.2: Geometry of beam propagation.

From the geometry of the reflector (see Figure D.1), we can write the following relations:

$$L = b + c \tag{D.1}$$

$$b^2 = c^2 - 2c(2d)\cos(\phi) + (2d)^2 \tag{D.2}$$

Simplifying the last equation, we can write:

$$b = \frac{L^2 - 2(2d) * L\cos(\phi) + (2d)^2}{2(L - (2d)\cos(\phi))} \tag{D.3}$$

Assuming that the wave propagates as a beam (as seen in Figure D.2) and that its amplitude scales with area$^{-1/2}$, the amplification factor for the pressure measured at the mouth of the reflector is

$$\frac{p_{\text{mouth}}}{p_{\text{initial}}} = \sqrt{\frac{A_1}{A_3}} \tag{D.4}$$

$$= \left(\frac{r_1}{r_2}\right)\left(\frac{r_3}{r_4}\right) \tag{D.5}$$

$$= \frac{b_0 c}{b(c-a)} \tag{D.6}$$

$$= \frac{b_0(L-b)}{b\sqrt{y^2+x^2}} \tag{D.7}$$

Along the axis of symmetry, the wave amplitude is

$$p(z) = \left(\frac{zo}{z}\right)[f(z - zo - ct) + f(z + zo + ct)] + \left(\frac{zo}{L/2 - d}\right)\left(\frac{d + L/2}{2d - z}\right) f(z - ct + L - 2d) \tag{D.8}$$

where $f(z)$ is the profile of the initial wave and z is the distance from $\mathbf{F}_1$ in the direction of $\mathbf{F}_2$.

Appendix E

Wave propagation

In this section, the discretization of the second order wave propagation inside an ellipsoidal reflector bowl is presented (see Figure E.1). The second order wave equation is

$$c^2 \frac{\partial^2 \phi}{\partial t^2} = \nabla^2 \phi \tag{E.1}$$

with the Neumann boundary condition

$$\nabla \phi \cdot \mathbf{n} = 0 \tag{E.2}$$

on the axis of symmetry and on the surface of the reflector.

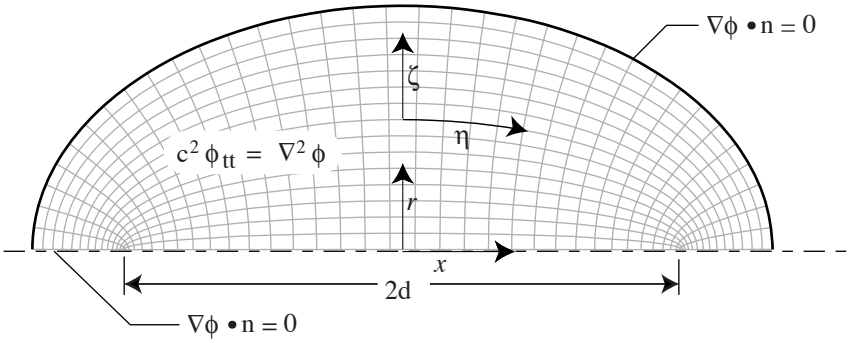

Figure E.1: Geometry of ellipsoidal reflector bowl.

In order to simplify the discretization of the problem, the Laplacian operator was cast in the following prolate spheroidal coordinate system (see Figure E.1):

$$\nabla^2 \phi = \frac{1}{\zeta^2 - \eta^2} \left[\frac{1}{\zeta^2 - 1} \frac{\partial}{\partial \zeta} \left((\zeta^2 - 1) \frac{\partial \phi}{\partial \zeta} \right) + \frac{1}{1 - \eta^2} \frac{\partial}{\partial \eta} \left((1 - \eta^2) \frac{\partial \phi}{\partial \eta} \right) \right] \tag{E.3}$$

where

$$\eta\epsilon[-1,1], \quad \zeta\epsilon[1,\zeta_{\text{reflector}}]$$
$$r = d\sqrt{(\eta^2-1)(\zeta^2-1)}, \quad x = d\zeta\eta$$

The above form has the advantage that the operator as the form

$$(\zeta^2-\eta^2)\nabla^2\phi = \mathcal{L}_\zeta(\phi) + \mathcal{L}_\eta(\phi)$$

Since the operator $\mathcal{L}$ is a linear operator of one dependent variable and the grid is rectangular, only one discretization of the operator is required for each direction.

In this work, the operator $\mathcal{L}$ was discretized using finite difference approximation. Given

$$\phi \approx a_0 + a_1(x-x_o) + a_2(x-x_o)^2 + a_3(x-x_o)^3 + a_4(x-x_o)^4, \tag{E.4}$$

$$\begin{aligned}\mathcal{L}_x(\phi) \approx a_1 C(x) + a_2\left[2 + 2C(x)(x-x_o)\right] + a_3\left[6(x-x_o) + 3C(x)(x-x_o)^2\right] \\ + a_4\left[12(x-x_o)^2 + 4C(x)(x-x_o)^3\right]\end{aligned}, \tag{E.5}$$

where

$$C(x) \equiv \frac{2x}{x^2-1},$$

or

$$\phi \approx V(x)\cdot A, \tag{E.6}$$
$$\mathcal{L}_x(\phi) \approx LV(x)\cdot A, \tag{E.7}$$

where

$$A \equiv [a_0, a_1, a_2, a_3, a_4],$$
$$V(x) \equiv \left[1, (x-x_o), (x-x_o)^2, (x-x_o)^3, (x-x_o)^4\right],$$
$$LV(x) \equiv \left[0, C(x), 2+2C(x)(x-x_o), 6(x-x_o)+3C(x)(x-x_o)^2, 12(x-x_o)^2+4C(x)(x-x_o)^3\right].$$

Using the above approximation, we can evaluate the operator $\mathcal{L}$ at a node i in terms of $(\phi_{i-1}, \phi_i, \phi_{i+1}, \mathcal{L}_{i-1}, \mathcal{L}_{i+1})$.

$$
\begin{aligned}
x_o &= x_i \\
\phi_{i-1} &\approx V(x_{i-1}) \cdot A \\
\phi_i &\approx V(x_i) \cdot A \\
\phi_{i+1} &\approx V(x_{i+1}) \cdot A \\
\mathcal{L}_{i-1} &\approx LV(x_{i-1}) \cdot A \\
\mathcal{L}_{i+1} &\approx LV(x_{i+1}) \cdot A
\end{aligned}
$$

Or

$$
\begin{bmatrix} \phi_{i-1} \\ \phi_i \\ \phi_{i+1} \\ \mathcal{L}_{i-1} \\ \mathcal{L}_{i+1} \end{bmatrix} \approx \mathbf{M} \cdot A, \tag{E.8}
$$

where

$$
\mathbf{M} = \begin{bmatrix} V(x_{i-1}) \\ V(x_i) \\ V(x_{i+1}) \\ LV(x_{i-1}) \\ LV(x_{i+1}) \end{bmatrix}.
$$

Using the above, we can write

$$
\mathcal{L}_i \approx LV(x_i) \cdot \mathbf{M}^{-1} \cdot \begin{bmatrix} \phi_{i-1} \\ \phi_i \\ \phi_{i+1} \\ \mathcal{L}_{i-1} \\ \mathcal{L}_{i+1} \end{bmatrix}, \tag{E.9}
$$

or equivalently

$$b_{i-1}\mathcal{L}_{i-1} + \mathcal{L}_i + b_{i+1}\mathcal{L}_{i+1} \approx c_{i-1}\phi_{i-1} + c_i\phi_i + c_{i+1}\phi_{i+1}, \tag{E.10}$$
$$b_i = b_i(x_{i-1}, x_i, x_{i+1}),$$
$$c_i = c_i(x_{i-1}, x_i, x_{i+1}).$$

Based on the above result, the evaluation of the operator $\mathcal{L}$ for a grid line in the domain requires the evaluation of the b's and c's constant (which only needs to be done once), and solving a tridiagonal system of equation.

The wave equation was integrated in time using a second order implicit Euler method

$$c^2 \frac{\phi^n - 2\phi^{n-1} + \phi^{n-2}}{\Delta t^2} \approx \nabla^2 \phi^n, \tag{E.11}$$

where the superscript refers to the appropriate time unit. Combining the time integration with the discrete approximation of the Laplacian operator, we obtain

$$(\zeta_i^2 - \eta_j^2)\frac{c^2}{\Delta t^2}\left(\phi_{ij}^n - 2\phi_{ij}^{n-1} + \phi_{ij}^{n-2}\right) \approx \mathcal{L}_{ij}^{\zeta} + \mathcal{L}_{ij}^{\eta}, \tag{E.12}$$

where

$$b_{i-1}^{\zeta}\mathcal{L}_{i-1j} + \mathcal{L}_{ij}b_{i+1}^{\zeta}\mathcal{L}_{i+1j} \approx c_{i-1}^{\zeta}\phi_{i-1j} + c_i^{\zeta}\phi_{ij} + c_{i+1}^{\zeta}\phi_{i+1j}, \tag{E.13}$$
$$b_{i-1}^{\eta}\mathcal{L}_{i-1j} + \mathcal{L}_{ij}b_{i+1}^{\eta}\mathcal{L}_{i+1j} \approx c_{i-1}^{\eta}\phi_{i-1j} + c_i^{\eta}\phi_{ij} + c_{i+1}^{\eta}\phi_{i+1j}, \tag{E.14}$$

where (b^{ζ}, c^{ζ}) and (b^{η}, c^{η}) are the b, c coefficients evaluated in the ζ-direction and η-direction respectively.

The overall solution algorithm used here is described as follows:

1. Generate rectangular grid in ζ, η coordinates.
2. Compute $b^{\zeta}, c^{\zeta}, b^{\eta}, c^{\eta}$ for the grid.
3. Set initial condition $\phi^0 = \phi(0, \mathbf{x})$ and $\phi^{-1} = \phi(0, \mathbf{x}) - \Delta t \phi_t(0, \mathbf{x})$.
4. Set $n = 1$.
5. Set $\phi^* = \phi^{n-1}$

6. Solve tridiagonal system for $\mathcal{L}^\zeta$ for each $\eta =$ constant line.

$$\mathcal{L}^\zeta = \mathcal{L}^\zeta(\phi^*)$$

7. Solve tridiagonal system for $\mathcal{L}^\eta$ for each $\zeta =$ constant line.

$$\mathcal{L}^\eta = \mathcal{L}^\eta(\phi^*)$$

8. Evaluate:

$$\phi^{**} = 2\phi^{n-1} - \phi^{n-2} + (\zeta^2 - \eta^2)\frac{\Delta t^2}{c^2}(\mathcal{L}^\zeta + \mathcal{L}^\eta)$$

9. Set $\phi^* = \alpha\phi^{**} + (1-\alpha)\phi^*$.

10. Goto step 6 until $\phi^{**} \approx \phi^*$ to sufficient accuracy.

11. Set $\phi^n = \phi^{**}$ and $n = n + 1$.

12. Goto step 5.

The value of α in above step 9 is a relaxation parameter used to control the convergence of the iteration process. For the purpose of this work, a value of $\alpha = 0.7$ was found to be adequate.

Appendix F

Estimation of bubble cloud parameters from experiments

As mentioned earlier in this work, the numerical model requires some characterization of the bubble cloud. In this present work, the cloud was assumed homogeneous and monodisperse so only two parameters are necessary for characterization: bubble initial size and number density of nuclei. The estimation of either parameters is complicated at best since bubbles are too small to be identified while the liquid is at rest.

The problem of estimating the initial bubble size in the liquid is a rather important one since it is required in order to use any type of numerical model for bubble dynamics. To solve this problem, the conventional approach uses two measurements that can be made relatively accurate: the pressure trace and the time between initial bubble growth and its first collapse (or time to collapse t_c). The pressure signal can be obtained using a membrane or the more accurate fiber optic pressure transducer. Although the time to collapse can be roughly estimated from high-speed photography, the more accurate approach is to used a focused hydrophone (passive cavitation detector) aimed at the appropriate location. Using the empirically measured pressure history as the forcing pressure in an appropriate model for bubble dynamics (Gilmore, Rayleigh-Plesset, Keller-Miksis, etc...) a plot of the numerical prediction for the time to collapse as a function of initial radius can be made.

The estimation of the bubble number density is an equally daunting task. As in the previous case, this parameter must be estimated from observations made during the firing of the lithotripter. The number of bubble nuclei present can be approximated using high-speed pictures of the bubble cloud during its maximum growth. As see in the following Figure (F.2), the larger bubbles can be easily identified however, the others (smaller bubbles and out of focus bubbles) are much more difficult to count. Close packing of bubbles also prevent an accurate census.

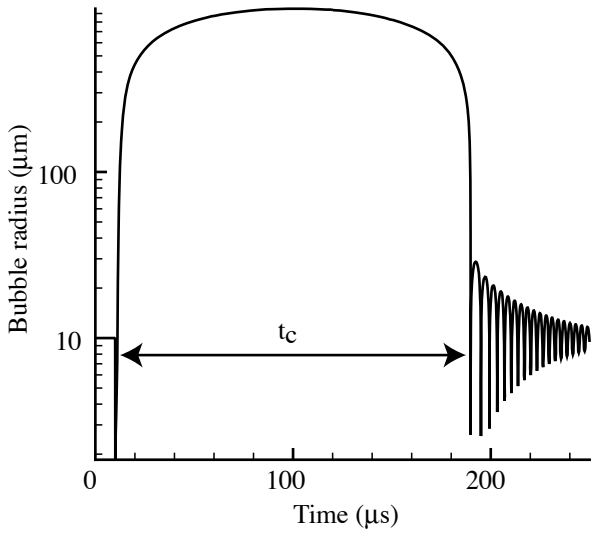

Figure F.1: Collapse time for a bubble at focus using Gilmore equation.

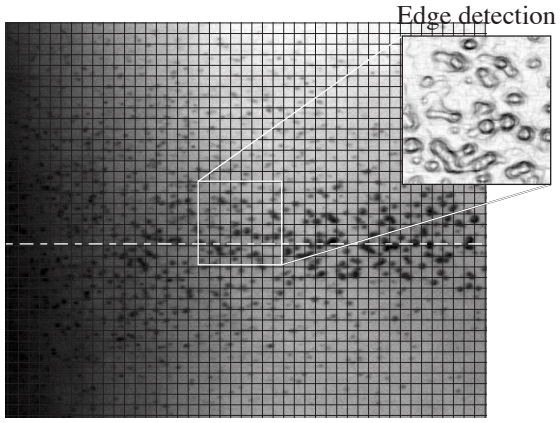

Figure F.2: Counting bubbles in high-speed picture of a bubble cloud for a free-field lithotripter.

As illustrated in the above figure, an estimation can be made of the number of bubbles present within a region of known size. For example, in the white square shown in Figure F.2, a total of approximately 32 bubbles can be identified. Although the dimension of the area shown is known (8 by 8 millimeters in this case), the depth of the field of view is unknown.

As shown in Figure F.3, the bubble density observed from the side view is the density integrated in the y–direction. This is further complicated by the limitation in the depth of field of view of the optical system for the high-speed camera.

In Figure F.2, approximately 32 bubbles can be identified within the highlighted box (8-by-8 mm). From the same picture, the cloud thickness can be roughly estimated at 35 mm. Using these numbers, the total

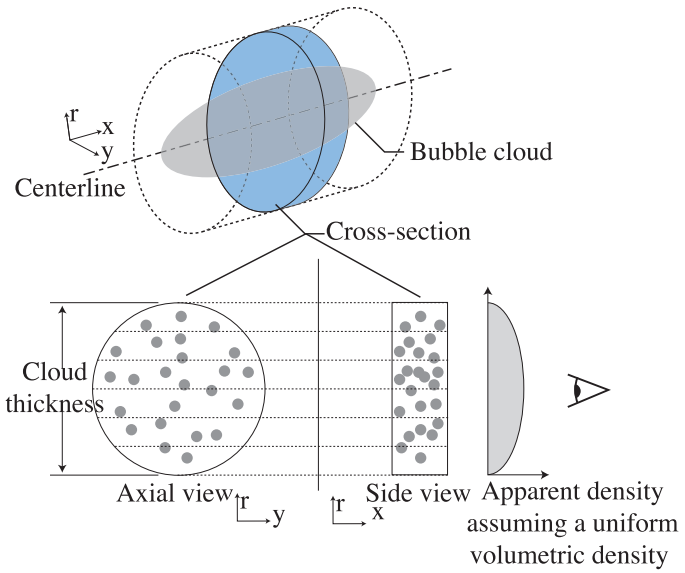

Figure F.3: Estimating nuclei density from side view section.

included volume encompassed by the box is slightly less than 2.24 cm^3 (8x8x35=2240 mm^3) which translates to a bubble number density of $32/2.24 = 14.29$ bubble/cm^3. By applying this approach on various regions over several different photographs, typical values for the bubble number density range from 5-50 bubbles/cm^3. Clearly, this range can vary considerably since both the bubble census and cloud size estimates are highly subjective. However, this approximate value for the bubble number density is consistent with observations from other researchers. As discussed in the results section of this work, the results from our numerical model based on these initial values are in reasonable agreement with empirical observations.

Appendix G

Modeling gas diffusion for single bubble model

In this section, we will cover the extension required to introduce gas diffusion model for a single bubble in uniform field. The equations relevant to the bubble exterior for this case are

$$\frac{\partial \rho}{\partial t} + \frac{1}{r^2}\frac{\partial}{\partial r}\left(r^2 \rho u_r\right) = 0, \tag{G.1}$$

$$\frac{\partial \rho u_r}{\partial t} + \frac{1}{r^2}\frac{\partial}{\partial r}\left(r^2 \rho u_r u_r\right) + \frac{\partial p}{\partial r} = 0, \tag{G.2}$$

$$p = C_p\left(\rho^\beta - 1\right), \tag{G.3}$$

$$\frac{\partial C\rho}{\partial t} + \frac{1}{r^2}\frac{\partial}{\partial r}\left(r^2 C \rho u_r\right) = \frac{1}{r^2}\frac{\partial}{\partial r}\left(r^2 \rho D \frac{\partial C}{\partial r}\right). \tag{G.4}$$

$$\tag{G.5}$$

It should be noted that in the above equations, it is implicitly assumed that the presence of dissolve gas does not impact on the liquid phase (which can be easily justified considering the concentration of gas is of the order of 10^-5) and that thermal effects are negligible. A first simplification can be made to the above set by assuming that the flow field is incompressible in the region near the bubble. The resulting equations are

$$u_r = \frac{R^2 \dot{R}}{r^2}, \tag{G.6}$$

$$\frac{\partial C}{\partial t} + u_r \frac{\partial C}{\partial r} = \frac{1}{r^2}\frac{\partial}{\partial r}\left(r^2 D \frac{\partial C}{\partial r}\right). \tag{G.7}$$

A very useful transformation for the last equation was presented in the work of Plesset & Zwick (1952)

and Eller & Flynn (1965).

$$z = \frac{1}{3}\left(r^3 - R^3\right) \tag{G.8}$$

$$\frac{\partial}{\partial r} = \frac{\partial}{\partial z} r^2 \tag{G.9}$$

$$\frac{\partial}{\partial t} = \frac{\partial}{\partial \tau} - \frac{\partial}{\partial z} R^2 \dot{R} \tag{G.10}$$

The equation for the concentration of gas in the transformed coordinates is

$$\left[\frac{\partial C}{\partial \tau} - R^2 \dot{R} \frac{\partial C}{\partial z}\right] + \frac{R^2 \dot{R}}{r^2}\left[r^2 \frac{\partial C}{\partial z}\right] = \frac{\partial}{\partial z}\left(r^4 D \frac{\partial C}{\partial z}\right), \tag{G.11}$$

$$\frac{\partial C}{\partial \tau} = \frac{\partial}{\partial z}\left(r^4 D \frac{\partial C}{\partial z}\right). \tag{G.12}$$

The last equation is particularly useful since the convective term has been removed from the equation. For the purpose of this work, the governing equation was discretized in the slightly different way:

$$x = \left(3z + R_o^3\right)^{1/3}, \tag{G.13}$$

$$\begin{aligned} \frac{\partial}{\partial z} &= \left(3z + R_o^3\right)^{-2/3} \frac{\partial}{\partial x}, \\ &= \frac{1}{x^2} \frac{\partial}{\partial x} \end{aligned} \tag{G.14}$$

$$\frac{\partial C}{\partial \tau} = \frac{1}{x^2} \frac{\partial}{\partial x}\left[\frac{\left(x^3 + R^3 - R_o^3\right)^{4/3}}{x^2} \frac{\partial C}{\partial x}\right]. \tag{G.15}$$

In the above transformation, a new parameter R_o is introduced. There are no restrictions on its value other than it must be positive. Based on numerical tests, it was found that for cases involving lithotripsy shock waves, a good choice is to set the value to the initial equilibrium bubble size ($R_o = R_{\text{initial}}$).

For the purpose of this work, the above formulation was discretized following an implicit finite volume approach. The spatial derivative was approximated to 2nd order accuracy while the time derivative was approximated using 1st order Euler method. Because the bubble can grow to several orders of magnitude, a stretched grid was used to minimize computational costs. Grid spacing as a function of the dependent variable x is shown in Figure G.1.

To validate the implementation, the model was used to compute the concentration field surrounding a sphere of fixed radius with constant concentration at the boundary. The solution for this problem is the well

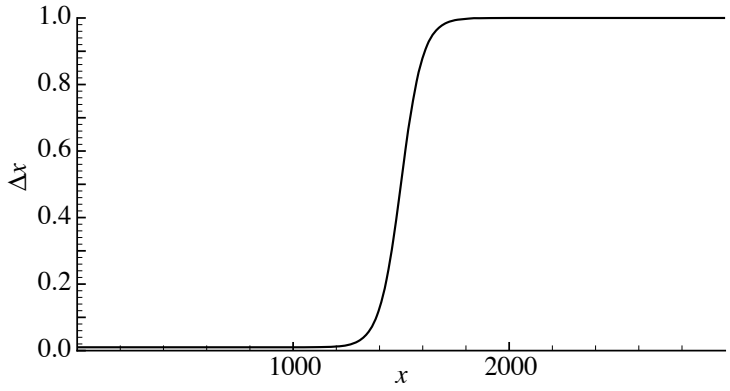

Figure G.1: Grid spacing for stretched grid.

known error function.

$$\frac{\partial C}{\partial t} = D\frac{1}{r^2}\frac{\partial}{\partial r}\left(r^2\frac{\partial C}{\partial r}\right) \tag{G.16}$$

$$C(t, r = R) = C_{\text{wall}} \tag{G.17}$$

$$C(t = 0, r) = C_{\infty} \tag{G.18}$$

$$C(t, r) - C_{\infty} = (C_{\text{wall}} - C_{\infty})\,\text{Erfc}\left(\frac{r - R}{\sqrt{4Dt}}\right) \tag{G.19}$$

$$\frac{\partial C}{\partial r}(t, r = R) = -\frac{C_{\text{wall}} - C_{\infty}}{\sqrt{\pi Dt}} \tag{G.20}$$

Figure G.2 shows the error of numerical model in the gradient and total flux for this diffusion problem.

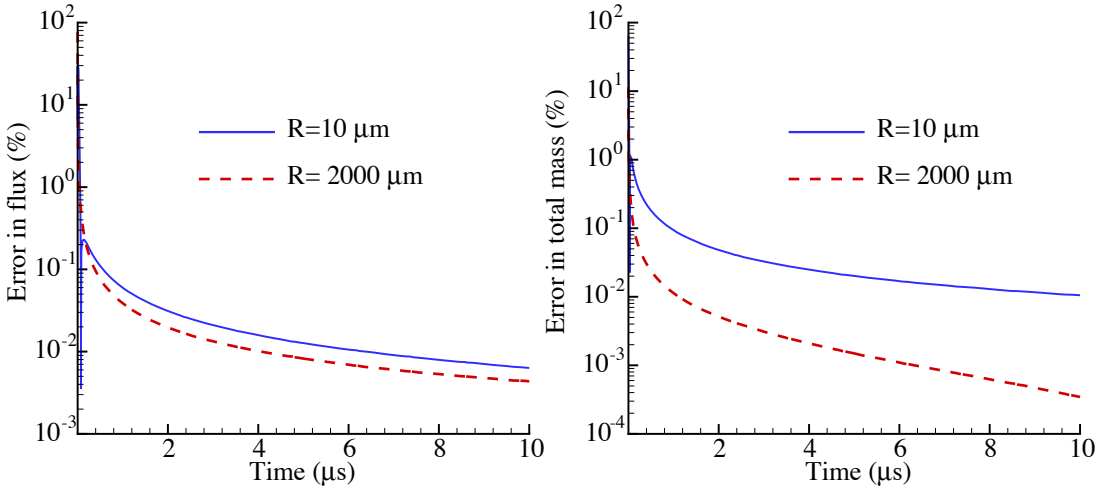

Figure G.2: Comparison between numerical model and analytical solution for simple diffusion problem ($R_o = 10\mu m$).

Appendix H

Dynamics of probability distribution of bubble states

This section presents some of our notes regarding simplifications in the modeling of a distribution of bubble states. For the purpose of this analysis, consider the following simplified probability distribution function for the bubble state at a particular location:

$$\mathcal{P} = \mathcal{P}(R, \dot{R}, t), \tag{H.1}$$

and the corresponding governing equation for the evolution of this probability field is

$$\frac{\partial \mathcal{P}}{\partial t} + \frac{\partial}{\partial R}\left(\dot{R}\mathcal{P}\right) + \frac{\partial}{\partial \dot{R}}\left(\ddot{R}\mathcal{P}\right) = 0. \tag{H.2}$$

The above equation can be discretized and solved numerically. This type of problem is usually solved using a Monte-Carlo approach and represent the evolving probability field by a set of discrete samples. This approach is advantageous in that the number of samples is independent of the number of states (dimensionality of the problem). However, every sample represents a bubble and may collapse violently at some point. Since computing a bubble collapse is expensive, computing a large sample set can become prohibitively expensive. A different approach to the problem is to discretized the problem as a convection problem.

Using the assumptions presented in this work, we can write

$$\ddot{R} = \ddot{R}(R, \dot{R}, t). \tag{H.3}$$

If we use the Rayleigh-Plesset bubble model then the above expression can be written as

$$R\ddot{R} + \frac{3}{2}\dot{R}^2 + f(R) + \frac{p_\infty(t)}{\rho} = 0. \tag{H.4}$$

The above equation can be integrated once to yield:

$$\frac{1}{2}R^3\dot{R}^2 + \int f(R)R^2 dR = E(t), \tag{H.5}$$

where $E(t)$ is the bubble energy which include the equilibrium energy and work done on the bubble by the pressure field. The energy term can be separated in the rest energy (E_o) and the pressure work term (the viscous damping term has been neglected in this analysis but can easily be introduced).

$$E(t) = E_o + \int_0^t \frac{p_\infty(t)}{\rho} R^2 \dot{R} dt \tag{H.6}$$

If we assume that the pressure field is zero, then the second order differential equation reduces to a first order equation. This simplification suggests a new set of variable instead of the $(R, \dot{R})$ combination. Using the polar coordinates (r, θ), the dependent variables can be rewritten as

$$r\sin(\theta) \equiv \frac{1}{\sqrt{2}} R^{3/2}\dot{R}, \tag{H.7}$$

$$r\cos(\theta) \equiv \sqrt{\int f(R)R^2 dR - E_o}, \tag{H.8}$$

$$r^2 = E(t), \tag{H.9}$$

and the inverse relation,

$$R = g\left(r\cos(\theta)\right). \tag{H.10}$$

The differential equations in the new coordinates are

$$\dot{r} = \frac{R^{1/2}\sin(\theta)}{\sqrt{2}} \frac{p_\infty(t)}{\rho}, \tag{H.11}$$

$$r\dot{\theta} = \frac{R^{1/2} f(R)}{\sqrt{2}\cos(\theta)} - \frac{R^{1/2}\cos(\theta)}{\sqrt{2}} \frac{p_\infty(t)}{\rho}. \tag{H.12}$$

The probability conservation equation can be rewritten in terms of this new coordinate system:

$$\frac{\partial \mathcal{P}'}{\partial t} + \frac{\partial}{\partial r}\left(\dot{r}\mathcal{P}'\right) + \frac{\partial}{\partial \theta}\left(\dot{\theta}\mathcal{P}'\right), \tag{H.13}$$

where

$$\mathcal{P}' = \frac{R^5 \dot{R} f(R)}{4r^3 \cos(\theta)\sin(\theta)}\mathcal{P} \tag{H.14}$$

If the absence of a forcing pressure field, the equations simplify to

$$\dot{r} = 0, \tag{H.15}$$

$$r\dot{\theta} = \frac{R^{1/2} f(R)}{\sqrt{2}\cos(\theta)}. \tag{H.16}$$

Figure H.1 shows the evolution of a smooth probability distribution in a zero pressure field. The right side of Figure H.1 shows the probability field in the transformed coordinates (using $r\cos(\theta) \equiv x$ and $r\sin(\theta) \equiv y$) while the left side presents the field in the corresponding $(R, \dot{R})$ coordinates. The computed bubble radius average for this case is shown in Figure H.2 as well as the result for a single bubble starting with the same initial average condition.

The differences between the smooth and narrow probability distribution are clear from Figure H.2:

- the average bubble radius oscillates at a slightly lower frequency,
- the average bubble radius does not collapse significantly but rather oscillates about a value larger than the equilibrium radius,
- the amplitude of oscillations for average radius diminishes steadily as if under the influence of some damping field.

These observation are a consequence of the shape of the probability distribution. The smoother the field, the more pronounced the above effects will be.

For large bubble oscillations, a much larger part of the period is spent at a radius above the equilibrium. Consequently, it is rather improbable to find a bubble during its collapse phase. For a smooth distribution, only a very small portion of the field enter the collapse region of the phase space at any given time. Since bubble motion is very fast during collapse, a probability packet entering quickly exits this region. This

transition from pre to post-collapse is illustrated in Figure H.3. This seemingly discontinuous propagation of the probability field results in a very smooth average behavior.

The observed damping in Figure H.2 is caused by variations in the oscillation frequency in the probability field. More energetic bubbles oscillate at a slower rate and therefore get progressively out of phase with less energetic bubbles. Consequently, a smooth probability field is stretched more and more after each oscillation. This stretching results in the so called damping observed above.

The average bubble motion for the smooth probability distribution seen in Figure H.2 is significantly less stiff than its narrow distributed counterpart. This suggests that a model representing the average could be much faster to compute. At the present stage, the only method available to represent the evolution of the average is the semi-lagrangian approach used above. The semi-lagrangian approach used in this example has the advantage of not having to compute the rapid changes due to bubble collapse however, because of the large number of nodes used in the grid (Figure H.1 was computed on a 1000x100 grid) this formulation far more expensive to compute than an approach based on a Monte-Carlo approach.

For the simplified case where both the pressure field and viscous damping are zero, the governing equation for the probability density simplifies to:

$$\frac{\partial \mathcal{P}'}{\partial t} + \frac{\partial}{\partial \theta}(\mathcal{P}'\dot{\theta}) = 0. \tag{H.17}$$

For a given energy level (r = constant) the probability field oscillates with periodicity τ.

$$\mathcal{P}'(t,\theta) = \sum_{n=1}^{\infty} a_n \exp\left[2\pi i n \frac{t}{\tau}\right] f_n(\theta) \tag{H.18}$$

Inserting the above solution in equation H.17, we can obtain a solution for the $f_n(\theta)$ functions:

$$f_n(\theta) = \frac{1}{\dot{\theta}} \exp\left[-\frac{2\pi i n}{\tau} \int_0^{\theta} \frac{d\theta}{\dot{\theta}}\right]. \tag{H.19}$$

The general probability field can thus be expressed as:

$$\mathcal{P}'(t,\theta) = \sum_{n=1}^{\infty} \frac{a_n}{\dot{\theta}} \exp\left[\frac{2\pi i n}{\tau}\left(t - \int_0^{\theta} \frac{d\theta}{\dot{\theta}}\right)\right]. \tag{H.20}$$

It is interesting to note that for a smooth distribution, the probability field can be represented accurately

by a small number of modes.

$$\mathcal{P}'(t,\theta) = \sum_{n=1}^{N} \frac{a_n}{\dot{\theta}} \exp\left[\frac{2\pi i n}{\tau}\left(t - \int_0^\theta \frac{d\theta}{\dot{\theta}}\right)\right], \tag{H.21}$$

$$\langle R \rangle = \sum_{n=1}^{N} a_n \exp\left[\frac{2\pi i n t}{\tau}\right] \bar{R}_n, \tag{H.22}$$

$$\bar{R}_n \equiv \int \frac{R(\theta)}{\dot{\theta}} \exp\left[-\frac{2\pi i n}{\tau}\int_0^\theta \frac{d\theta}{\dot{\theta}}\right] d\theta. \tag{H.23}$$

The averaged nonlinear second order ODE can be expressed in terms of a linear PDE (equation H.2, H.13 or H.17). At this stage, we have not found any way of converting the high dimensional linear problem back to a simpler nonlinear ODE model representing the average.

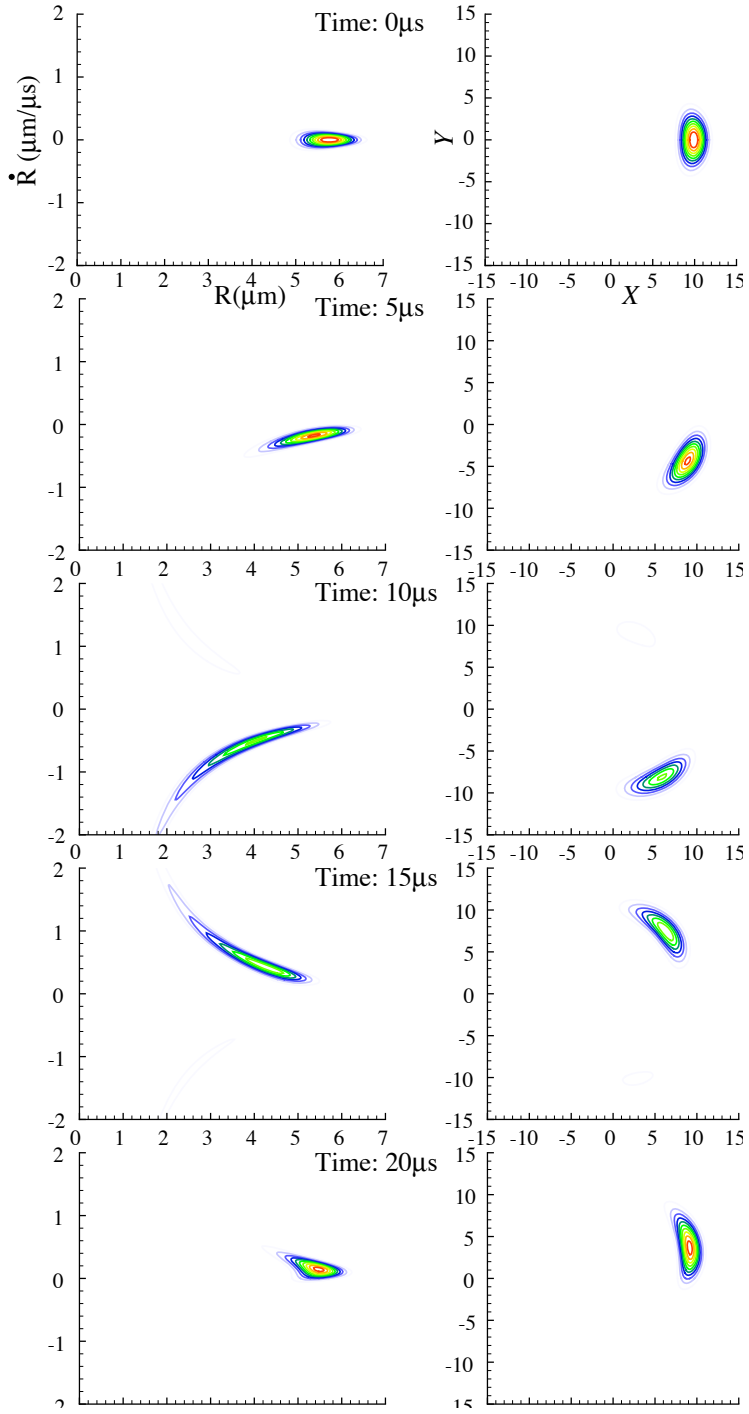

Figure H.1: Evolution of the probability density for zero pressure as function of $(R, \dot{R})$ and (x, y).

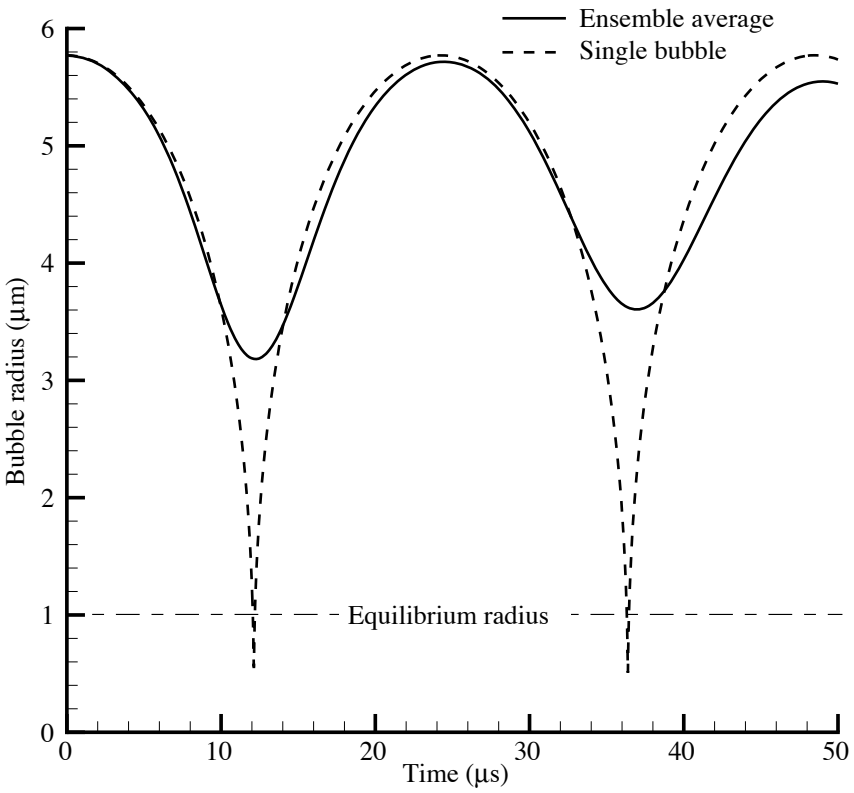

Figure H.2: Comparison between the average and single bubble radius.

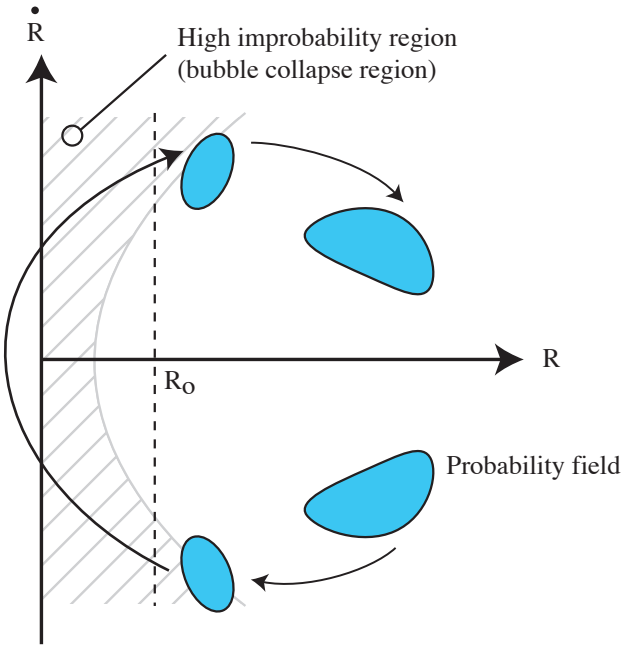

Figure H.3: Illustration of evolution of probability field for bubble collapse.

Bibliography

Averkiou, M. & R. Cleveland (1999). Modeling of an electrohydraulic lithotripter with the KZK equation. *Journal of the Acoustical Society of America 106*(1), 102–112.

Bailey, M., R. Cleveland, L. Crum & T. Matula (2003). Personal communication.

Bailey, M., L. Crum, O. Sapozhnikov, A. Evan, J. McAteer, R. Cleveland & T. Colonius (2003). Cavitation in shock wave lithotripsy. In *Proceedings of the 5th International Symposium on Cavitation*, Osaka, Japan. published electronically at http://iridium.me.es.osaka-u.ac.jp/cav2003/index.html : paper OS-2-1-006.

Biesheuvel, A. & L. van Wijngaarden (1984). Two-phase flow equations for a dilute dispersion of gas bubble in liquid. *Journal of Fluid Mechanics 148*, 301–318.

Blomgren, P., B. Connors, J. Lingeman, L. Willis & A. Even (1997). Quantitation of shock wave lithotripsy-induced lesion in small and large pig kidneys. *Anatomical Record 249*(3), 341–348.

Born, M. & E. Wolf (1980). *Principle of optics* (6th ed.)., Chapter 8.3.1. New York: Pergamon.

Brennen, C. (1995). *Cavitation and bubble dynamics*. Oxford University Press.

Cates, J. & B. Sturtevant (1997). Shock wave focusing using geometrical shock dynamics. *Physics of Fluids 9*(10), 3058–3068.

Christopher, T. (1994). Modeling the Dornier HM3 lithotripter. *Journal of the Acoustical Society of America 96*(5), 3088–3095.

Church, C. (1989). A theoretical study of cavitation generated by an extracorporeal shock wave lithotripter. *Journal of the Acoustical Society of America 86*(1), 215–227.

Cleveland, R., M. Bailey, N. Fineberg, B. Hartenbaum, M. Lokhandwalla, J. McAteer & B. Sturtevant (2000). Design and characterization of a research electrohydraulic lithotripter patterned after the Dornier HM3. *Review of Scientific Instruments 71*, 2514–2525.

Cole, R. (1948). *Underwater explosions*. Princeton, NJ: Princeton University Press.

Coleman, A., M. Choi & J. Saunders (1991). Theoretical predictions of the acoustic pressure generated by a shock wave lithotripter. *Ultrasound in Medicine and Biology 17*, 245–255.

Coleman, A. & J. Saunders (1993). A review of the physical-properties and biological effects of the high amplitude acoustic fields used in extracorporeal lithotripsy. *Ultrasonics 31*(2), 75–89.

Coleman, A., J. Saunders, R. Preston & D. Bacon (1987). Pressure waveforms generated by a Dornier extra-corporeal shock-wave lithotripter. *Ultrasound in Medicine and Biology 13*, 651–657.

Colonius, T., S. Lele & P. Moin (1993). Boundary conditions for direct computation of aerodynamic sound generation. *AIAA Journal 31*(9), 1574–1582.

Connors, B., A. Evan, L. Willis, P. Blomgen, J. Lingeman & N. Fineberg (2000). The effect of discharge voltage on renal injury and impairment caused by lithotripsy in the pig. *JASN 11*(2), 310–318.

Crum, L. (1988). Cavitation microjets as a contributory mechanism for renal calculi disintegration in ESWL. *Journa of Urology 140*, 1587–1590.

Crum, L. (2003). Personal communication.

Eller, A. & H. Flynn (1965). Rectified diffusion during nonlinear pulsations of cavitation bubbles. *Journal of the Acoustical Society of America 37*(3), 493–503.

Evan, A., L. Willis, B. Connors, J. McAteer, J. Lingeman, R. Cleveland, M. Bailey & L. Crum (1998). Separation of cavitation and renal injury induced by shock wave lithotripsy (SWL) from SWL-induced impairment of renal hemodynamics. In *Proc. 16th International Congress on Acoustics*, Volume 4, pp. 2487–2488.

Evan, A., L. Willis, J. Lingeman & J. McAteer (1997). Renal trauma and the risk of long-term complications in shock wave lithotripsy. *Nephron 78*, 1–8.

Gilmore, R. (1952). The growth or collapse of a spherical bubble in a viscous compressible liquid. Technical Report Rep. No. 26-4, California Institute of Technology.

Gottlieb, S. & C.-W. Shu (1998). Total variation diminishing Runge-Kutta schemes. *Mathematics of Computation 67*(221), 73–85.

Hamilton, M. (1993). Transient axial solution for the reflection of a spherical wave from a concave ellipsoidal mirror. *Journal of the Acoustical Society of America 93*(3), 1256–1266.

Harten, A. (1989). ENO schemes with subcell resolution. *Journal of Computational Physics 83*, 148–184.

Harten, A., B. Engquist, S. Oscher & S. Chakravarthy (1986). Some results on uniformly high-order accurate essentially nonoscillatory schemes. *Applied Numerical Mathematics 2*, 347–377.

Harten, A., B. Engquist, S. Oscher & S. Chakravarthy (1987). Uniformly high-order accurate essentially nonoscillatory schemes .3. *Journal of Computational Physics 71*, 231–303.

Harten, A. & S. Osher (1986). Uniformly high-order accurate nonoscillatory schemes.1. *SIAM Journal of Numerical Analysis 24*, 279–309.

Herring, C. (1941). Theory of the pulsations of the gas bubble produced by an underwater explosion. Technical Report 236, OSRD.

Hubert, P., K. Jöchle & J. Debus (1998). Influence of shock wave pressure amplitude and pulse repetition frequency on the lifespan, size and number of transient cavities in the field of an electromagnetic lithotripter. *Physics in Medicine and Biology 43*, 3113–3128.

Jiang, G. & C. Shu (1996). Efficient implementation of weighted ENO schemes. *Journal of Computational Physics 126*(1), 202–228.

Jöchle, K., J. Debus, W. Lorenz & P. Hubert (1996). A new method of quantitative cavitation assessment in the field of a lithotripter. *Ultrasound in Medicine and Biology 22*(3), 329–338.

Keller, J. & M. Miksis (1980). Bubble oscillations of large amplitude. *Journal of the Acoustical Society of America 68*(2), 628–633.

Kuznetsov, V. (1970). Equation of nonlinear acoustics. *Soviet Physics Acoustics 16*, 467–470.

Lifshitz, D., J. Williams, J. Lingeman, A. Evan, D. Rietjens & J. McAteer (2000). Efficiency of SWL stone fragmentation in vitro is improved by slowing sw delivery rate. *Journal of Urology 163*, 338.

Lifshitz, D., J. Williams, B. Sturtevant, B. Connors, A. Evan & J. McAteer (1997). Quantitation of shock wave cavitation damage in vitro. *Ultrasound Medical Biology 23*(3), 461–471.

Liu, X., S. Osher & T. Chan (1994). Weighted essentially nonoscillatory schemes. *Journal of Computational Physics 115*(1), 200–212.

Lokhandwalla, M. (2001). *Damage mechanisms in shock wave lithotripsy.* Ph. D. thesis, California Institute of Technology.

Lokhandwalla, M., J. McAteer, J. William & B. Sturtevant (2001). Mechanical haemolysis in shock wave lithotripsy (SWL): Ii. in vitro cell lysis due to shear. *Physics in Medicine and Biology 46*, 1245–1264.

Lord Rayleigh (1917). Pressure developed in a liquid during the collapse of a spherical cavity. *Philosophical Magazine 34*, 94–98.

Matsumoto, Y. & F. Takemura (1994). Influence of internal phenomena on gas bubble motion. *JSME International Journal series B- Fluids and Thermal Engineering 37*, 288–296.

Matula, T., P. Hilmo, B. Storey & A. Szeri (2002). Radial response of individual bubbles subjected to shock wave lithotripsy pulses *in vitro*. *Physics of Fluids 14*(3), 913–921.

Mohseni, K. & T. Colonius (2000). Numerical treatment of polar coordinate singularities. *Journal of Computational Physics 157*(2), 787–795.

Müller, M. (1989). Die fokussierung von wasserstoßwellen zur lithotripsy durch verschiedene ellipsoidreflektoren. *Biomedizinische Technik 34*, 62.

Müller, M. (1990). Dornier-lithotripter im vergleich vermessung der stoßwellenfeider und fragmentationswirkungen. *Biomedizinische Technik 35*, 250.

Paterson, R., D. Lifshitz, J. Lingeman, A. Evan, B. Connors, N. Fineberg, J. Williams & J. McAteer (2002a). Stone fragmentation in shock wave lithotripsy is improved by slowing the shock wave rate: studies with a new animal model. *Journal Urology*, Submitted.

Paterson, R., D. Lifshitz, J. Lingeman, A. Evan, B. Connors, N. Fineberg, J. Williams & J. McAteer (2002b). Stone fragmentation in shock wave lithotripsy is improved by slowing the stock wave rate: Studies with a new animal model. *Journal of Urology 168*, 2211–2215.

Plesset, M. & S. Zwick (1952). A nonsteady heat diffusion problem with spherical symmetry. *Journal of Applied Physics 23*(1), 95–98.

Press, W., S. Teukolsky, W. Vetterling & B. Flannery (1996). *Numerical receipes in Fortran 77: the art of scientific computing* (2nd ed.)., Chapter 16, pp. 731–735. Cambridge University Press.

Preston, A., T. Colonius & C. Brennen (2002, July). A simplified model of heat transfer effects on the dynamics of bubbles. In *ASME/FED Fourth International Symposium on Numerical Methods for Multiphase Flow*, Montreal, Quebec, Canada.

Prosperetti, A. & A. Lezzi (1986). Bubble dynamics in a compressible liquid. part 1. first-order theory. *Journal of Fluid Mechanics 168*, 457–478.

Reisman, G., Y.-C. Wang & C. Brennen (1998). Observations of shock waves in cloud cavitation. *Journal of Fluid Mechanics 355*, 255–283.

Sapozhnikov, O., V. Khokhlova, M. Bailey, J. Williams, J. McAteer & R. Cleveland (2002). Effect of overpressure and pulse repetition frequency on cavitation in shock wave lithotripsy. *Journal of the Accoustical Society of America 112*, 1183–1195.

Sapozhnikov, O., V. Khokhlova, M. Bailey, J. Williams, J. McAteer, R. Cleveland & L. Crum (2002). Effect of overpressure and pulse repetition frequency on cavitation in shock wave lithotripsy. *Journal of the Acoustical Society of America*, Submitted.

Sass, W., M. Braunlich, H. Dreyer, E. Matura, W. Folberth, H. Preismeyer & J. Seifert (1991). The mechanisms of stone disintegration by shock waves. *Ultrasound in Medicine and Biology 17*, 239–243.

Sass, W., H. Dreyer, S. Kettermann & J. Seifert (1992). The role of cavitational activity in fragmentation processes by lithotripters. *Journal of Stone Disease 4*(3), 193–207.

Shu, C.-W. & S. Osher (1988). Efficient implementation of essentially non-oscillatory shock-capturing schemes. *Journal of Computational Physics 77*(2), 439–471.

Sokolov, D., M. Bailey & L. Crum (2001). Use of a dual-pulse lithotripter to generate a localized and intensified cavitation field. *Journal of the Acoustical Society of America 110*(3), 1685–1695.

Sokolov, D., M. Bailey, L. Crum, P. Blomgren, B. Connors & A. Evan (2002). Pre-focal alignment improves stone comminution in shock wave lithotripsy. *Journal of Endourology 16*, 709–715.

Staudenraus, J. & W. Eisenmenger (1993). Fiber-optic probe hydrophone for ultrasonic and shock-wave measurements in water. *Ultrasonics 31*, 267–273.

Thompson, K. (1987). Time dependent boundary conditions for hyperbolic systems. *Journal of Computational Physics 68*, 1–24.

Wang, Y.-C. (1996). *Shock waves in bubbly cavitating flows*. Ph. D. thesis, California Institute of Technology.

Wang, Y.-C. (1999). Stability analysis of one-dimensional steady cavitating nozzle flows with bubble size distribution. In *Proceedings of the ASME/JSME Fluid Engineering Division Summer Meeting*, San Franscico, California.

Wang, Y.-C. & C. Brennen (1995). The noise generated by the collapse of a cloud of cavitation bubble. In *ASME/JSME Symposium on Cavitation and Gas-Liquid Flow in Fluid Machinery and Devices*, Volume FED 226, pp. 17–29.

Weir, M., N. Tariq & R. Honey (2000). Shockwave frequency affects fragmentation in a kidney stone model. *Journal of Endourology 14*, 547.

Yang, H. (1990). An artificial compression method for ENO schemes: the slope modification method. *Journal of Computational Physics 89*, 125–160.

Zabolotskaya, E. & R. Khokhlov (1969). Quasi-plane waves in the nonlinear acoustics of confined beams. *Soviet Physics Acoustics 15*, 35–39.

Zhang, D. & A. Prosperetti (1994). Ensemble phase-averaged equations for bubbly flows. *Physics of Fluids 6*(9), 2956–2970.